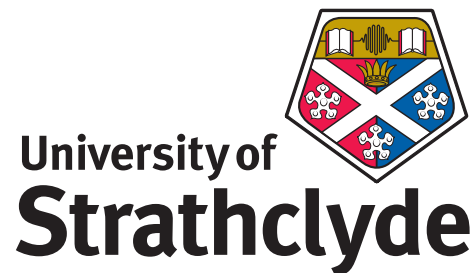**UNIVERSITY OF STRATHCLYDE**

Department of Physics

Development and Implementation of Monolithic GaN μLED Arrays for Multifunctional Optical Systems

by

Mark R. Stonehouse

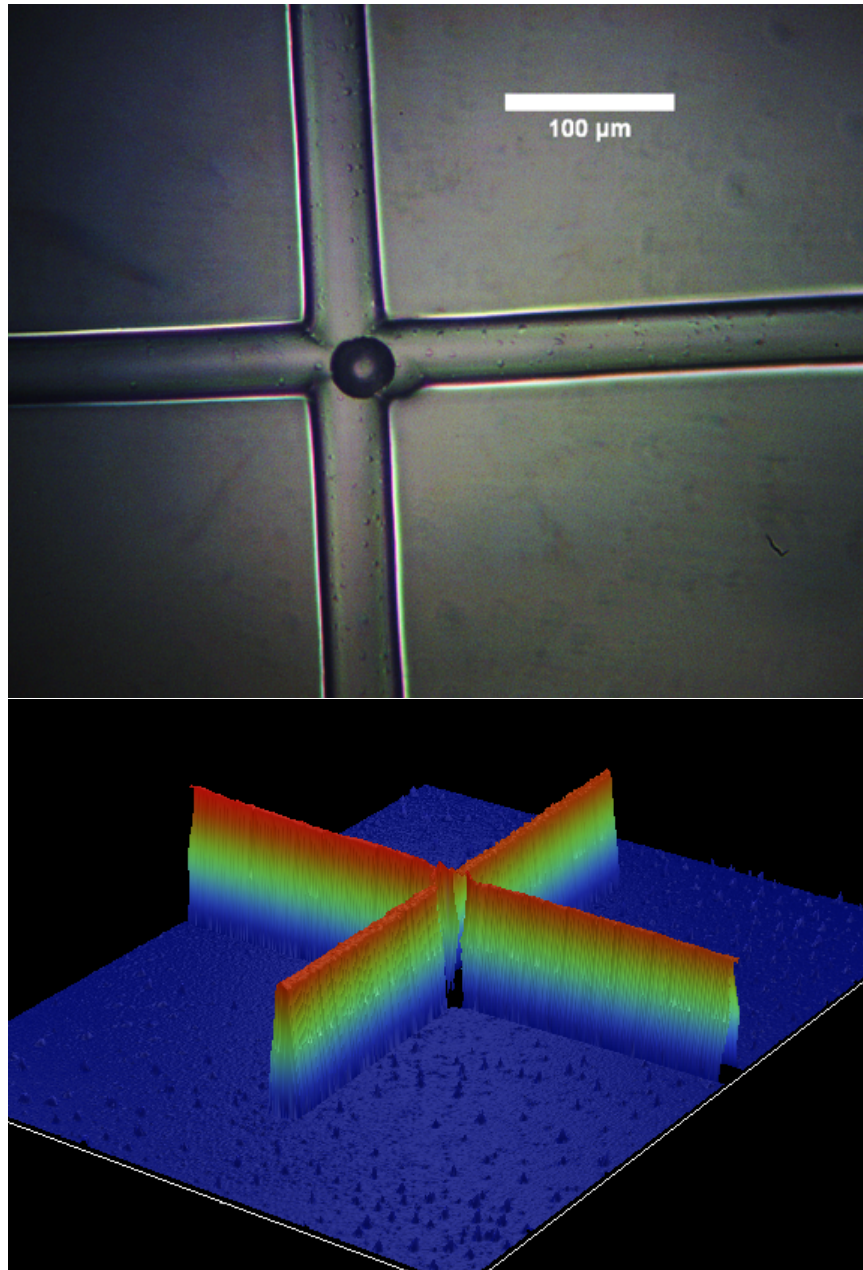A thesis submitted for the degree of Doctor of Philosophy

December 19, 2021

Frontispiece

Top) Plan view optical micrograph of a photocured structure aligned to a fluorescent marker produced through the use of a micro-LED automated photolithography system. Bottom) A 3D render produced by an optical stylus profiler of the same structure highlighting the uniform lines and sidewall.

Abstract

Monolithic LED arrays comprising micron-sized pixels are rapidly maturing as a technology due to their high efficiency and modulation rates. When coupled with complementary metal-oxide semiconductor (CMOS) electronics, which offer high level spatio-temporal control, such devices are capable of communications based applications along with the ability to provide structured illumination based functionality. This novel 'smart display' technology opens up a range of potential new applications.

This thesis describes the full development of such micro-LED arrays from initial design and fabrication through to implementation. By manipulating their fabrication process, highly customised devices can be created to accommodate the needs of a specialised setup or application scenarios. An example of this is the creation of n-contact devices and modifying the epitaxial structure of the array to allow for individually addressable pixels to better suit specific driving electronics. Devices such as these were developed and characterised. When compared to existing state-of-the art alternatives, these devices are shown to be either comparable with or to exceed them in terms of modulation rate and optical power output. In addition to modifying LED epitaxy to create novel applications, arrays of LEDs can also be implemented to create imaging systems capable of 3D imaging using only a single camera. This setup along with the steps taken to optimise the process is also detailed. Furthermore it includes the incorporation of a 3-dimensional tracking system, which can be used simultaneously with 3D imaging.

Along with new technologies introduced by micro-LED arrays, they can also be used to improve existing technologies and even add additional functionality to them. This thesis documents the development of a maskless photolithography setup wherein the optical emission pattern of the micro-LEDs is controllable through CMOS drivers to implement a direct writing tool and replace the quartz masks, typically used in photolithography. The setup is shown to be capable of producing highly uniform photo-

Chapter 0. Abstract

lithography defined structures of controllable width across a 16×16 grid where each coordinate is individually addressable. By synchronising the LED array's emission pattern with a motorised XYZ stage, continuous customisable directly written structures can be developed. Along with the photocuring components of the setup, an additional LED array was incorporated allowing for additional functionality through structured illumination. This comes in the form of the recognition, tracking and automated alignment to non-standardised alignment markers on a micrometre scale. Photocuring was performed whilst aligned to these markers while simultaneously tracking these markers to ensure the quality of fabricated structures.

Acknowledgements

Firstly I would like to thank my supervisors Prof. Martin Dawson and Dr. Erdan Gu for their advice and guidance throughout the project. I would also like to thank Dr. Johannes Herrnsdorf for allowing me to work alongside him and providing me with the opportunities I needed to complete this PhD. The majority of this work would not of been possible with his support and efforts. Thanks also go to Dr. Enyuan Xie for the work I did alongside him in my first year. I would also like to thank Dr. Benoit Guilhabert and Dr. Jonathan McKendry for their input and advice throughout.

I would also like to thank the other students I have had the privilege of working along side. Special thanks go to Ruaridh Winstanly, Francesca McEwan, Alex Griffiths, Alex Blanchard for the laughs and distractions and Georgios Arvanitakis for being an amazing travel companion.

Thanks also go to EPSRC for providing the funding which allowed this to happen.

Finally I would like to thank my family for getting me here in the first place and Priya Soni for everything she has done behind the scenes to support me throughout. This would not of been possible without them.

Contents

Contents

Contents

List of Figures

List of Figures

List of Figures

xi

List of Figures

List of Figures

List of Figures

List of Tables

Abbreviations

APD	Avalanche Photodiode
BER	Bit Error Ratio
CMOS	Complementary Metal-Oxide-Semiconductor
COSHH	Control of Substances Hazardous to Health Regulations
CVD	Chemical Vapour Deposition
DAC	Digital to Analogue Converter
DC	Direct Current
DNA	Deoxyribonucleic Acid
EBL	Electron Blocking Layer
FDMA	Frequency-Division Multiple Access
FOM	Figure of Merit
FOV	Field of View
FWHM	Full Width Half Maximum
GaN	Gallium Nitride
ICP	Inductively Coupled Plasma
InGaN	Indium Gallium Nitride
IV	Current - Voltage Relationship
LED	Light emitting diode
LI	Luminosity - Current Relationship
MIMO	Multiple Input Multiple Output

MOCVD	Metal-Organic Chemical Vapour Deposition
MOS	Metal Oxide Semiconductor
MQW	Multiple Quantum Well
NLOS	None Line Of Sight
NMOS	N-Type Metal Oxide Semiconductor
OOK	On-Off Keying
PAM	Pulse Amplitude Modulation
PMMA	Polymethyl Methacrylate
PMOS	P-Type Metal Oxide Semiconductor
PMT	Photomultiplier Tube
PVD	Physical Vapor Deposition
PWM	Pulse Width Modulation
QD	Quantum Dot
RF	Radio Frequency
RGB	Red Green Blue
RNA	Ribonucleic Acid
SMA	Subminiature Version A
SNR	Signal to Noise Ratio
SSK	Space-Shift-Keying
TDMA	Time-Division Multiple Access
VLC	Visible light communication
WDM	Wavelength Division Multiplexing
SEM	Scanning Electron Microscope
SISO	Single Input Single Output

Symbols for Physical Terms and Quantities

c	Speed of light
h	Planck's constant
λ	Wavelength
ω	Angular frequency
τ	Carrier lifetime
NA	Numerical aperture
η	Refractive index

Chapter 1

Introduction

This thesis will discuss the design, fabrication and implementation of gallium nitride based micrometre-sized light emitting diodes or micro-LEDs (μLEDs). With the improvements in epitaxy and performance, μLEDs are emerging as a new form of electronic visual display technology. LEDs are also becoming a desirable emitter in already established technologies such as lighting. Direct bump bonding to complementary metal-oxide-semiconductor (CMOS) drivers allows high-fidelity control over large arrays of LEDs which can enable additional functionality not possible with other emitter types. This chapter will outline the general LED background and theory of operation. It will also cover some of the applications of LEDs. Finally, it will provide a description of the development of the CMOS-integrated μLED arrays along with the finalised device characteristics.

Chapter 2 will describe the development of purpose designed μLEDs tailored for specific performance characteristics. This includes a reversal of the common epitaxial structure to allow for individually n-addressable electrical contacts. Chapter 3 will detail the development and characterisation of an optical lithography setup which uses a CMOS integrated μLED array as the emitters. A review of the photosensitive materials used in photolithography will also be provided. Chapter 4 will discuss the adaptation of the lithography setup detailed in chapter 3 to incorporate additional structured

illumination based functionality achieved through a second LED array. Structured illumination allows for features such as recognition and automated alignment through an motorised XYZ stage. Finally, Chapter 5 will summarise the key findings of this work and highlight further modifications and advancements which can be made to improve the photolithography setup.

1.1 LED History and Theory

1.1.1 Initial Development

The first LED was accidentally created by Henry Joseph Round in 1907 [1]. It was observed that crystals of silicon carbide (SiC) emitted a 'yellowish light' when under a 10 - 110 V bias. This was the first reported case of electroluminescence. It was not until the 1920's that this phenomenon was further developed into the first SiC LED by Oleg Losev [2] as was reported in "Luminous carborundum detector and detection effect and oscillations with crystals" [3]. Decades later, the first practical visible light LEDs were produced in 1962 by Nick Holonyak Jr whilst employed at 'General Electric' [4]. Following this, in 1968 the 'Monsanto Corporation' created the first mass produced, low cost LED based on red-emitting Gallium-Arsenide-Phosphide (GaAsP) [5]. Other available LEDs at this time emitted at red [6] and infrared [7] wavelengths and were fabricated with gallium arsenide (GaAs) and aluminium gallium arsenide (AlGaAs). LEDs such as these are used for applications ranging from surveillance systems [8] to health monitoring [9]. The extension of LED operation to green wavelengths was achieved by doping GaAsP with nitrogen [10] and with gallium phosphide (GaP) [11]. This works by the dopants creating an isoelectronic trap below the conduction band which can allow optical transitions via this deep state [12]. These devices were commonly used for simple displays, for example in digital wrist watches. Due to the limited optical output power, efficiency and available wavelengths, early applications of LEDs were restricted. It was not until advancements in semiconductor materials and epitaxy (the

layer-by-layer growth of single crystal thin films on planar-wafer substrates) that LEDs had the capability to fully broaden out in wavelength, performance and applications.

Despite reasonably efficient red-green LEDs having been commercially available from the 1960's, based on compound semiconductors, blue wavelengths relied on SiC based devices which were of poor performance due to having an in-direct bandgap and requiring momentum conservation during optical transitions [12]. Further development of LEDs was stalled until the 1990s when advancements in gallium nitride (GaN) technology enabled it to be fabricated with a higher output efficiency [13,14], thus leading to its market uptake. These advances came from the growth techniques of metal organic chemical vapor desposition (MOCVD) and specifically [1] the ability to successfully p-dope GaN using low energy electron beam irradiation or thermal annealing and [2] growing low temperature GaN buffer layers on the sapphire substrate [15] to reduce dislocation defects in the crystal structure. The development of efficient blue LEDs is significant as it allows for white light to be made by combining LED emissions of the three primary colours [16]. Another way to generate white light from LEDs is to coat a blue LED in a phosphor coating to convert some of the light into longer yellow wavelengths. This technique was emphasised in the citation for the 2014 Nobel prize awarded to Isamu Akasaki, Hiroshi Amano and Shuji Nakamura for blue LED development [17]. This capability has applications in general purpose illumination due to the long lifetime and high efficiency of LEDs in comparison to fluorescent lamps and incandescent bulbs. If the current trends in efficiency improvements hold, LEDs will be over 60% more efficient than fluorescent lamps and 90% more efficient than incandescent bulbs [18]. Moreover, LED light fittings can exceed by upwards of 100 times the life expectancy of incandescent bulbs.

Notwithstanding applications such as solid state lighting and general illumination [19], the low cost, high efficiency and long lifetime of LEDs makes them attractive candidates for other uses. More recent applications include televisions (in back lighting or in mini-LED or micro-LED formats), wearable screens such as in smart watches,

car headlights and portable water purification devices. Portable devices in general can benefit from the high external quantum efficiency (EQE) of LEDs as they can be operated at low powers thereby reducing the battery requirements of the devices. This is especially true for UV emitting devices as traditional methods involve mercury vapour lamps which are physically bulky, have a high power consumption and are fragile. In addition, the high modulation bandwidths associated with modern μLEDs [20] allow for 'smart' lighting systems where the same emitters used for general illumination can be used for additional functionality such as data communications and object tracking [21–24]. Beyond the electrical/optical characteristics of these devices, the ability to fabricate high density micro-scale emitters also provides other opportunities. An example of this is the use of micro-LED probes for in-vivo optogenetic neural stimulation [25]. Here the probes also benefit from these high efficiency devices producing little heat, making them suitable for operation in/around biological samples without causing significant damage.

1.1.2 Electroluminescence

LEDs are fabricated out of a family of materials called semiconductors. These materials are intermediate between conductors and insulators in terms of their electrical characteristics. The band gap in a material is a range of energy levels that are impossible for an electron to possess and is often regarded as the energy difference between the valence and conduction bands. In insulators there are few to no free electrons in the conduction band and the band gap is sufficiently large that electrons can not be easily excited into it. Conductors, on the other hand, have their valence and conduction bands partially overlapped allowing for some of their valence electrons to move freely through the material. This can also be explained in terms of the materials Fermi-level, which is the energy at which there is a 50% chance of an electron occupying it. In conductors, the Fermi level can be seen to be within either the valence or conduction band whilst in semiconductors and insulators the Fermi level is within the band gap. Semiconductors

have a relatively small band gap ($\approx$0.1 - several eV) wherein electrons can fairly easily be excited into the conduction band, for example with thermal, optical or electrical excitation. Note that the Fermi level can be altered through the positive (p) or negative (n) doping of the semiconductor, moving in energy towards the conduction band when n-doping and towards the valence band when p-doping. Intrinsic semiconductors are semiconductors that are pure and have no added dopants. When an electron is excited into the conduction band through any means, it leaves behind a vacancy, or 'hole', in the valence band. These holes act as if they were a positively charged particle and can also provide electrical conduction. Before doping, intrinsic semiconductors are neutrally charged and have an equal amount of holes and electrons. Typical doping concentrations range between 10^{15} to 10^{18} cm^{-3}. The change in charge comes from the fact that dopant materials will have either more or less electrons in its valence band, thus contributing more electrons or holes to the material lattice. Positively charged dopants (e.g. magnesium) are known as acceptors, as they have additional holes to accept an electron, and produce a positively charged semiconductor known as p-type. Conversely negatively charged dopants (e.g. silicon) are known as donors, due to having additional electrons to donate, and produce a negatively charged semiconductor known as n-type.

Electroluminescence is the process where photons are produced when current is injected into a semiconductor and electrons from the conduction band drop to the valence band. As energy must be conserved, the energy difference between the two bands is the same as the energy of the resultant photon. This also corresponds to the wavelength of the emitted photon through the following equation:

$$E = \frac{hc}{\lambda},$$
(1.1)

where E is the energy difference between the valence and conduction bands, h is Planck's constant, c is the speed of light in a vacuum and λ is the photon wavelength.

Chapter 1. Introduction

Due to the ability to alloy semiconductors during growth, the band structure of the LED materials can be tailored to produce specific emission wavelengths, thus resulting in different coloured LEDs covering the deep UV to the IR.

The basic principle behind LED operation is based on carrier recombination within a p-n junction. This junction is formed by growing two heavily doped layers of p-type and n-type semiconductor material on top of each other. By doping the material, it not only increases the number of available carriers, but it also creates a band structure shown in Fig. 1.1. Due to the opposing charges, excess carriers diffuse into the opposing material type and recombine. This results in an area depleted of charge carriers known as the 'depletion region' at the interface. This region creates a potential difference, V_D across the interface known as the 'diffusion voltage' which opposes the flow of carriers across it, meaning that carriers must be able to overcome the potential barrier energy, eV_D, to flow into the opposing region. This diffusion voltage dictates the size of the depletion region and is a product of the concentration of dopants. In order for the LED to operate, a forward bias can be applied which reduces the potential barrier and allows carriers to enter the depletion region where they recombine and produce photons. This is shown in Fig. 1.1b. Note that recombination can also be non-radiative resulting in phonons or Auger processes.

Light generation by the LED is dependent on the rate at which carriers are able to recombine, which is in turn dependent on the carrier densities within the active region. Having a higher carrier concentration improves the rate at which electrons and holes are able to recombine as shown by equation 1.2:

$$R = Bnp \tag{1.2}$$

Where R is the recombination rate, B is the radiative recombination coefficient, n is the electron concentration and p is the hole concentration. Note that the concentration of holes and electrons are the equal in intrinsic semiconductor materials.

6
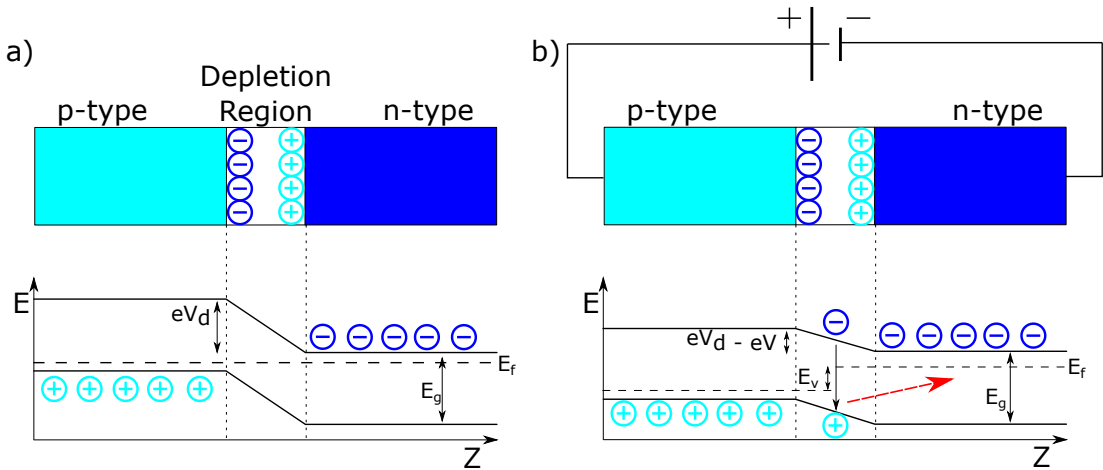
Figure 1.1: A schematic showing the band structure of a p-n junction under a) no bias and b) forward bias. The vertical axis is energy and the horizontal axis is distance through the junction.

By driving LEDs at higher current densities, they will produce more light until limited by thermal effects. The problem with the simple p-n junction is that the carriers will propagate through the materials' relatively large volume, thus reducing the carrier concentration. Therefore, modern LED structures typically confine carriers using a p-i-n structure. Sandwiching a lower bandgap material between two materials with a higher bandgap, known as a 'heterojunction', creates potential barriers which confine carriers thus effectively increasing the carrier concentration. Carriers within this region can be subject to quantum confinement effects if the structure is thin enough. Most commonly this is achieved by multiple quantum well (MQW) layers in the intrinsic region of the device. These are ultra-thin layers of a lower bandgap material. Fig. 1.2a shows how the effects of quantum confinement become relevant if the thickness of the active layer in an LED approaches the de Broglie wavelength of electrons ($\approx$10 nm). As described in the infinite potential well scenario [26], the available energy levels then become discrete quantised values. This means that by carefully engineering the band gap and QW structures, very specific emitted wavelengths can be achieved. A method for preventing leakage and containing the carriers within the device active region is to include an electron blocking layer (EBL). This layer will be located between the MQW's
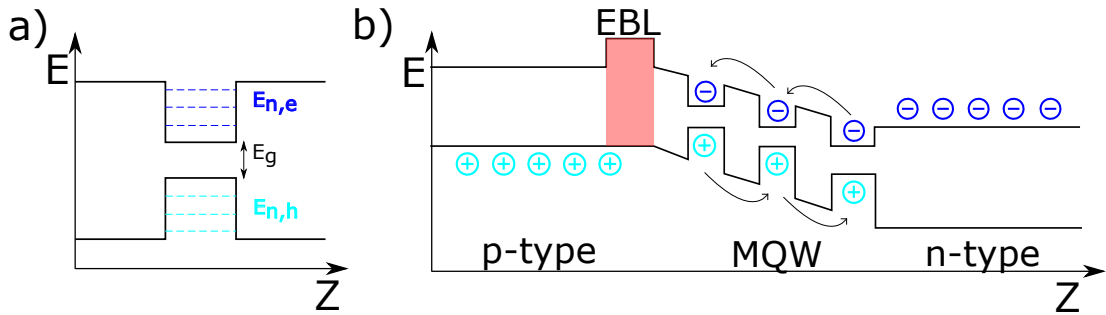
Figure 1.2: a) A quantum well demonstrating the discrete available energy levels for both electrons and holes. b) A diagram demonstrating the band structure of an LED with multiple quantum wells and an electron blocking layer.

and the p-type semiconductor and will have a higher conduction band potential than the p-type material. This creates a potential barrier that the carriers must overcome in order to diffuse out of the active region, this is shown in Fig. 1.2b. The reason for this blocking layer being on the p-side of the junction is due to both a disparity in electron and hole concentrations [27,28] and the higher carrier mobility of electrons compared to holes. This leads to an excess of electrons within the MQW structures which requires the EBL to be on the p-side to compensate for.

1.1.3 Nitrides and Epitaxial Materials

All LEDs featured in this thesis were fabricated using commercially available AlInGaN LED wafers. In these structures, indium gallium nitride (InGaN) quantum wells giving visible or near UV visible wavelength emission are confined by GaN barriers. The emission wavelength is controlled through the composition of the InGaN alloy, with higher indium concentrations giving longer wavelengths, and by the thickness of the quantum wells via the quantum confinement effect introduced above.

1.1.3.1 Substrate Choice

Most of the work described here uses micron-sized pixel LEDs or μLED epistructure. The first step in fabricating a μLED device is to choose the substrate on which to grow

the LED epistructure. Sapphire (Al_2O_3) is the most common substrate material used in GaN based LEDs though other options, such as zinc-oxide, silicon carbide, silicon and more recently gallium nitride [29, 30], are available. In this thesis sapphire substrates were used and operated in flip-chip format. The reason that sapphire is commonly used is that it is thermally stable, optically transparent and can be relatively cheaply acquired. Another point to note is that sapphire is not electrically conductive. This means that the metal contacts to each device must be on the same side of the wafer.

AlInGaN wafers are typically grown in the c-axis crystal orientation ([0001]) of sapphire. Due to sapphire having a poor lattice match to GaN, $\approx 15\%$, the resultant wafers have a high density of dislocation defects [5]. In order to reduce this, a thin buffer layer (≈ 20 nm) is first grown directly upon the substrate [31]. This layer reduces the strain caused by lattice mismatch and allows the growth of nitride materials with less dislocations. Despite this buffer layer, GaN based devices still demonstrate a very high density of dislocations when compared to other LED materials. For example, GaN will offer a density of $\approx 10^8$ cm^{-2} whereas silicon will only have $\approx 10^4$ cm^{-2}. A characteristic trait of GaN devices is that they are able to operate efficiently at this dislocation density where other materials would be unable to emit any light at all [32], although this reason behind this is still debated.

1.1.3.2 Dopants

AlInGaN is typically grown by MOCVD. This technique allows for multi-layer crystalline thin-films to be grown on a suitable substrate by depositing from vapour phase materials. MOCVD can give growth rates of over 100 μm per hour [33]. Two inch diameter sapphire wafers are commonly used in this process, although larger substrates are becoming available.

When growing GaN, the resultant material is usually n-type due to unintentional doping [34]. It is relatively simple to produce n-type materials of more defined doping levels by intentionally doping GaN with silicon. However, producing p-type GaN is

significantly more difficult. Efficient p-doping was first achieved by Amano et al. [35] and later refined by Nakamura et al. [36] by introducing magnesium. This method however introduces a problem wherein the magnesium is 'deactivated' by hydrogen atoms during the growth process. This can be compensated, to a certain extent, by annealing the material at temperatures over 600°C, although due to the low doping densities discussed above, it can be assumed that this does not fully remove the hydrogen contaminants. The annealing process is believed to break the relatively weak bonds with hydrogen, and as the hydrogen atoms are sufficiently small it allows them to escape the material lattice.

1.1.3.3 LED Design

Fig. 1.3 shows a typical cross-sectional schematic of GaN μLEDs fabricated from a commercially purchased wafer. The LED wafer comprises of the substrate, n-GaN, MQWs and p-GaN. Note that additional layers such as electron blocking layers are not shown in this figure. Here each individual LED element is defined and isolated by etching down to the n-GaN, typically using an inductively coupled plasma dry etching tool. This exposes the n-GaN to allow for an electrical contact to be fabricated, and results in an LED array with a common/shared n-electrode (cathode) and individually addressable p-electrodes (anodes). After this etch, a dielectric insulation layer is deposited over the n-GaN to allow for individual anodes to be fabricated without causing short circuits. Note that if the p-contact metal is chosen appropriately it can not only produce an ohmic contact but also act as a reflector for the emitted light which can help with light extraction. These devices are designed to be operated in flip-chip format, meaning that the device is bonded upside down and light is extracted through the substrate. The added benefit of having the LED mount bonded to the substrate is that it will act as a heat sink. This mode of operation also allows for the direct bump bonding onto CMOS electronics and is discussed further in Section. 1.3.1.
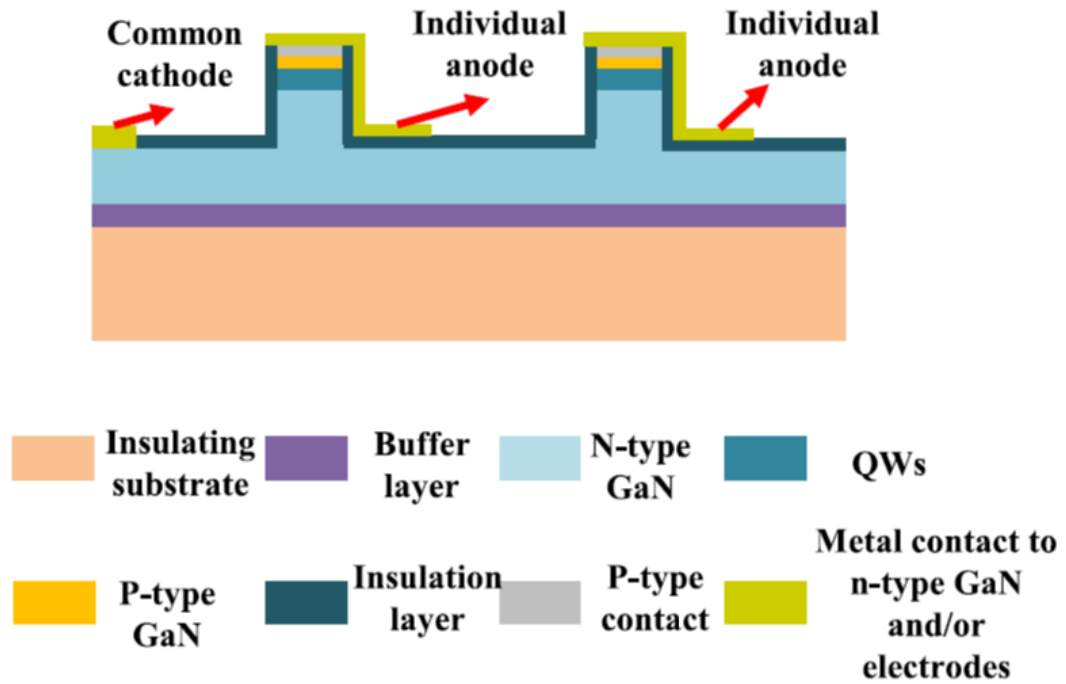
Figure 1.3: A cross-sectional schematic showing the typical epitaxial and layer structure of a μLED array with individually addressable p-contacts [37].
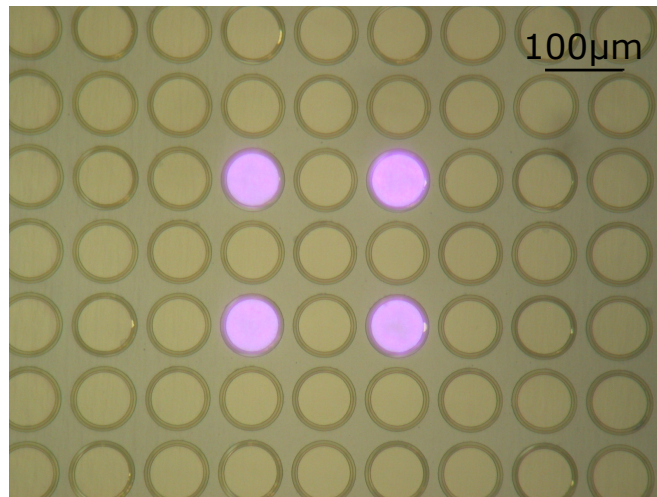
Figure 1.4: A plan view optical image of a typical μLED array with individually addressable p-contacts. Here, 4 pixels are shown switched on.

11

1.1.4 LED Characteristics

LED characteristics are not only defined by their emission wavelength. The material and epitaxial choices during their fabrication process are also capable of defining the device format, electrical characteristics, emission pattern and optical performance properties. In this thesis, the LED devices utilised throughout are micro-pixelated LED arrays (μLEDs). The difference between these μLEDs and conventional broad area devices is that each emitter element in a μLED array will have a diameter of 100 μm or less, whereas more conventional broad area devices typically have active areas of 0.1 - 1 mm^2. Typically, broad area devices, or other such devices, are used for high powered general purpose illumination applications. On the other hand, μLED devices are the basis of new types of high resolution display technology and have other advantageous characteristics such as high modulation bandwidths.

1.1.4.1 Pixel Shape and Fill Factor

As discussed in Section. 1.1.2, it is optimal to have a high carrier concentration within the LED to ensure a high rate of carrier recombination. This goes hand-in-hand with the production of short light pulses or fast modulation to an electronic stimulus. Low recombination rates increases the average minimum time it takes for all the injected carriers to produce photons, which in turn create longer pulses. Although MQW structures provide good carrier confinement perpendicular to the epitaxial growth plane, broad area devices still have two other large dimensions in which carriers can diffuse.

By physically producing smaller pixels, i.e. μLEDs, it is possible to produce very high carrier concentrations which further increases recombination rates [38]. Smaller pixels have also been shown to have reduced heating effects which improves their EQE [39]. It has also been observed that multiple μLEDs emit light with upwards of 60% more efficiency than broad area devices with similarly sized active regions [40]. The ability to create micro-pixelated devices also makes them suitable for applications which do not necessarily require the high bandwidths they are capable of. For example, high
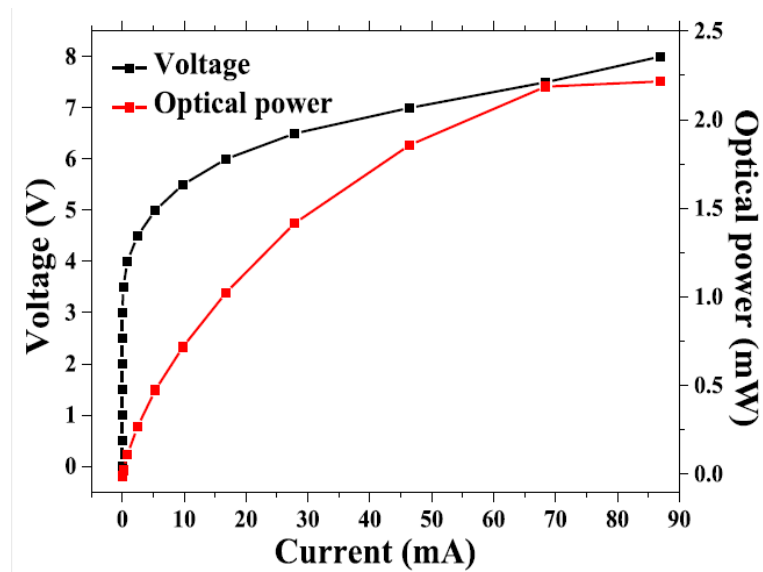
Figure 1.5: A graph depicting the typical IV and LI characteristics of a 24 μm diameter GaN μLED [37].

definition in organic LED displays are sought after due to their high colour contrast and their high efficiency emission in comparison to other display types.

1.1.5 Characterisation Techniques

1.1.5.1 LI and IV Measurements

An LED's electrical-to-optical (E-O) performance is generally defined by its current and voltage draw in comparison to its electroluminescence. Fig. 1.5 shows a representative example of current to voltage (IV) and electroluminescence to current (LI) curves for an LED, in this case a 24 μm diameter GaN μLED. The IV curve shows a typical diode behaviour with a distinct turn on voltage of the device and the series resistance of the device, which can be determined by taking the slope of the linear portion of the plot. The LI curve demonstrates the trend of increasing output power with current, with the increase subject to 'thermal rollover' where the power output is dominated by heating effects, and lossy recombination mechanisms.

1.1.5.2   Frequency Response Measurements

The maximum operating modulation frequency of an LED is defined by its optical bandwidth. This is the rate at which the device can be switched between high and low intensity levels and is directly dependent on the recombination rate of carriers within its active region. Optical bandwidth is important for many applications primarily within the communications field. As discussed in Section. 1.1.2, μLEDs demonstrate a significantly higher bandwidth than conventional broad area devices, and are often optimised for high bandwidths.

The setup for measuring a device's frequency response is relatively simple. A network analyser produces a sinusoidal driving signal with a gradually increasing (swept) frequency. This signal is kept within positive voltage levels by a DC voltage produced by a bias-tee. Depending on the voltage at any given time from the signal, the LED will emit different light output intensities. This output power is collected by an AC coupled avalanche photodiode (APD) which returns the information to the network analyser which in turn calculates the device's frequency response. The effect under scrutiny by this is the device's ability to successfully change from high to low light intensities with an ever increasing driving frequency. This change in power (ΔP) will eventually decrease into a constant output level as the LED becomes less able to respond fast enough to the driving signal. The optical bandwidth of an LED is defined as the frequency at which the emitted power drops to 50%, or -3 dB. It is worth noting that as the photodiode produces a voltage from the optical signal in a linear fashion, and the network analyser produces a frequency response curve which is proportional to the square of voltage. Thus on the resultant response curve the optical bandwidth relates to the -6 dB frequency. The frequency response for a μLED can be approximated by the following equation:

$$P(\omega) = \frac{1}{1 + (\omega\tau)^2},$$
(1.3)
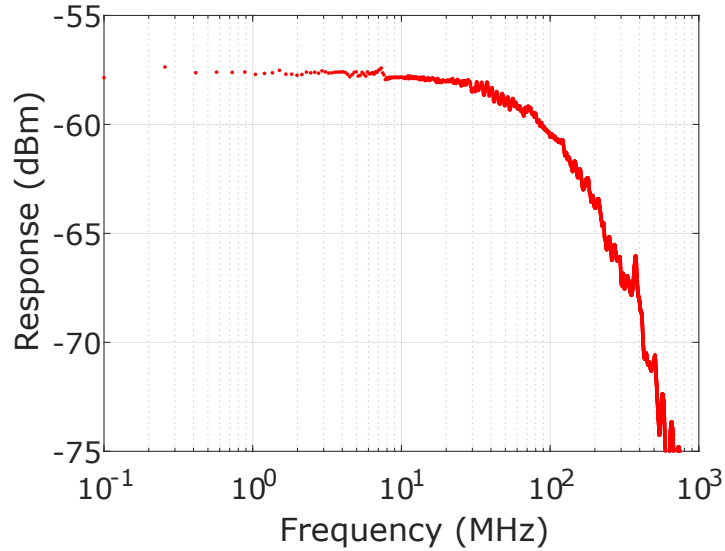
Figure 1.6: A graph showing the frequency response of a μLED measured as described in the text.

where ω is the angular frequency of the AC signal and τ is the carrier lifetime within the device. For larger devices with dimensions above $\approx$200 $\times$ 200 μm^2 this switching speed is dominated by the resistance $\times$ capacitance (RC) time constant [22]. The bandwidth of the device can be given by:

$$f_{bw} = \frac{1}{2\pi\tau}.$$
(1.4)

As shown by Equation. 1.4, reduced carrier lifetimes result in a higher optical bandwidth. Another factor which may affect this is that non-polar and semi-polar crystal orientation materials demonstrate a higher bandwidth due to improved carrier wavefunction overlap within the quantum wells which in turn also reduces the carrier lifetime [41]. A typical frequency response curve of a comparable device to those used in this thesis is shown in Fig. 1.6.

1.2 Photonic Applications

The practical applications for light-based technologies can range from optical communications [42] to bio-sensing [43]. This section will explore photonic capabilities used for the work in this thesis, in addition to how the relevant processes work, particularly how light is used for communications, photolithography and photometric stereo imaging. Although this is only a small selection of possible applications, they cover a wide range of topics and have different requirements from the emitters used.

1.2.1 Visible Light Data Encoding Schemes

Optical wireless communications (OWC) is the use of visible, ultraviolet or infrared light to send data signals. This can also be designated 1visible light communications' (VLC) when the visible part of the electromagnetic spectrum is used. With modern emitter technology, OWC systems can be modulated to GHz rates, taking advantage of techniques manipulating the frequency, phase, intensity and/or the wavelength of the light. More sophisticated options for modulation are available, such as polarisation and angular momentum, however this places additional stringent requirements on the receiver and emitter. For the most part, OWC can be thought of in a similar fashion to traditional electrical communications only without the need for physical conductors to transmit the signal, plus a photo-emitter and receiver to encode and decode the signal into light.

An advantage which OWC has over radio frequency (RF) communications, which achieves a similar function apart from the higher data rates, is the reusable nature of the optical signals. With the expansion of portable and wearable technology, there has never been a greater demand for bandwidth. Because of this, the current methods of radio and microwave based communications are beginning to run out of bandwidth, meaning that alternative methods of communications will soon be required in order to satisfy the demand. Optical bandwidths have $\approx$320 THz of available and unregulated

bandwidth which can be reused repeatedly, even within a single building, due to light being unable to penetrate many materials (e.g. walls). This also means that indoor based communications are more secure than RF based communications as it is more difficult to intercept signals.

1.2.1.1 Common Techniques for Data Encoding

Much like in electronic data communications, many encoding schemes have been developed to increase the achievable data rates in optical communications. Although some techniques have a direct equivalent in other forms of data communication, some are applicable exclusively to OWC by altering the characteristics of light. The operating principles of some common techniques which were used in this thesis are given below.

1.2.1.1.1 On-Off Keying On-off keying (OOK) is the simplest form of data transmission. In this scheme the output of the transmitter has only two modes, 'on' or 'off', which represents a '1' or a '0' at the receiver end. This is typically achieved by combining a DC voltage with the data stream through a bias-tee. This can also be achieved by driving the emitter with an amplifier capable of modulating the data stream about a reference point. The data decoding works by first setting a reference intensity level, and if the data signal is above this threshold it is seen as a '1' and if the signal is below it is seen as a '0'. The maximum data rate of this link is directly correlated to the modulation rate of the emitter. If the data stream is operated at a frequency above the modulation bandwidth of the device, the total intensity swing will reduce resulting in bit errors and noise. When operated significantly above the modulation bandwidth the data will degrade towards a constant intensity and the data cannot then be decoded. A visual representation of an OOK data signal is shown in Fig. 1.7.

1.2.1.1.2 Pulse Amplitude Modulation Pulse amplitude modulation (PAM) is similar to OOK in that it directly correlates intensity values into data bits. However, PAM offers the ability to encode multiple bits simultaneously giving higher data rates
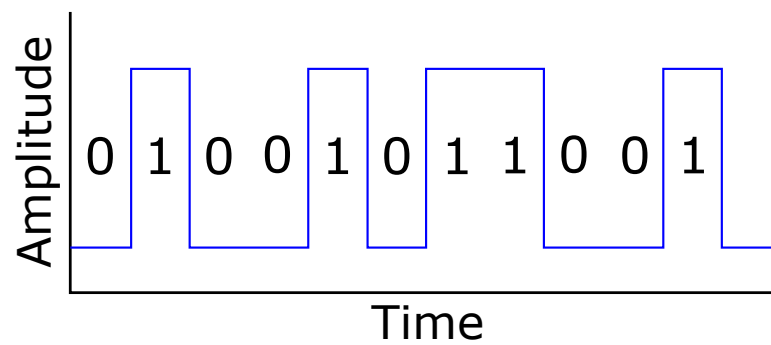
Figure 1.7: A schematic of an example of OOK data transmission with data values labelled.
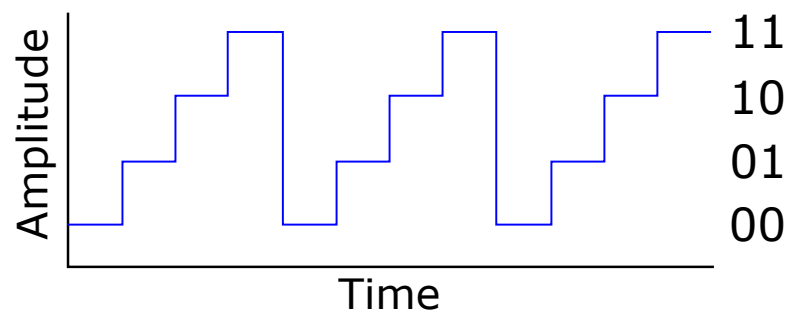
Figure 1.8: A schematic of an example of 4-PAM transmission with data values labelled.

for the same bandwidth. Here the number of intensity levels increase from two, as in OOK, to M discrete levels, where M must be a power of 2. In this case M-PAM will encode $\log_2(M)$ bits per point. This is limited by the light emitter's ability to produce discrete values and is often limited by the signal-to-noise ratio (SNR). As shown in Fig. 1.5, an LED's output power is non-linear with current which restricts the available output power intensities as the driving current increases. A schematic example of 4-PAM is given in Fig. 1.8.

1.2.1.1.3 Manchester Encoding Manchester encoding differs from OOK and PAM in that it uses a change in signal amplitude to represent bits instead of an amplitude level. For example a logic '1' can be represented as a high-to-low transition while a logic '0' can be seen as a low-to-high as shown in Fig. 1.9. An advantage of this scheme is that it embeds the clock information into the signal itself which can be decoded at
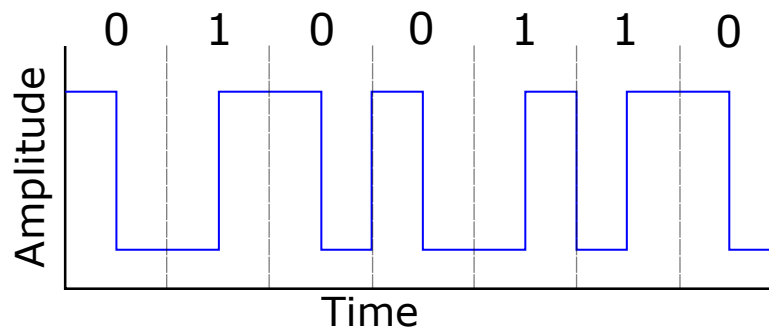
Figure 1.9: A schematic of an example of a Manchester encoded data stream with data values labeled.
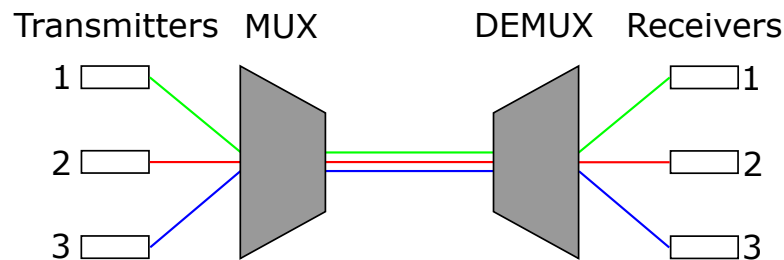
Figure 1.10: A schematic showing how multiple wavelengths can be multiplexed and then de-multiplexed to transmit multiple optical beams in the same link.

the receiver to allow for synchronisation. However, it comes at the cost of effectively halving the data rate when compared to the available transmission bandwidth. This is because for each bit two logic levels are required instead of one.

1.2.1.1.4 Wavelength Division Multiplexing Wavelength division multiplexing (WDM) is a system which combines multiple different data signals which have been transmitted on multiple distinct wavelengths of light. This allows for a single link to have an increased capacity by utilising receivers which are capable of independently extracting each of the original data streams. WDM can be used in conjunction with other encoding streams with each wavelength carrier acting independently to further increase data rates. This system is shown schematically in Fig. 1.10.

WDM is very applicable for LED based communication as such devices are capable of producing a spectrally discrete output at wavelengths from deep UV to infra-red with a narrow linewidth, and are able to be driven by simple electronics when compared to

other light emitters, i.e. lasers. This allows for the practical construction of compact emission systems. A potential issue, however, for LED based systems is the high amount of optical power that can be lost through beam divergence in the optics used to combine the multi-wavelength light.

1.2.1.1.5 Spatial Multiplexing   Unlike data schemes which encode the data stream itself, spatial multiplexing instead encodes data in the position of said data stream. For example, by having a series of 4 LEDs and detecting which LED is active at any given time, data can be encoded in a similar way to 4-PAM only instead of modifying the light intensity the user switches the active LED. This can be in turn be used alongside other encoding schemes to produce systems where multiple inputs carry encoded data to further increase the data capacity of a link whilst reusing the same frequency band. By doing this it means that the Shannon limit can be bypassed [44]. Fig. 1.11 shows this method using four emitters.

1.2.1.2   Network Design

In addition to optimising the data signal, the design of the network which the signal is sent across is also important. The most basic form of network is a single-input-single-output (SISO). This is a data link where the transmitter modulates only a single emitter and the receiver has only one detector, as shown in Fig. 1.12. The advantage of this setup is the simplicity in both hardware and processing power required to encode/decode the data signal. However, this link is ultimately limited to Shannon's law and is fully dependent on the channel capacity and SNR.

An alternative to this method is a multiple-input-multiple-output (MIMO) architecture where the transmitter has multiple emitters and the receiver has multiple detectors. This can be used to either create systems which essentially operate as a SISO link but with multiple optical channels to improve data throughput, or a system where multiple independent transmitters can communicate with multiple independent receivers. This
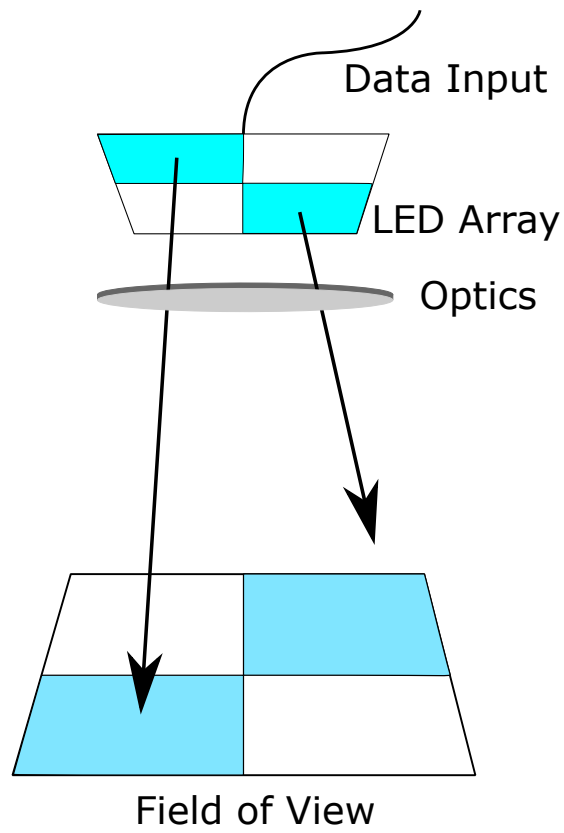
Figure 1.11: A schematic showing how an LED emission pattern directly correlates to a similar pattern within the FOV.
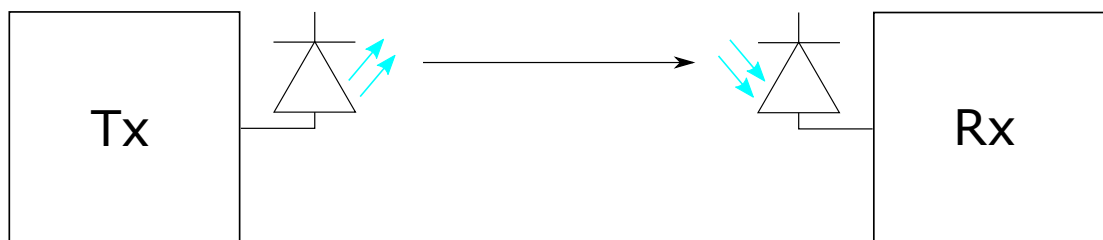
Figure 1.12: A schematic of a SISO network.
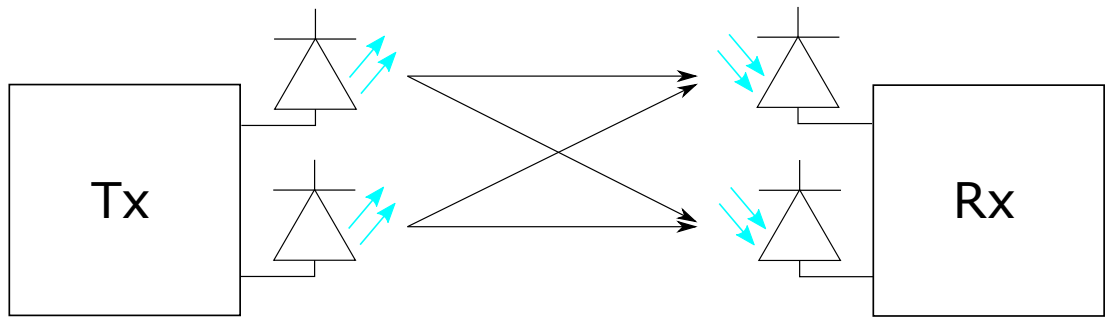
Figure 1.13: A schematic of a MIMO network.

is shown in Fig. 1.13. However, this comes at the cost of additional complexity to encode and decode signals and more costly hardware. MIMO systems, and variations thereof, have also been shown to improve the SNR across a data link [45]. In terms of optical links, MIMO is an extension of spatial multiplexing which can be achieved with either an array of emitters or multiple discrete emitters providing a method of extracting each signal is possible, e.g. wavelength multiplexing.

A variation of a MIMO system is space-shift-keying (SSK). In this setup only a single emitter is activated at a time, thus implicitly conveying information based on which emitter it was. This method removes any cross-channel interference and removes the need for any inter-transmitter synchronisation. It also reduces the complexity of the system and provides a lower error rate.

1.2.2   Photolithography

Micro-patterning is a method of transferring a pattern to a substrate and is commonly used during the microfabrication of semiconductor devices. It also has applications in microsensors, microfluidic devices and organic electronics, such as organic LEDs. This section will give an overview of how micro-patterning is achieved with a focus on optical lithography.

1.2.2.1 Theory of Optical Photocuring

The most commonly used method of micro-patterning is photolithography, also known as optical lithography. This process works by coating a layer of photo-sensitive material, also known as a photoresist, onto a substrate and then selectively exposing areas of that resist in a desired pattern. When the photoresist is exposed to a wavelength of light it is sensitive to, it chemically alters to either form an insoluble solid structure in those areas for negative resists, or decomposes and becomes soluble for positive resists. The patterns are typically created by projecting general illumination through a custom designed quartz mask with the negative pattern imprinted on it. The mask is unique to each pattern and cannot be altered once created. This can be a problem as these masks are both expensive and time consuming to manufacture, especially for prototyping and infrequently used patterns. Common embodiments of photolithography setups use mercury vapour lamps to generate UV/violet light however these emitters are physically large, inefficient and rely on toxic materials. Large area UV LEDs are able to replace these lamps and offer more desirable qualities such as a reduced size and power requirements [46]. A schematic of conventional mask-based optical lithography is shown in Fig. 1.14.

A significant issue with conventional photolithography is the reliance on physical masks to create and project the desired pattern. By contrast, 2-dimensional monolithic μLED arrays allow for maskless direct writing processes. This has been demonstrated in two distinct modes: using de-magnified projection of spatial light patterns [47], and by translation of a sample under illumination from a single pixel [48]. The spatio-temporal control offered by CMOS integrated μLEDs simply allows for the desired patterns to be projected onto the substrate by modulating individual LEDs within the array that correspond to the pattern. By doing this a 'library of masks' can in effect be generated and stored electronically as required giving a level of flexibility previously unavailable.

Regardless of which of these methodologies are used to generate the pattern, the
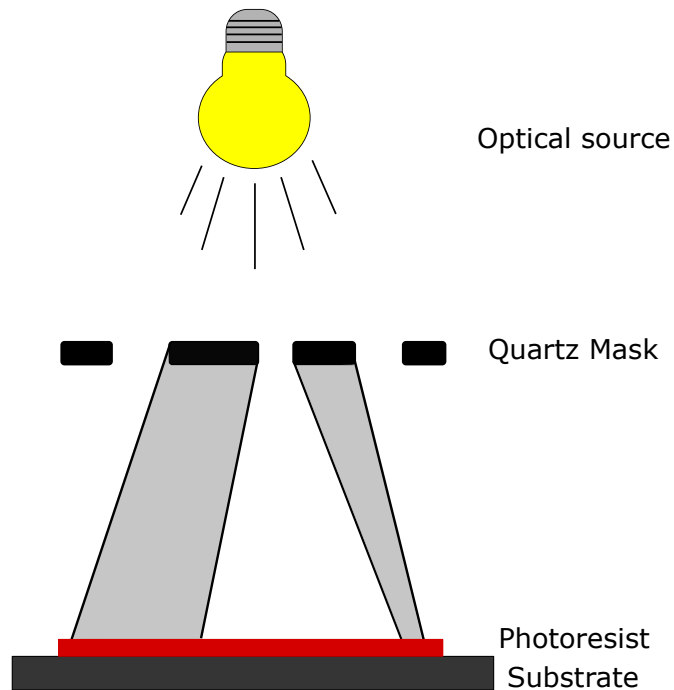
Figure 1.14: A schematic of a conventional mask-based optical lithography setup.

maximum resolution achievable with these optical sources is given by the diffraction limit:

$$d = \frac{\lambda}{2NA},\tag{1.5}$$

Where d is the diffraction-limited spot size, λ is the wavelength of light and NA is the numerical aperture of the emitting optics. This will usually be dominated by the NA of the used optics. Reducing the wavelength of light used, for example, from the readily available 370 nm to deep UV, means that smaller spot sizes and higher resolution structures become achievable, making LEDs even more desirable as light emitters as they are capable of producing such wavelengths with the added bonus of being cheaply and easily interchanged as required.

1.2.2.2 Effects of Device Characteristics

The characteristics of the light sources play a crucial role in photolithography. Excluding other practical considerations such as power requirements and device lifetime etc. the requirements for mask-based lithography are, simply, to have the correct wavelength for photocuring and sufficient optical power density to cure the resist in a reasonable time frame. However, in maskless LED based systems there is more which can be controlled or manipulated. For example, the projected optical spot size is a direct result of the LED pixel size and the de-magnification of the setup, which ultimately defines the resolution the system is capable of. Along with this, the fill factor of the LED active regions within the array define how close the projected spots are in the exposure plane. The impact of this can be seen in the system's ability to create large or continuous structures on static substrates as, if the optical spots cannot generate structures which overlap, then only individual dots can be patterned. This goes hand-in-hand with the optical spot shape being defined by the shape of the LED which created it. For example a circular pixel will create a circular structure whilst a square pixel will create a square structure. Fortunately, these characteristics can all be controlled during the LED fabrication process so highly customised devices can be created to suit specific needs. Moreover, if the LED emissions can be synchronised with a substrate mounted on a mechanically controlled translation stage then further patterning flexibility is possible.

Beyond defining the actual pattern shape, each of the LED's performance within the array will affect the resist curing times. that is, if the array has poor LED to LED uniformity in terms of output power then the resultant structures will have areas of under and over exposure giving unreliable final results. This can be mitigated with adequate temporal control over the duty cycle of any under- or over-performing elements. As explained in Sec. 1.3, this control can be achieved through the CMOS integration of these LED arrays.
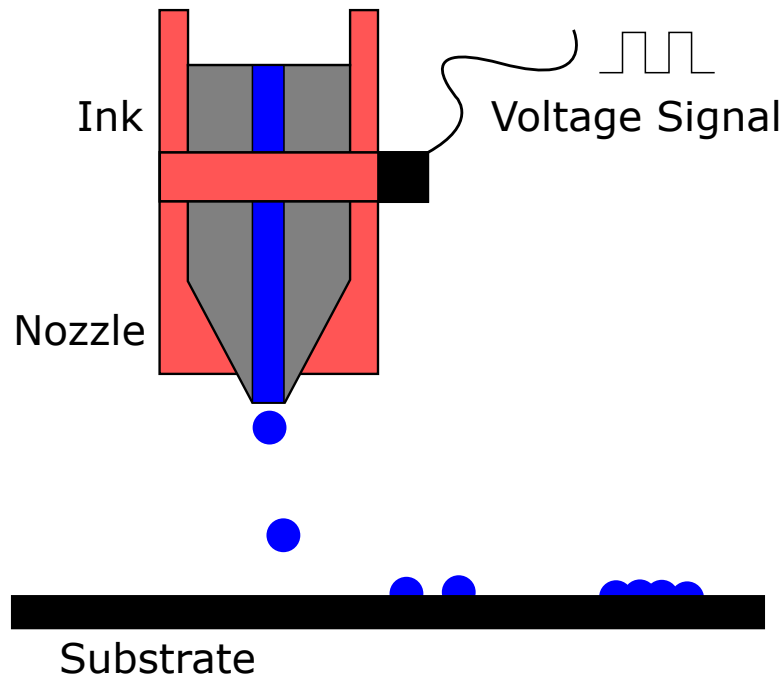
Figure 1.15: A schematic of a ink-jet printing setup.

1.2.2.3 Other Maskless Lithography Techniques

Along with photolithography there are many other methods for micro-patterning. Another common example is 'ink-jet printing'. This method works in the same fashion as common office printers in that a 'nozzle' systematically raster scans the substrate and sprays a small jet of liquid onto each location. The technique is capable of depositing any liquid materials along with any suspended materials within it making it useful for printing quantum dots and even organic materials. A schematic of this system is shown in Fig. 1.15.

The advantage of this technique is that it is mask free and is able to print any liquid material with a low enough viscosity giving a great deal of flexibility. However, the resolution which can be achieved is not only dependant on the volume of material deposited, but also the substrate being used. For untreated surfaces the maximum resolution is typically above 100 μm [49] whilst treated surfaces have been able to produce down to 2 μm features [50]. Another issue with this method is that as any

solvents within the deposited material dries it will encounter the 'coffee ring effect', that results in any deposited materials likely forming rings with high concentration of solids as it dries.

Another potential solution for developing micro-structures is electron beam lithography. This technique is somewhat similar to photolithography in that a resist is exposed in order to alter its solubility, only in this instance it is exposed to a beam of electrons rather than a more conventional light source. In order to generate specific patterns the electron beam is scanned across the substrate surface as required without the need of a hard mask giving a great deal of flexibility. A benefit of using electrons rather than light is the resolution is significantly higher than what is possible with photolithography and can reach a feature size of single digit nano-meters [51] which far exceeds conventional photo-lithography. However, due to the nature of the system it requires a high vacuum for the electron beam to propagate through. This introduces some restrictions on the use of substrate materials, resist materials and can impact the maximum sample size or number of samples which can fit into the vacuum chamber. The requirement also introduces additional issues when it comes to the mass production of devices as each patterning run requires time to produce the vacuum and then bring it back to ambient pressure. Another significant issue which comes with e-beam lithography is the long patterning times which can be over 24 hours per square centimeter [52], although this is highly dependant on the intricacy of the pattern being produced.

1.2.3 Photometric Stereo Imaging

Another practical and common application of light is in imaging. The availability of cameras in smartphones taking high quality 2D images has become a daily occurrence for many. A further advancement on standard photography is to expand its functionality to reconstruct 3D images. This can be achieved either by having an array of cameras, each imaging the object from different angles, or by using a single camera and illuminating the object from different angles. Photometric stereo imaging is a technique
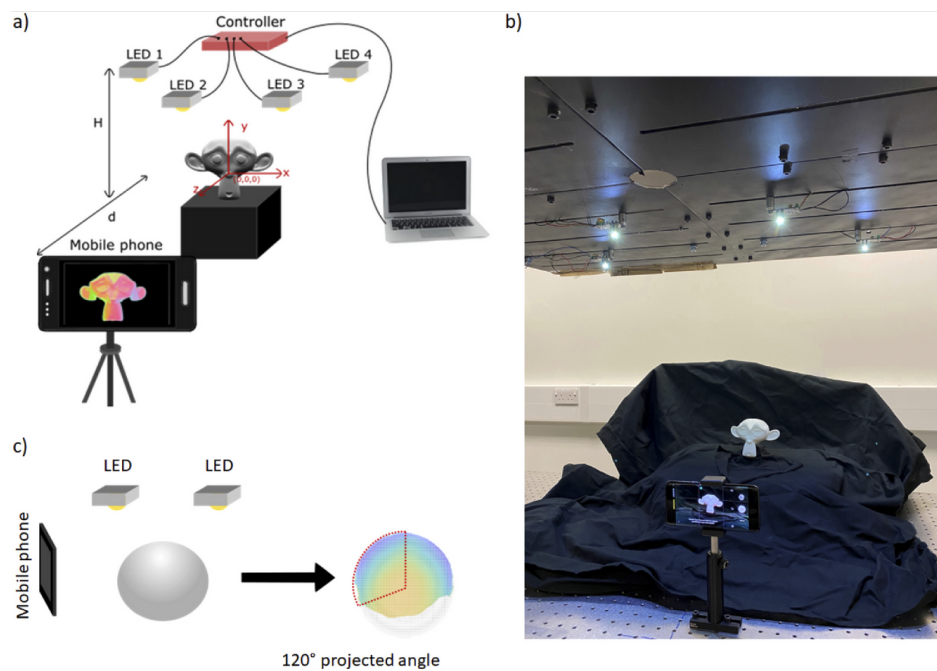
Figure 1.16: a)A schematic of a photometric stereo imaging setup using four light sources each at a different angle to the imaged object. b) An optical image of the setup and c) schematic of the projected angle [55]

that is capable of determining the profile and surface normals of an object whilst being imaged using a single static camera. The technique is enabled by an array of LEDs which are synchronised to the camera and are capable of illuminating the scene from multiple directions as shown in Fig. 1.16 [53]. A particular advantage of this approach is that no assumptions of the surface roughness need to be made, as is required with other 3D imaging techniques [54]. Along with this, for purely surface normal reconstruction, the computational requirements are minimal.

The schematic shown in Fig. 1.16 gives the example from our groups work of using four synchronised LEDs which are independently and sequentially modulated to illuminate the scene with the camera imaging at each interval. Each LED will illuminate the scene in a way that creates a unique and distinct image, with each frame being collated to derive the 3D rendering. This is done by analysing the difference in pixel intensities from images acquired from at least three different illumination directions. The recon-

struction method relies on the Lambertian surface assumption, i.e any incident light is reflected in all directions evenly.

LEDs are good candidates for this style of imaging as they can be modulated at sufficiently high frequency to reduce any visual flicker. They are also able to produce white light giving rise to opportunities for simultaneous general purpose illumination and 3D imaging. This could potentially utilise existing LED based lighting infrastructure due to LED lighting being common in industrial and professional areas/offices. To reduce the visual flicker a high frame rate camera is preferred as the modulation time of each LED is the camera frame rate divided by the total number of emitters. For example a 60 fps camera with four LEDs would have an image update rate of 15 Hz.

1.3 CMOS Electronics

Most of the experimental work presented in this thesis was achieved through the use of custom CMOS electronic drivers developed by colleagues at the University of Edinburgh under Prof. Robert K. Henderson. By directly bump bonding μLED arrays to these drivers they provide a compact and highly controllable system for spatio-temporally patterned optical emission. This section will explain the development and performance capabilities of CMOS electronic drivers.

1.3.1 GaN μLED Array Development

1.3.1.1 Bump Bonding

As discussed in Sec. 1.1.2, GaN μLEDs have been shown to offer high modulation rates and mW-level light output. This in combination with the fabrication of arrays of individually addressable elements creates the opportunity for additional functionality. However, implementing array format devices creates the problem of packaging the device with the required number of contacts. For example, the first example of such a micro-display consisted of a 10×10 array with a common n-contact [56]. This required

100 individual contacts to be fabricated around the array. This becomes more imprac-
tical as larger array dimensions are used, for example the Samsung 146 inch TV called
'The Wall' which uses μLEDs for high frame rates and an 8K resolution. A possible
solution to this issue is to create a matrix addressing system where each column of
pixels shares a common p-contact and each row of pixels shares a common n-contact.
This has the benefit of linearly scaling the number of contacts as the array dimensions
grow instead of scaling quadratically. However this option creates a new problem that
simultaneously addressing multiple pixels may trigger unwanted elements within the
array. This can be addressed by employing appropriate line scanning techniques though
this is slow for large arrays and impacts the LED duty cycle.

Flip-chip bump bonding is a method which allows for the individual addressing of
each pixel whilst not requiring contacts to be fabricated around the array. Using an
electrode of each LED as the contact, traditionally the p-contact due to semiconductor
growth requirements, allows that array to be directly stacked on top of the individual
electronic drivers for each μLED without the requirement of any metal tracks to reach
each element. This also allows for higher density arrays to be fabricated as the space
requirement between pixels is negligible. Flip-chip configuration is achieved by using
gold or indium bump bonds for each LED by mechanically pressing the CMOS driver
and array together. Thermal energy then melts the gold bumps creating a connec-
tion. Providing that the dimensions of the bond pads for each device match, arrays
of arbitrary dimensions can be bonded. This results in a flip-chip format where the
emitted light is extracted through the sapphire LED substrate. This process is shown
schematically in Fig. 1.17.

1.3.1.2   Driver Capabilities

The CMOS driver chip used here comprises 16×16 arrays of individual CMOS drivers
with 100 μm pitch and a 50×50 μm^2 bond pad. The drivers consist of four layers with
the bottom two dedicated to routing signals, the third layer acting as a safety barrier

CMOS device Deposited gold LED Array aligned
              bumps   and bonded
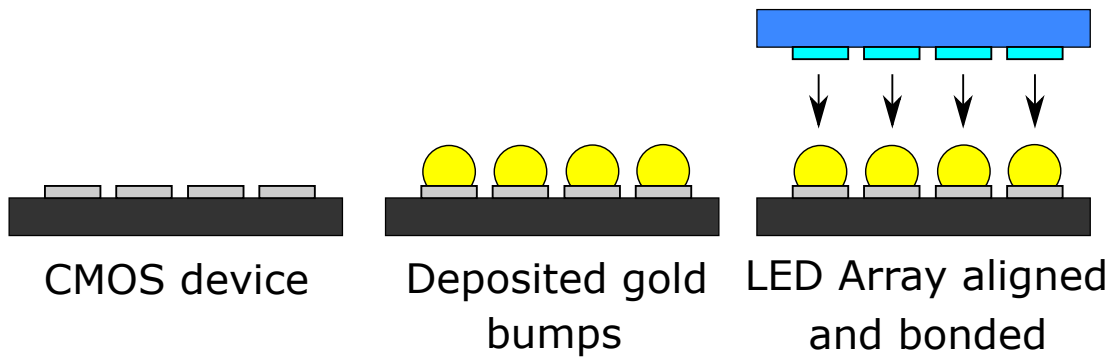
Figure 1.17: A representation of the bump bonding process to connect flip-chip μLEDs with CMOS drivers. The bumps are typically 10's of microns in diameter.

to protect the electronics from the LED voltages and the top layer featuring the bond pads. Due to previous iterations being damaged during the bump bonding process, the electronics for each driver are positioned around the bond pad and not underneath it [57]. Additionally, vertical tungsten columns are located throughout the chip which improve mechanical stability.

Each driver in the CMOS chip has the logic circuitry shown in Fig. 1.18. The inputs defined ROW and COL respectively refer to the row and column of the intended pixel. This means that when a pixel is addressed, a flip-flop output will shadow the driver input (DIN) at the rate defined by the clock (CLK). In this setup the flip-flop will maintain the DIN input even if the pixel is no longer being addressed. The output of the driver is controlled by $INPUT\_SIG$ with the inverse being represented when the pixel is active. $INPUT\_SIG$ can be sourced from either an on-chip voltage controlled oscillator (VCO), a DC signal from the control board, or in the case of the work undertaken here, an external logic signal. Details of the VCO can be found in [58]. The output of the device can be operated in pulsed mode and is controlled by $MODE\_CONTROL$. If $MODE\_CONTROL$ is high then the output will follow $INPUT\_SIG$ directly, however if it is low then $INPUT\_SIG$ will also be sent through an inverter to introduce a time delay. This delay is achieved by current starving the inverter with a transistor, thus allowing it to be controlled with an external voltage ($VBMC2$). The signal is then sent
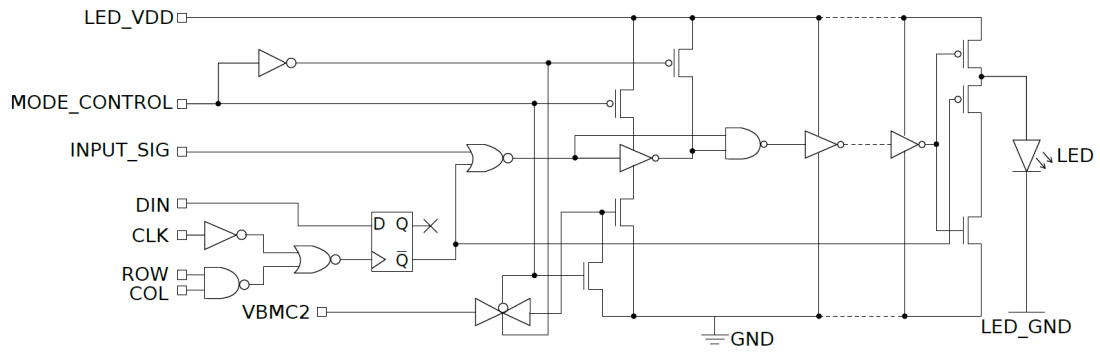
Figure 1.18: The logic circuitry within each CMOS driver [61].

to a NAND gate along with the original *INPUT_SIG* which then drives the LED in short pulse mode [59]. This circuitry has allowed for pulses to be generated down to 300 ps in duration [60].

The chain of inverters used is to reduce the load capacitance on the input signal and to increase the drive strength [59]. It is also important to note that *LED_GND* can be separated from the driver's main ground. This allows for the LEDs to be driven above the usual 3.3 V limit by shifting the LED ground to a negative bias.

1.3.2 Driver boards

To control the CMOS integrated μLED arrays a motherboard was developed by colleagues at the University of Edinburgh. This is shown in Fig. 1.19. This board features a field programmable gate array (FPGA) card, a series of variable resistors to control output voltages and a daughter card. The FPGA acts as a connection between the CMOS drivers and a PC allowing for direct control with MATLAB^{TM}. The daughter card routes the logic signals to the correct CMOS pins along with housing a connection for an external power supply, *INPUT_SIG*. Along with tuning the LED bias voltage, the variable resistors also control *VBMC2* to control optical pulse widths. The USB connection between the FPGA and PC also provides power for the boards.
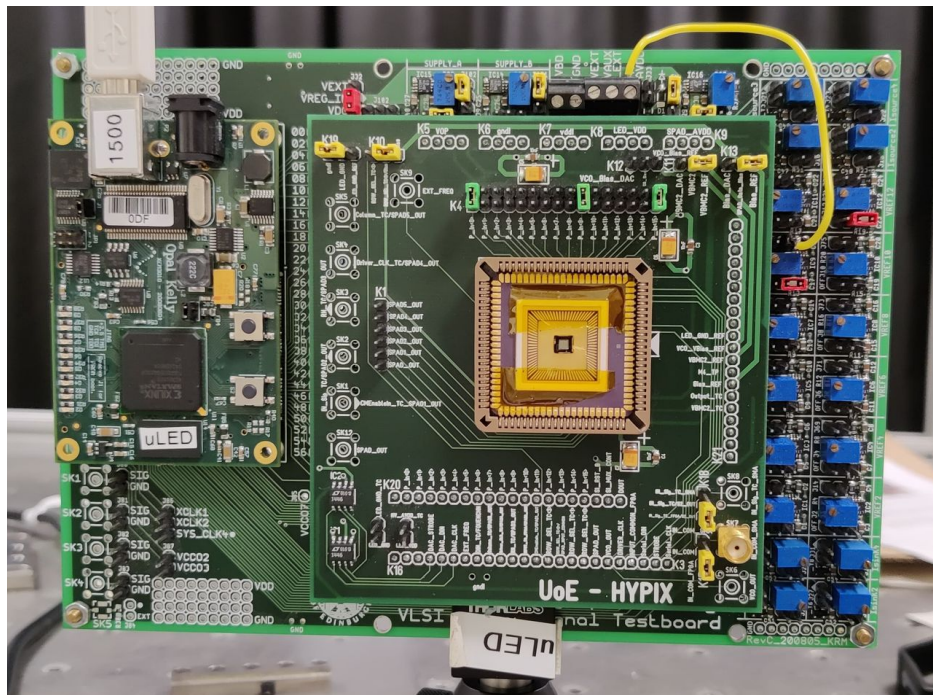
Figure 1.19: A photograph of the motherboard and attached daughter cards for the CMOS integrated LED array.

1.4 Optical Scanning Methods

By illuminating an area with a suitable sequence of spatially modulated light patterns, information may be obtained about the surface of, or the contents, of the field of view (FOV). This concept has applications in areas such as indoor navigation for automated systems [62] and 3D imaging [63]. The basic principle of this can also be easily scaled using suitable optics to meet a variety of requirements across metre to micrometre scale. For example, on the metre scale, this method can track objects or automated vehicles as they move around a warehouse. A promising method of achieving this is through visible light and incorporating VLC style systems to transmit and detect these sequentially projected light patterns patterns. A good example of how this can be performed is through the use of LED arrays or arrays of LED lights, which are common in the ceilings of large commercial spaces, to provide the required light coverage at a high modulation rate. VLC based location and tracking systems systems also have

other advantages over more traditional RF-based systems such as GPS. For example specialised indoor environments may not be compatible with RF [64]. On top of this, as LED technologies are becoming more mainstream and the architectures to utilise these systems are being incorporated into buildings meaning that indoor GPS using lighting can be an additional capability to illumination.

To achieve this functionality there are multiple different techniques which can be utilised. This includes but is not limited to time of arrival, angle of arrival, optical fingerprinting and triangulation. The work presented in this thesis was achieved through the use of triangulation and optical fingerprinting. This method is carried out by exploiting the innate spatio-temporal control of light emission from a μLED array to project specialised patterns in a chequerboard style grid onto an area, as shown in Fig. 1.20. If the series of patterns is chosen carefully, each coordinate within the projected grid will receive a unique binary modulation data stream, or 'fingerprint', which can then be correlated to its physical location [65]. There is a great deal of flexibility in the composition of pattern sequence which is projected and the optimal sequence will vary between applications. Ideally, the optimal sequence will be the minimal number of patterns required to accurately locate a marker, whilst maintaining an acceptably low cross-talk between frames. LEDs are a good candidate for this style of light projection as they are capable of providing flicker free, high frame rate patterns [66], have a low power consumption and are easily integrated into simple driving electronics. They can also be fabricated to meet specific wavelength or size requirements. Furthermore, only simple and inexpensive optics are required to scale the emitted light to create a tailored FOV. Different forms of pattern projection will be discussed in the following section.

1.4.1 Raster Scan

In this example of structured illumination a chequerboard style grid is created within the camera FOV from the projected emission pattern of an LED array. Each element within the LED array illuminates a single grid coordinate and can project its own
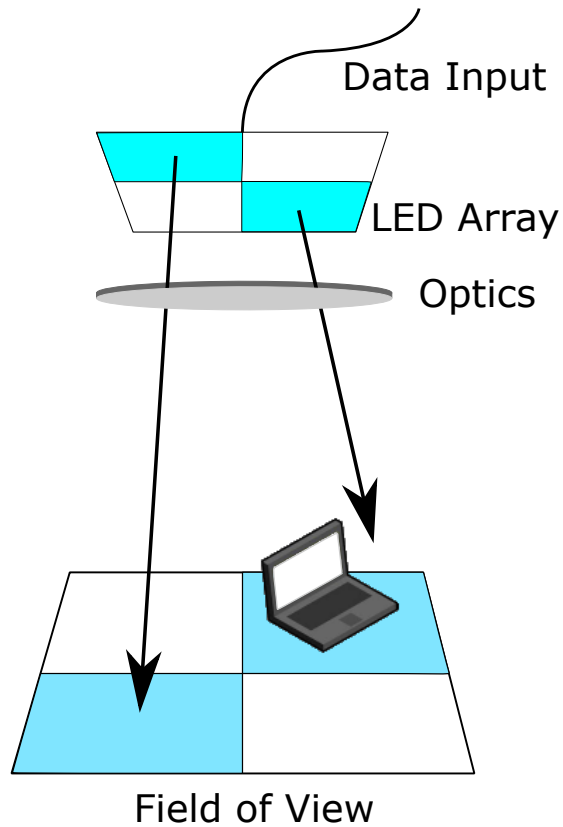
Figure 1.20: An example schematic showing how the spatial layout of an LED array directly translates into a similar checkerboard style layout with each LED representing and illuminating each coordinate within this grid. This creates a coordinate system which directly correlates with the LED row/column addresses.
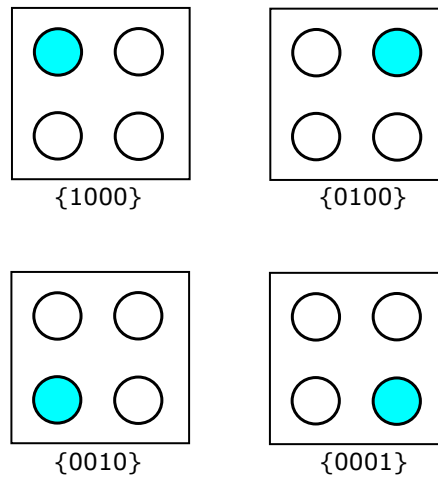
Figure 1.21: A visual representation of a raster scan sequence of illuminating pixels.

contribution to an illumination pattern accordingly. In order to obtain data from each point within this grid with light, each point must have received a unique fingerprint signal from a series of patterns. The easiest and most direct approach to doing this is to perform a raster scan over this area. In this, each individual element of the emitting array will be sequentially and individually modulated. This means that for an array of N emitters, there will be a bit sequence of length N. This is shown schematically in Fig. 1.21. The problem with this technique is that the sequence length scales linearly with the size of the array, meaning that as the size of the array increases, the amount of data which has to be transmitted, collected and analysed also drastically increases. As shown in Fig. 1.21, this is suitable for small arrays, for example a 2×2 array will only require 4 patterns, however a 16 x 16 array requires 256 patterns. This inefficiency is a fundamental problem with this approach as in order to have a higher positioning accuracy during detection, a higher number of grid coordinates is desirable as each coordinate can then be physically smaller within the FOV.

The raster scan technique typically requires synchronisation between the emitter and detector which may not always be practical for some applications. Also, if it were to be used for simultaneous general purpose illumination, the emitters and detectors used would need to be capable of operating at high frame rates. This is because in

order to have flicker-free illumination each element must have a similar duty cycle and the sequence must be completed at a frequency unnoticeable to the human eye [67]. This would again scale linearly with the size of the array and can potentially cause issues due to any limitations in driving speeds.

1.4.2 Induction Search Patterns

If we consider an array where the number of emitters (N) is a power of two, we are able to use a binary encoding scheme for the positional information [68]:

$$N = 2^m \tag{1.6}$$

Where

$$n_{min} \approx 2m \tag{1.7}$$

Here n is the sequence length and m is the power defining the array size. By using an induction method, a unique fingerprint sequence of length 2m can be generated. For example for an array where m = 2, there will be four emitters and a sequence of four patterns can be generated as shown:

$$t^1 = \begin{bmatrix} 1100 \\ 0011 \\ 0110 \\ 1001 \end{bmatrix} \tag{1.8}$$

Where t^1 is the bit sequence for $m = 1$. This is shown graphically in Fig. 1.22. Note that in comparison to the raster scan method, as n scales linearly with m instead of exponentially, the sequence length for larger arrays will be substantially shorter. The μLED arrays used in our work to implement the structured illumination are of 16×16 pixels and the full pattern sequence required is as shown in Fig. 1.23.

As Fig. 1.23 is for an 8 x 8 array, this sequence operates as a series of stripe
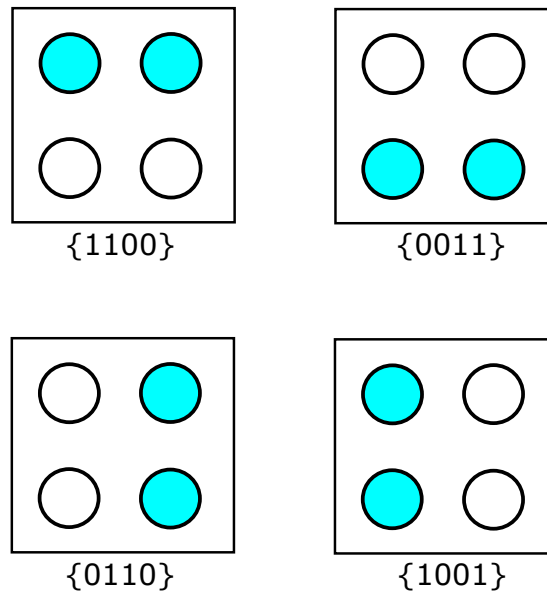
Figure 1.22: A visual representation of the pattern sequence defined by induction methods shown in Equation 1.8

patterns, with the inverse also being included, it is possible to treat the positional data as Manchester encoded bits at the receiver [65]. This not only enables the information to be easily decoded but by projecting the inverse patterns in this fashion it also provides a more robust data set. Along with this it provides uniform illumination onto the FOV should it be required, e.g. to combine illumination and positional fingerprinting. This decoding of this pattern is unusual as it can be done in a binary fashion. This is because the first four patterns in the sequence define quadrants where data can be interpreted. After this the subsequent four patterns define a similar four quadrants, but within each of the previous quadrants and so on. This pattern continues on until the final four patterns define the final precision of operation.

1.4.3 Binary Search Patterns

A more general method of constructing a binary search enabled pattern sequence is possible. This method however has an increased sequence length of $n = 3m$ and is suitable for square arrays of dimensions 2^l x 2^l. First consider the following matrices:
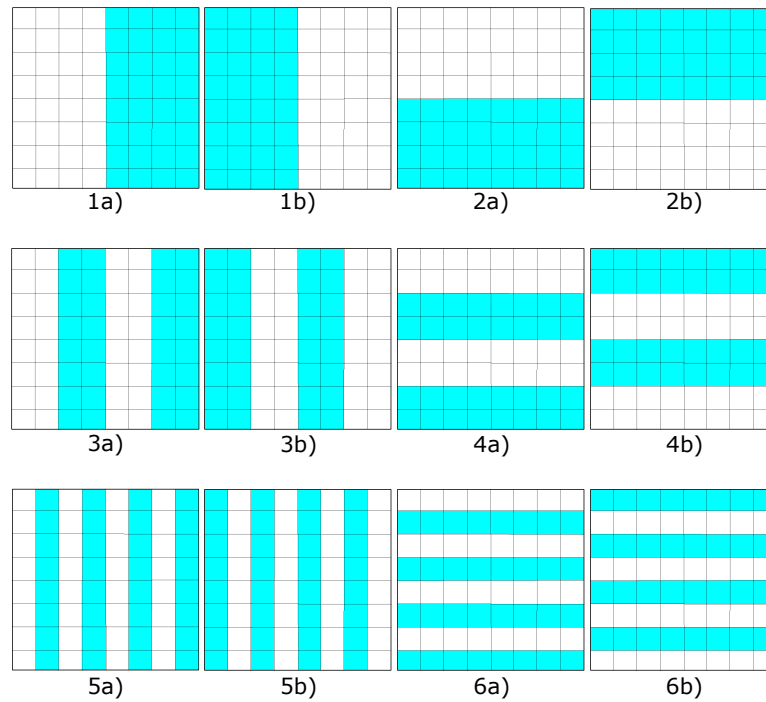
Figure 1.23: A visual representation of the full induction scan pattern for a 8 x 8 LED array. Each pattern is annotated in pairs, one being the inverse of the other.

$$B^1 = \begin{bmatrix} 10 \\ 10 \end{bmatrix} \qquad B^2 = \begin{bmatrix} 11 \\ 00 \end{bmatrix} \qquad B^3 = \begin{bmatrix} 10 \\ 01 \end{bmatrix} \tag{1.9}$$

These matrices correspond to a Hadamard basis and can be used for 2×2 tracking. Previously in Section 1.4.2, a pattern sequence was made using only matrices B^1 and B^2 which produced a sequence of minimal length. Here the inclusion of B^3, and its inverse, increases the length of this sequence whilst improving the reliability, as discussed in 1.4.4. This pattern sequence for a 8×8 array is shown in Fig. 1.24.

1.4.4 Moving Bars

As the induction-generated sequence is of minimal length it means that an error in any individual frame compromises the intended operation. These errors can only be removed through certain filtering methods such as median filtering. Using a longer and
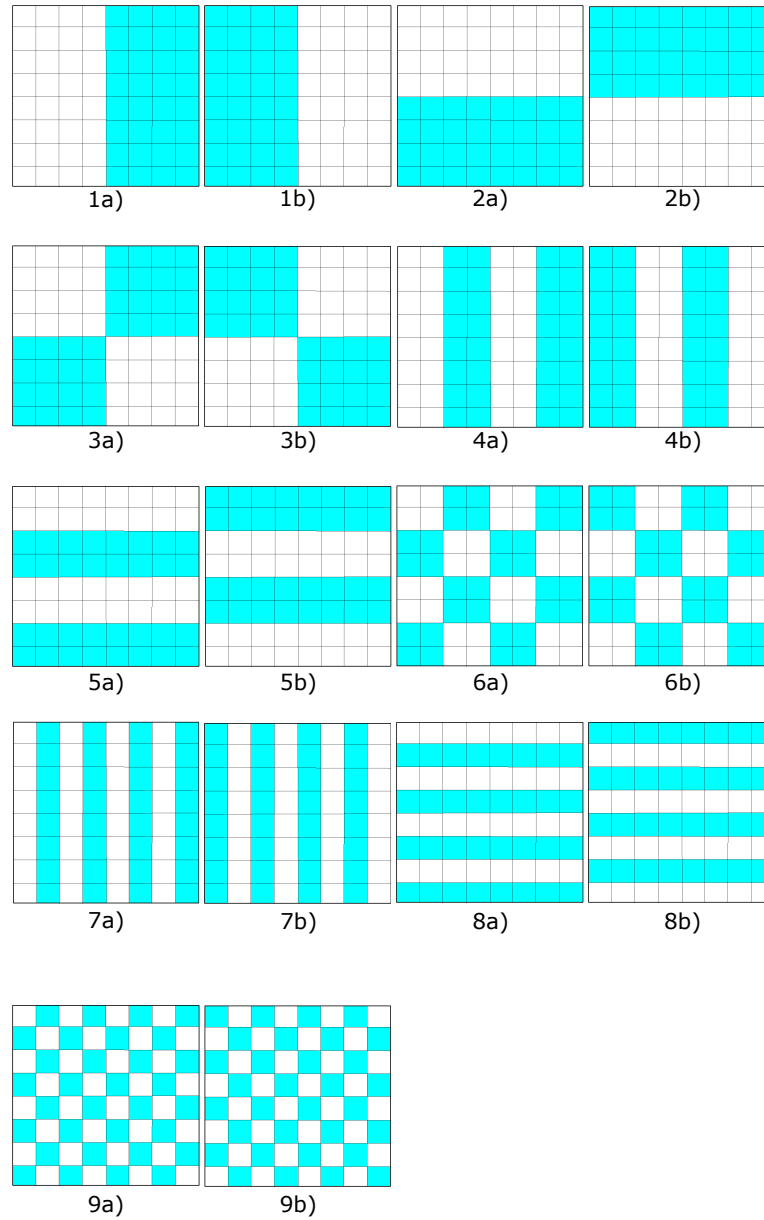
Figure 1.24: A visual representation of the full binary scan pattern for an 8 x 8 LED array. Each pattern is annotated in pairs with each being the pattern and it's inverse.

Table 1.1: A summary of the pattern sequences discussed.

Sequence	Number of Patterns	Figure
Raster Scan	N	1.21
Induction Scan	$2\log_2(\mathrm{N})$	1.23
Binary Scan	$3\log_2(\mathrm{N})$	1.24
Moving Bars Scan	$2\sqrt{N}$	1.25

more robust set of patterns, such as the binary sequence, allows for more sophisticated methods of removing these errors. An example of this can be seen through the position information gained from the binary sequence being obtained with a reverse Hadamard sequence [69].

It can be seen that patterns with low spatial frequencies, referred to as 'coarse', offer better SNR and subsequently a higher differential signal between patterns. The drop in this differential signal when using a finer pattern is caused by both the cross talk between pixels within the array, and by overlapping beam profiles of the emitted light [70,71]. This effect can be avoided by developing a pattern sequence of only coarse patterns which are then spatially shifted instead of becoming finer [68].

With this in mind a sequence can be made which takes the first four patterns in the induction/binary sequence and shifts them horizontally or laterally, essentially scanning the active pixels across the FOV whilst maintaining the 50% active pixel ratio. This sequence is shown in Fig. 1.25 and is known as a moving bars sequence. Although this sequence can be shown to have only coarse spatial shifts, there is a trade off between this having a shorter sequence length which must be considered. Table 1.1 provides a summary of the various pattern sequences discussed.
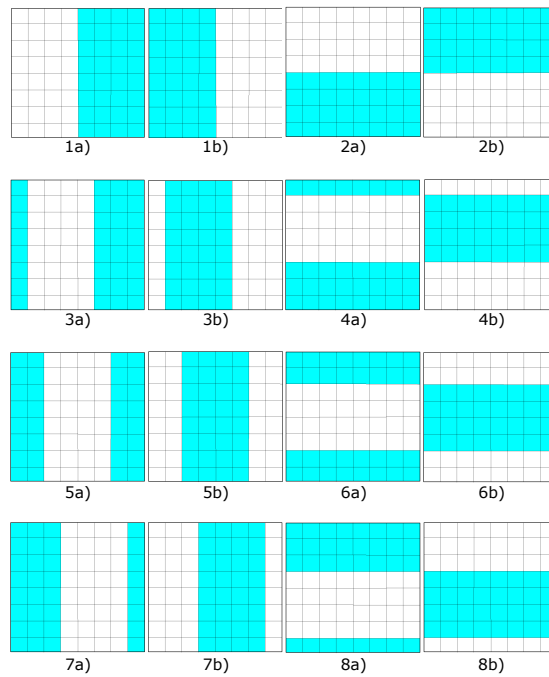
Figure 1.25: A visual representation of the full moving bars scan pattern for a 8 x 8 LED array. Each pattern is annotated in pairs, with each being the inverse of each other.

1.5 Summary

This chapter has introduced the core concepts and relevant background material for the work described in this thesis. This includes the history and operating principles of LEDs which are instrumental throughout, specifically μLEDs and μLED arrays which enable additional functionality due to their size and desirable performance characteristics.

Common data encoding techniques and modulation schemes suitable for μLEDs were also introduced. This included techniques for both single emitters (on/off keying, pulse amplitude modulation, etc.) and arrays of emitters (spatial modulation, wavelength division multiplexing, etc.). Due to the inherent opto-electronic properties of LEDs, they allow for multiple schemes to run simultaneously giving flexibility in their implementation. The basic concepts of photolithography were discussed along with the limitations and how they can be addressed through the use of μLEDs. This includes the ability to create maskless systems which are both reliable and low cost. The use

of CMOS driving electronics for directly controlling the μLED arrays used throughout this thesis was highlighted and explained. By using these drivers, high fidelity devices can be used to project structured illumination pattern sequences, and this was also discussed. The characteristics of these patterns was introduced along with the important trade off between high resolution/accuracy and pattern length.

Bibliography

[1] H. J. Round, "Light-emitting diodes hit the centenary milestone," *World*, vol. 19, p. 309, 1907.

[2] N. Zheludev, "The life and times of the LED—a 100-year history," *Nature photonics*, vol. 1, no. 4, p. 189, 2007.

[3] O. Lossev, "CII. Luminous carborundum detector and detection effect and oscillations with crystals," *The London, Edinburgh, and Dublin Philosophical Magazine and Journal of Science*, vol. 6, no. 39, pp. 1024–1044, 1928.

[4] N. Holonyak Jr and S. Bevacqua, "Coherent (visible) light emission from ga (as1-x p x) junctions," *Applied Physics Letters*, vol. 1, no. 4, pp. 82–83, 1962.

[5] E. F. Schubert, "Light-emitting diodes Cambridge University Press," *New York*, pp. 35–40, 2006.

[6] H. Rupprecht, J. Woodall, and G. Pettit, "Efficient visible electrolumenescence at 300 K from Ga1-x Al x As p-n junctions grown by liquid-phase epitaxy," *Applied Physics Letters*, vol. 11, no. 3, pp. 81–83, 1967.

[7] J. Pankove and J. Berkeyheiser, "A light source modulated at microwave frequencies," *IRE Transactions on Electron Devices*, vol. 9, no. 6, pp. 503–503, 1962.

[8] S. Lang and B. Siskind, "Digital video surveillance system," Feb. 14 2008. US Patent App. 11/891,381.

Bibliography

[9] Y. Mendelson and B. D. Ochs, "Noninvasive pulse oximetry utilizing skin reflectance photoplethysmography," *IEEE Transactions on Biomedical Engineering*, vol. 35, no. 10, pp. 798–805, 1988.

[10] W. Groves, A. Herzog, and M. Craford, "The Effect of Nitrogen Doping on GaAs1-x P x Electroluminescent Diodes," *Applied Physics Letters*, vol. 19, no. 6, pp. 184–186, 1971.

[11] R. Logan, H. White, and W. Wiegmann, "EFFICIENT GREEN ELECTROLUMINESCENCE IN NITROGEN-DOPED GaP p-n JUNCTIONS," *Applied Physics Letters*, vol. 13, no. 4, pp. 139–141, 1968.

[12] E. F. Schubert, *Light-emitting diodes.* E. Fred Schubert, 2018.

[13] S. Nakamura and S. F. Chichibu, *Introduction to nitride semiconductor blue lasers and light emitting diodes.* CRC Press, 2000.

[14] T.-Y. Seong, J. Han, H. Amano, and H. Morkoç, *III-Nitride based light emitting diodes and applications.* Springer, 2013.

[15] S. Nakamura, S. Pearton, and G. Fasol, *The blue laser diode: the complete story.* Springer Science & Business Media, 2000.

[16] M. H. Crawford, "LEDs for solid-state lighting: performance challenges and recent advances," *IEEE Journal of Selected Topics in Quantum Electronics*, vol. 15, no. 4, pp. 1028–1040, 2009.

[17] I. Akasaki, H. Amano, and S. Nakamura, "The Nobel Prize in Physics 2014," *Nobelprize. org. Nobel Media AB (2014)*, 2014.

[18] J. K. Kim and E. F. Schubert, "Transcending the replacement paradigm of solid-state lighting," *Optics Express*, vol. 16, no. 26, pp. 21835–21842, 2008.

[19] M. D. Al-Amri, M. El-Gomati, and M. S. Zubairy, *Optics in Our Time.* Springer International Publishing, 2016.

Bibliography

[20] R. X. Ferreira, E. Xie, J. J. McKendry, S. Rajbhandari, H. Chun, G. Faulkner, S. Watson, A. E. Kelly, E. Gu, R. V. Penty, *et al.*, "High bandwidth GaN-based micro-LEDs for multi-Gb/s visible light communications," *IEEE Photonics Technology Letters*, vol. 28, no. 19, pp. 2023–2026, 2016.

[21] P. H. Pathak, X. Feng, P. Hu, and P. Mohapatra, "Visible light communication, networking, and sensing: A survey, potential and challenges," *IEEE communications surveys & tutorials*, vol. 17, no. 4, pp. 2047–2077, 2015.

[22] S. Rajbhandari, J. J. McKendry, J. Herrnsdorf, H. Chun, G. Faulkner, H. Haas, I. M. Watson, D. O'Brien, and M. D. Dawson, "A review of gallium nitride LEDs for multi-gigabit-per-second visible light data communications," *Semiconductor Science and Technology*, vol. 32, no. 2, p. 023001, 2017.

[23] T.-H. Do and M. Yoo, "An in-depth survey of visible light communication based positioning systems," *Sensors*, vol. 16, no. 5, p. 678, 2016.

[24] M. Stonehouse, A. Blanchard, B. Guilhabert, I. M. Watson, E. Gu, J. Herrnsdorf, and M. D. Dawson, "Microscale automated alignment and spatial tracking through structured illumination," in *2019 IEEE Photonics Conference (IPC)*, pp. 1–2, IEEE, 2019.

[25] N. McAlinden, D. Massoubre, E. Richardson, E. Gu, S. Sakata, M. D. Dawson, and K. Mathieson, "Thermal and optical characterization of micro-LED probes for in vivo optogenetic neural stimulation," *Optics letters*, vol. 38, no. 6, pp. 992–994, 2013.

[26] D. Halliday, R. Resnick, and J. Walker, *Fundamentals of physics*. John Wiley & Sons, 2013.

[27] Y.-H. Liang and E. Towe, "Progress in efficient doping of high aluminum-containing group iii-nitrides," *Applied Physics Reviews*, vol. 5, no. 1, p. 011107, 2018.

[28] K. Takeda, M. Iwaya, T. Takeuchi, S. Kamiyama, and I. Akasaki, "Electrical properties of n-type algan with high si concentration," *Japanese Journal of Applied Physics*, vol. 55, no. 5S, p. 05FE02, 2016.

[29] F. Hamdani, A. Botchkarev, W. Kim, H. Morkoç, M. Yeadon, J. Gibson, S.-C. Tsen, D. J. Smith, D. C. Reynolds, D. C. Look, *et al.*, "Optical properties of GaN grown on ZnO by reactive molecular beam epitaxy," *Applied physics letters*, vol. 70, no. 4, pp. 467–469, 1997.

[30] D. Zhao, S. Xu, M. Xie, S. Tong, and H. Yang, "Stress and its effect on optical properties of GaN epilayers grown on Si (111), 6H-SiC (0001), and c-plane sapphire," *Applied physics letters*, vol. 83, no. 4, pp. 677–679, 2003.

[31] H. Amano, N. Sawaki, I. Akasaki, and Y. Toyoda, "Metalorganic vapor phase epitaxial growth of a high quality GaN film using an AlN buffer layer," *Applied Physics Letters*, vol. 48, no. 5, pp. 353–355, 1986.

[32] S. Lester, F. Ponce, M. Craford, and D. Steigerwald, "High dislocation densities in high efficiency GaN-based light-emitting diodes," *Applied Physics Letters*, vol. 66, no. 10, pp. 1249–1251, 1995.

[33] T. Sochacki, Z. Bryan, M. Amilusik, M. Bobea, M. Fijalkowski, I. Bryan, B. Lucznik, R. Collazo, J. L. Weyher, R. Kucharski, *et al.*, "Hvpe-gan grown on mocvd-gan/sapphire template and ammonothermal gan seeds: Comparison of structural, optical, and electrical properties," *Journal of crystal growth*, vol. 394, pp. 55–60, 2014.

[34] R. B. Jain and H. P. Maruska, "How it really happened: The history of p-type doping of gallium nitride," *physica status solidi (a)*, vol. 204, no. 6, pp. 1970–1976, 2007.

Bibliography

[35] H. Amano, M. Kito, K. Hiramatsu, and I. Akasaki, "P-type conduction in mg-doped gan treated with low-energy electron beam irradiation (leebi)," *Japanese Journal of Applied Physics*, vol. 28, no. 12A, p. L2112, 1989.

[36] J. Rehr, "Recent developments in multiple-scattering calculations of XAFS and XANES," *Japanese Journal of Applied Physics*, vol. 32, no. S2, p. 8, 1993.

[37] E. Xie, M. Stonehouse, R. Ferreira, J. J. McKendry, J. Herrnsdorf, X. He, S. Rajbhandari, H. Chun, A. V. Jalajakumari, O. Almer, *et al.*, "Design, fabrication, and application of GaN-based micro-LED arrays with individual addressing by N-electrodes," *IEEE Photonics Journal*, vol. 9, no. 6, pp. 1–11, 2017.

[38] S. Jin, J. Shakya, J. Lin, and H. Jiang, "Size dependence of III-nitride microdisk light-emitting diode characteristics," *Applied Physics Letters*, vol. 78, no. 22, pp. 3532–3534, 2001.

[39] Z. Gong, S. Jin, Y. Chen, J. McKendry, D. Massoubre, I. M. Watson, E. Gu, and M. D. Dawson, "Size-dependent light output, spectral shift, and self-heating of 400 nm InGaN light-emitting diodes," *Journal of Applied Physics*, vol. 107, no. 1, p. 013103, 2010.

[40] S. Jin, J. Li, J. Lin, and H. Jiang, "InGaN/GaN quantum well interconnected microdisk light emitting diodes," *Applied Physics Letters*, vol. 77, no. 20, pp. 3236–3238, 2000.

[41] M. Monavarian, A. Rashidi, A. Aragon, S. Oh, A. Rishinaramangalam, S. DenBaars, and D. Feezell, "Impact of crystal orientation on the modulation bandwidth of InGaN/GaN light-emitting diodes," *Applied Physics Letters*, vol. 112, no. 4, p. 041104, 2018.

[42] S. Zhang, S. Watson, J. J. McKendry, D. Massoubre, A. Cogman, E. Gu, R. K. Henderson, A. E. Kelly, and M. D. Dawson, "1.5 Gbit/s multi-channel visible light

communications using CMOS-controlled GaN-based LEDs," *Journal of Lightwave Technology*, vol. 31, no. 8, pp. 1211–1216, 2013.

[43] W.-C. Lai, S. Chakravarty, Y. Zou, and R. T. Chen, "Silicon nano-membrane based photonic crystal microcavities for high sensitivity bio-sensing," *Optics letters*, vol. 37, no. 7, pp. 1208–1210, 2012.

[44] P. J. Winzer, "Spatial multiplexing: The next frontier in network capacity scaling," in *IET Conference Proceedings*, The Institution of Engineering & Technology, 2013.

[45] N. Jindal, "High SNR analysis of MIMO broadcast channels," in *Proceedings. International Symposium on Information Theory, 2005. ISIT 2005.*, pp. 2310–2314, IEEE, 2005.

[46] J. Bernasconi, T. Scharf, U. Vogler, and H. P. Herzig, "High-power modular LED-based illumination systems for mask-aligner lithography," *Optics express*, vol. 26, no. 9, pp. 11503–11512, 2018.

[47] D. Elfström, B. Guilhabert, J. McKendry, S. Poland, Z. Gong, D. Massoubre, E. Richardson, B. Rae, G. Valentine, G. Blanco-Gomez, *et al.*, "Mask-less ultraviolet photolithography based on CMOS-driven micro-pixel light emitting diodes," *Optics Express*, vol. 17, no. 26, pp. 23522–23529, 2009.

[48] B. Guilhabert, D. Massoubre, E. Richardson, J. J. McKendry, G. Valentine, R. K. Henderson, I. M. Watson, E. Gu, and M. D. Dawson, "Sub-micron lithography using InGaN micro-LEDs: mask-free fabrication of LED arrays," *IEEE Photonics Technology Letters*, vol. 24, no. 24, pp. 2221–2224, 2012.

[49] T. H. Van Osch, J. Perelaer, A. W. de Laat, and U. S. Schubert, "Inkjet printing of narrow conductive tracks on untreated polymeric substrates," *Advanced Materials*, vol. 20, no. 2, pp. 343–345, 2008.

[50] T. Sekitani, Y. Noguchi, U. Zschieschang, H. Klauk, and T. Someya, "Organic transistors manufactured using inkjet technology with subfemtoliter accuracy," *Proceedings of the National Academy of Sciences*, vol. 105, no. 13, pp. 4976–4980, 2008.

[51] Y. Chen, "Nanofabrication by electron beam lithography and its applications: A review," *Microelectronic Engineering*, vol. 135, pp. 57–72, 2015.

[52] K. Li, J. Li, C. Reardon, C. S. Schuster, Y. Wang, G. J. Triggs, N. Damnik, J. Müenchenberger, X. Wang, E. R. Martins, *et al.*, "High speed e-beam writing for large area photonic nanostructures—a choice of parameters," *Scientific reports*, vol. 6, no. 1, pp. 1–10, 2016.

[53] Y. Zhang, G. M. Gibson, R. Hay, R. W. Bowman, M. J. Padgett, and M. P. Edgar, "A fast 3D reconstruction system with a low-cost camera accessory," *Scientific reports*, vol. 5, no. 1, pp. 1–7, 2015.

[54] B. Sun, M. P. Edgar, R. Bowman, L. E. Vittert, S. Welsh, A. Bowman, and M. Padgett, "3D computational imaging with single-pixel detectors," *Science*, vol. 340, no. 6134, pp. 844–847, 2013.

[55] E. Le Francois, J. Herrnsdorf, J. J. McKendry, L. Broadbent, G. Wright, M. D. Dawson, and M. J. Strain, "Synchronization-free top-down illumination photometric stereo imaging using light-emitting diodes and a mobile device," *Optics Express*, vol. 29, no. 2, pp. 1502–1515, 2021.

[56] H. Jiang, S. Jin, J. Li, J. Shakya, and J. Lin, "III-nitride blue microdisplays," *Applied Physics Letters*, vol. 78, no. 9, pp. 1303–1305, 2001.

[57] J. J. McKendry, D. Massoubre, S. Zhang, B. R. Rae, R. P. Green, E. Gu, R. K. Henderson, A. Kelly, and M. D. Dawson, "Visible-light communications using a CMOS-controlled micro-light-emitting-diode array," *Journal of Lightwave Technology*, vol. 30, no. 1, pp. 61–67, 2011.

Bibliography

[58] J. Mckendry, *Micro-pixellated AlInGaN light-emitting diode arrays for optical communications and time-resolved uorescence lifetime measurements.* PhD thesis, University of Strathclyde, 2011.

[59] B. Rae, *Micro-systems for time-resolved fluorescence analysis using CMOS single photon avalanche diodes and micro-LEDs.* PhD thesis, University of Edinburgh, 2009.

[60] J. J. McKendry, B. R. Rae, Z. Gong, K. R. Muir, B. Guilhabert, D. Massoubre, E. Gu, D. Renshaw, M. D. Dawson, and R. K. Henderson, "Individually addressable AlInGaN micro-LED arrays with CMOS control and subnanosecond output pulses," *IEEE Photonics Technology Letters*, vol. 21, no. 12, pp. 811–813, 2009.

[61] A. D. Griffiths, *Novel optical communications and imaging enabled by CMOS interfaced LED technology.* PhD thesis, University of Strathclyde, 1968.

[62] G. Fu, A. Menciassi, and P. Dario, "Development of a low-cost active 3D triangulation laser scanner for indoor navigation of miniature mobile robots," *Robotics and Autonomous Systems*, vol. 60, no. 10, pp. 1317–1326, 2012.

[63] E. Le Francois, J. Herrnsdorf, L. Broadbent, M. D. Dawson, and M. J. Strain, "Top-down illumination photometric stereo imaging using light-emitting diodes and a mobile device," in *Laser Science*, pp. JTu3A–106, Optical Society of America, 2019.

[64] M. Lamey, B. Burke, E. Blosser, S. Rathee, N. De Zanche, and B. Fallone, "Radio frequency shielding for a linac-MRI system," *Physics in Medicine & Biology*, vol. 55, no. 4, p. 995, 2010.

[65] J. Herrnsdorf, M. J. Strain, E. Gu, R. K. Henderson, and M. D. Dawson, "Positioning and space-division multiple access enabled by structured illumination with light-emitting diodes," *Journal of Lightwave Technology*, vol. 35, no. 12, pp. 2339–2345, 2017.

Bibliography

[66] J. Herrnsdorf, J. J. McKendry, E. Xie, M. J. Strain, I. M. Watson, E. Gu, and M. D. Dawson, "High speed spatial encoding enabled by CMOS-controlled micro-LED arrays," in *2016 IEEE photonics society summer topical meeting series (SUM)*, pp. 173–174, IEEE, 2016.

[67] M. C. Potter, B. Wyble, C. E. Hagmann, and E. S. McCourt, "Detecting meaning in RSVP at 13 ms per picture," *Attention, Perception, & Psychophysics*, vol. 76, no. 2, pp. 270–279, 2014.

[68] J. Herrnsdorf, M. D. Dawson, and M. J. Strain, "Positioning and data broadcasting using illumination pattern sequences displayed by LED arrays," *IEEE Transactions on Communications*, vol. 66, no. 11, pp. 5582–5592, 2018.

[69] J. Herrnsdorf, M. J. Strain, E. Gu, and M. D. Dawson, "Concept of a GaN-LED-based positioning system using structured illumination," in *2015 IEEE Photonics Conference (IPC)*, pp. 28–29, IEEE, 2015.

[70] Z. Zhang, X. Wang, G. Zheng, and J. Zhong, "Hadamard single-pixel imaging versus Fourier single-pixel imaging," *Optics express*, vol. 25, no. 16, pp. 19619–19639, 2017.

[71] M.-J. Sun, M. P. Edgar, D. B. Phillips, G. M. Gibson, and M. J. Padgett, "Improving the signal-to-noise ratio of single-pixel imaging using digital microscanning," *Optics express*, vol. 24, no. 10, pp. 10476–10485, 2016.

Chapter 2

Combined functionality through structured LED illumination

This chapter will detail the work regarding novel LED technologies including the fabrication techniques and applications. The simplicity and versatility of LEDs allows them to be tailored and fabricated to any specialised applications. With this in mind the development of CMOS integrated μLED arrays with common n-electrodes will be discussed. These devices are more compatible with negative-channel metal oxide semiconductor (NMOS) transistors which are both faster and smaller than their positive-channel metal oxide semiconductor (PMOS) equivalent. Along with this, with the advances in semiconductor growth methods and materials, the creation of devices which can emit in the deep UV will be discussed due to their usefulness in many applications ranging from photocuring to bio-medical science and inter-satellite communication. Finally a photo-metric stereo imaging setup will be detailed, which uses commercially available broad area LEDs to produce 3-dimensional images of objects with an arbitrarily placed camera. This system is also capable of using the same LED array to track a target or photo detector within a spatial plane.

2.1   N-Contact LED Arrays

LED arrays can be fabricated using many different methods to produce devices capable of different tasks. Here, individually addressable N-contact μLED arrays are developed with the goal of incorporating them with NMOS transistors in custom CMOS drivers. Importantly, the fabrication methodology results in improvements due to allowing the use of both faster and physically smaller driving electronics. This in turn allows the innately high modulation bandwidths of μLEDs to be more fully utilised than was the case with the more limited PMOS transistor based driving circuitry.

2.1.1   Motivations

The inherent high current and optical power densities of μLEDs, when compared to conventional broad area devices, makes them ideal for high speed applications [1–3]. More recently, as fabrication methodology matures and more specialised devices become available, different addressing schemes for μLED arrays have been demonstrated [4–6]. As described in Chapter 1, an active driving scheme can be utilised through the integration of CMOS electronic drivers with LED arrays whilst operating the array in a flip-chip format [2, 7]. This CMOS integration allows significantly greater control over both the spatial and temporal emission of the LED array when compared to matrix addressing schemes. However, typical μLED arrays have some drawbacks when attempting to implement this scheme. These problems stem from the fact that generally μLED arrays are designed to have a common cathode (n-electrode) and individually addressable anodes (p-electrode), as shown in Fig. 1.3. This is also a common GaN LED structure due to the necessity to grow the p-side of the junction on top of the wafer due to several growth issues as well as lower conductivity of p-doped GaN [8]. Another problem with this layout comes from every pixel having a shared n-contact and conductive path, which means that every element within the array has a different conductive path length. This in turn results in the series resistance for each pixel

being different purely because of the n-type mesa. This continual change in resistance across the array results in non-uniform currents for similar applied voltages, as well as increased crosstalk between pixels [9] and non-uniform optical emission [5]. Although this resistance is somewhat dominated by the resistance of the p-GaN contact, it is still a design aspect which can be optimised.

Having p-type contacts for each pixel also creates problems when choosing a suitable driver. In order to correctly connect the source, drain and body contact of any driving MOSFET transistors, it restricts the CMOS electronics to using positively doped MOS (PMOS) transistors. The issue with this is that the carrier mobility of the majority carriers in PMOS transistors (holes) is substantially lower than the mobility of the majority carriers (electrons) in the NMOS alternative. For example the mobility of holes in Si doped at 10^{15} is $\approx 450cm^2/V.s$ and the mobility of electrons in Si doped at 10^{15} is $\approx 1500cm^2/V.s$ [8]. Because of this, not only are the operating speeds of PMOS transistors lower than that of NMOS transistors, but they also require PMOS devices to be physically larger in order to achieve a similar current driving capability. Consequently this leads to additional problems such as having larger device capacitance which further reduces the operating speeds of the CMOS device [10]. Due to the operating speeds of the driving electronics being the bottleneck in the implementation of modern μLEDs in conjunction with the pixel size and pitch within the array being limited by the size of the drivers, these limitations in PMOS electronics are severe. As such it is advantageous to create a device which is suitable for the implementation of NMOS drivers.

Here we present the implementation and characterisation of a novel GaN μLED array which features individually addressable n-electrodes and a common p-electrode along with its fabrication methodology. Arrays fabricated in this way show over 2 mW of optical power emission and 440 MHz modulation bandwidth for a single pixel. Each pixel within the array has a 24 μm diameter and the devices were fabricated with a 450 nm wavelength wafer. This work also shows the integration with a custom made
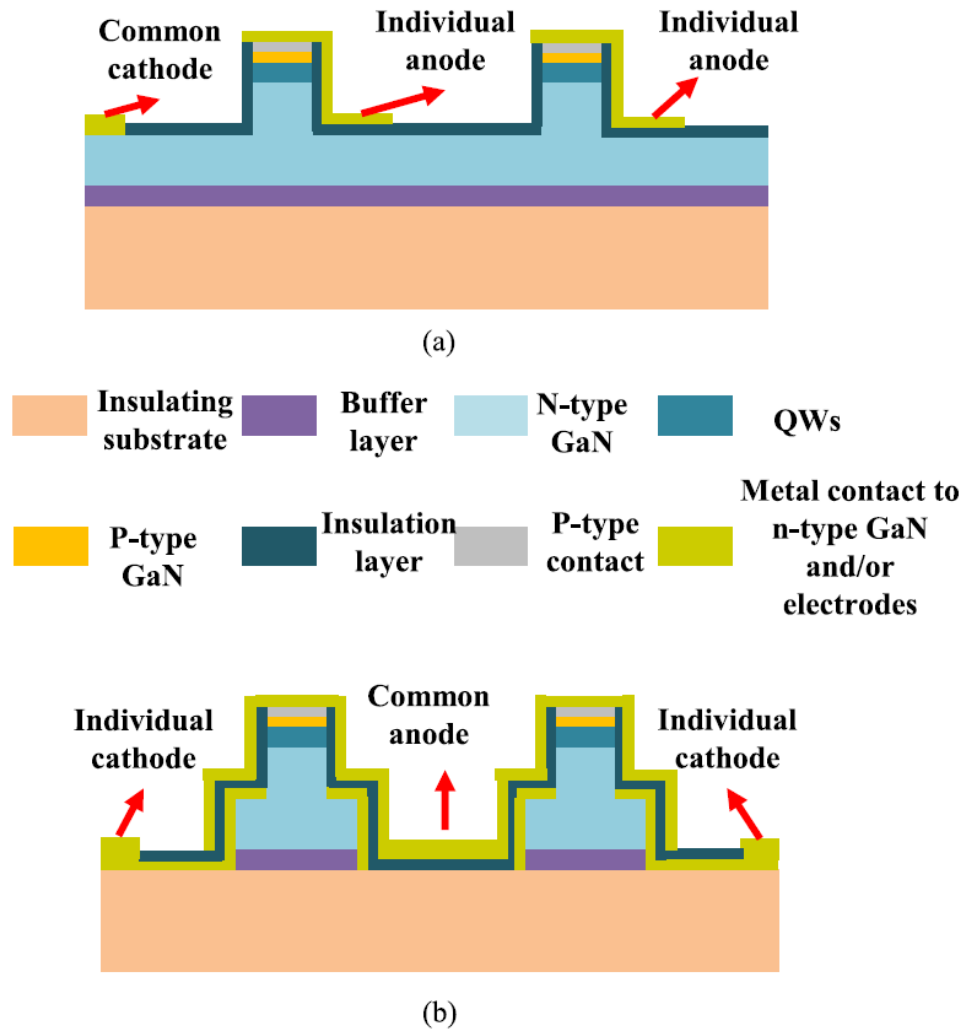
Figure 2.1: A simplified side-view schematic of the material structure in a) a conventional μLED array and b) the n-addressable version [11].

NMOS based CMOS driver which is capable of individually modulating each pixel with various driving schemes. The fabrication of the LED array was performed by Dr Enyuan Xie at the Institute of Photonics and the custom NMOS driver was developed at the University of Edinburgh as part of a collaborative effort.

2.1.2 LED Design and Fabrication

The μLED arrays were grown on a c-plane (0001) sapphire substrate and were fabricated using blue III-nitride wafers. These devices were operated in flip-chip format, meaning that the light is extracted through the sapphire substrate during operation, so the backside of the sapphire was polished prior to fabrication. The epitaxial structure comprises a 3.4 μm thick undoped buffer layer, a 2.6 μm thick n-type GaN layer (which also functions as the contact for the NMOS drivers), eleven quantum wells of InGaN (2.8 nm)/GaN (13.5 nm) which emit at 450 nm, a 30 nm thick p-type AlGaN electron blocking layer and a 160 nm thick p-type GaN layer (common anode). The p-type GaN is kept thin due to its low carrier mobility. The final device consists of a 6x6 array of μLEDs with each pixel being 24 μm in diameter with a 300 μm pitch. As mentioned in Sec. 2.1.1, Fig. 2.1a shows an example schematic of a typical μLED array which features individually addressable p-type contacts. The isolation of each LED element here is achieved by etching down to the n-doped GaN layer. By doing this the N-type GaN is connected to all of the individual μLEDs and acts as a common electrode whilst maintaining the ability to be individually modulated by the now etched-through p-contact. In order to alter this to have addressable n-contacts, each pixel must also be completely isolated from the adjacent n-type GaN layers, as shown in Fig. 2.1b. This can be achieved through two different Cl_2 based plasma etchings of the GaN, as shown in Fig. 2.2a/b. The first of these etches defines the 6x6 array of individual pixels and etches all the way to the sapphire substrate. This produces square mesas with a side wall of 130 μm and is achieved by ICP etching, Fig. 2.2a. Although this results in a mesa separation of 170 μm, this etching process has also been successfully applied to

arrays with a mesa separation of only 6 μm. The second etch defines the individual LED element at the centre of each mesa. These elements are 24 μm in diameter and this is achieved with another ICP etch which this time stops at the n-type GaN layer to allow for a suitable n-contact to be made, as shown in Fig. 2.2b. These two separate etching processes allow for the complete isolation of both the p and n type layers and also ensure the same contact area for each of the n-electrodes.

After the two ICP etches, a quasi-ohmic contact is grown on the p-type GaN by evaporating a 100 nm Pd layer and then thermally annealing it at 300 °C in a N_2 atmosphere. Metallisation of the n-type GaN contact is achieved by sputtering a 50-200 nm thick bilayer of TiAu and a subsequent lift-off process. This process is also used to simultaneously create bilayer tracks which are used to address each pixel independently, as shown in Fig. 2.2c. The photoresists used in the lift-off process were 'Dow Megaposit^{TM} SPR220 4.5' (a positive resist) and 'Micro Resist Technology ma-N 1420' (a negative resist). Initially this was developed using 1-methyl-2-pyrrolidone whilst either heated to 120 °C or ultrasonicated, in addition to acetone and methanol. This solvent based treatment is able to successfully remove any photoresist residue although it offers a low operational pixel yield. A more optimised process used an O_2-based plasma at 200 °C in a plasma asher (Matrix 105 system) to clean photoresist residue. This step was found to be critical in optimising the pixel yield and the uniformity of the electro-optical characteristics of the arrays.

After the cleaning process, a 300 nm thick SiO_2 insulation layer is deposited through plasma enhanced chemical vapour deposition (CVD). This layer is then selectively removed from the top of each pixel to allow for the p-contact to be made. Next, another TiAu bilayer is deposited which interconnects all of the p-electrodes forming a common p-type mesa. This is illustrated in Fig. 2.2d by the shaded areas. Here the distances between the common electrodes for each pixel and the pixel itself are still different throughout the array, however due to the fact the connections are made with a TiAu bilayer instead of n-type GaN the varied series resistance is minimised due to

its substantially lower sheet resistance. This improves on this previous problem shown in more typical μLED array structures.

2.1.3   NMOS Driver

A custom built CMOS driver based on NMOS transistors was developed for this work. This driver features four independent current steering 8-bit DAC channels. Each of these channels are capable of sinking up to 255 mA and can operate at 250 MHz [12]. In order to attach the μLED device to the CMOS drivers it is first wire bonded to a commercially available ceramic package which is in turn soldered onto a daughter card. The daughter card is then connected to a motherboard with four high speed connectors. The mother board has 40 SMA connectors around its edges, four of which are used for the power supplies and the remaining connectors used for supplying each pixel with the data signals as shown in Fig. 2.3.

2.1.4   Testing and Results

2.1.4.1   LED Performance

Prior to the LED array being integrated with the CMOS driver it was characterised including its electrical and optical characteristics. The LI and IV characteristics were measured simultaneously by placing a silicon photodetector in close proximity to the polished sapphire substrate of the LED array. All data points were obtained whilst in DC operation. The full modulation bandwidth was tested by combing a small signal modulation of fixed amplitude, generated by a HP8753ES network analyser, with a DC bias using a bias-tee. This signal was then sent to an individual pixel within the array using a high speed probe. The modulated emitted light was collected by a 1.4 GHz bandwidth photoreceiver and the network analyser to monitor the frequency response of the device.

Fig. 2.4 shows the LI and IV characteristics of a typical pixel within the LED
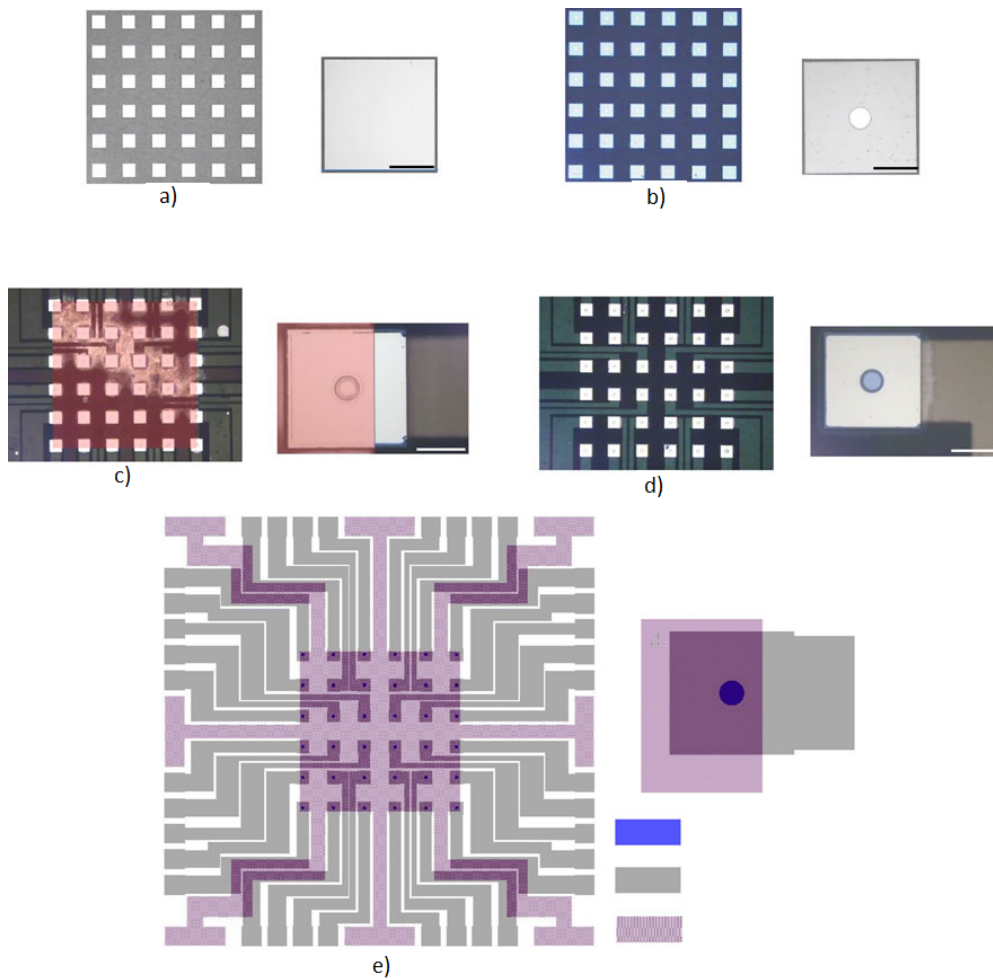
Figure 2.2: Plan view optical images of the main steps during the μLED array fabrication process, where the images on the right in each case show an individual pixel. a) Defining the GaN mesas by etching down to the sapphire substrate. b) The definition of each LED element with an etch stopping at the n-GaN. c) The deposition of metal bi-layers to allow for individual contacts. d) The deposition of metal for the shared p-electrode. e) A schematic of the entire LED arrays including contacts. The scale bar is 50 μm.
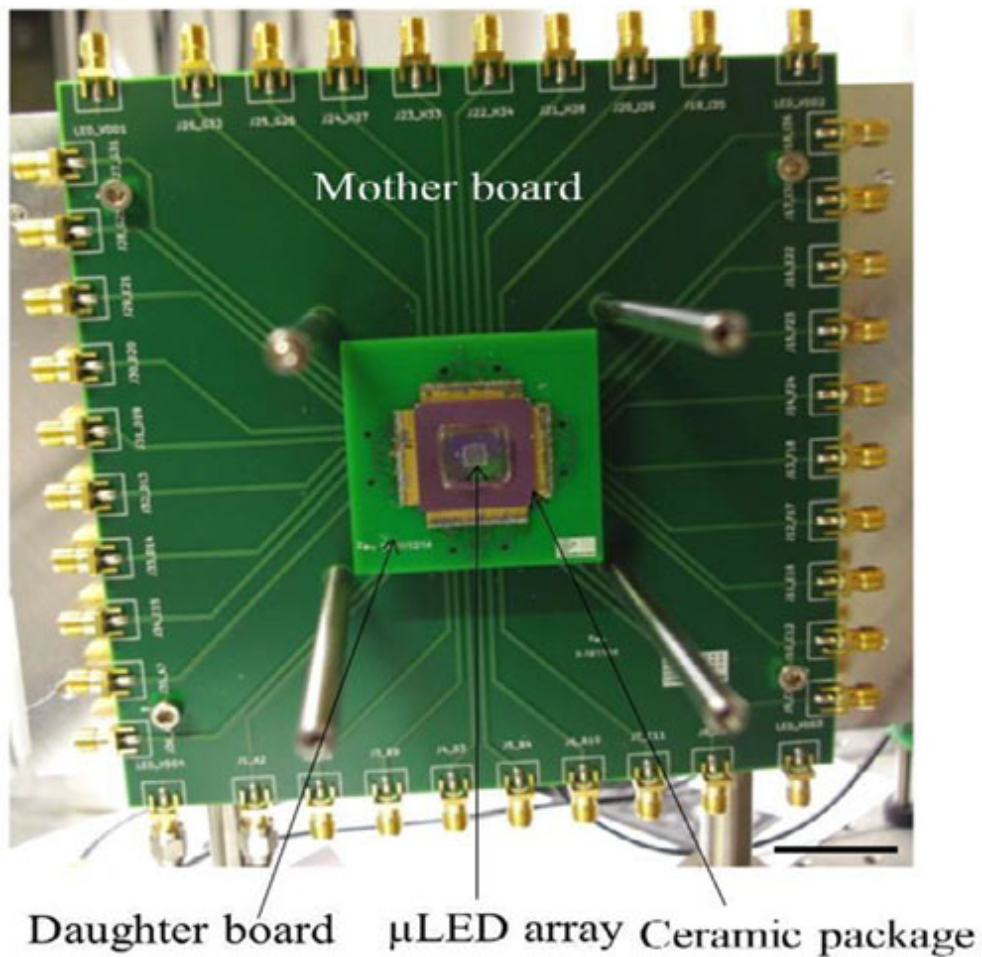
Figure 2.3: A photograph of the mother and daughter cards which integrate the LED array with the CMOS driver.

array. This demonstrates that an average pixel is capable of emitting over 2 mW before thermal rollover and can be driven up to 80 mA. This translates to an optical power density of 442.3 W/cm^2 and a current density of 17.7 kA/cm^2. This high current density, and therefore high carrier density and low carrier lifetime, leads to the high modulation bandwidths demonstrated by each pixel [2]. The effect can be seen in Fig 2.4b which shows a bandwidth of over 440 MHz, this being over twelve times higher then that of a typical commercially available LED [13]. Also, a significant improvement can be seen when this performance is compared to similar p-contact addressable μLED arrays which are only capable of $\approx$350 MHz [2,6]. This improvement can be partially attributed to the Pd contact to the p-type GaN which was not previously utilised. Previously an annealed NiAu contact, that was capped with a TiAu reflector, was used. This has a higher contact resistivity and a lower reflectance than Pd. Both of these factors reduce the functionality of the pixel as it increases the series resistance and reduces the light extraction efficiency, consequently resulting in a worse electrical to optical performance.

Another comparison between a typical μLED epitaxial structure and this n-contact design, is that the area of the metal contact to the n-type GaN of each pixel is limited to the area of the GaN mesa which has been etched down to the substrate. By observing the electrical characteristics, i.e. the reasonable turn-on voltage and slope efficiency which would degrade with a high contact resistance, it can be seen that the small contact area (less than 1.7 x10^{-4} cm^2) does not noticeably degrade the pixel's performance. This can be justified by the fact that the TiAu contact to the n-type GaN has a low contact resistivity ($\approx$3.7 x10^{-5} Ωcm^2) [14].

After this initial characterisation the array was integrated with the CMOS driver to show the functionality obtained in regards to its VLC applications. For these tests arbitrary waveforms were generated through a MATLAB^{TM} interface, downloaded into the FPGA and sent to the μLEDs via the NMOS based CMOS drivers. The PAM waveforms generated features of 0-255 levels on an 8-bit DAC, as defined by integer
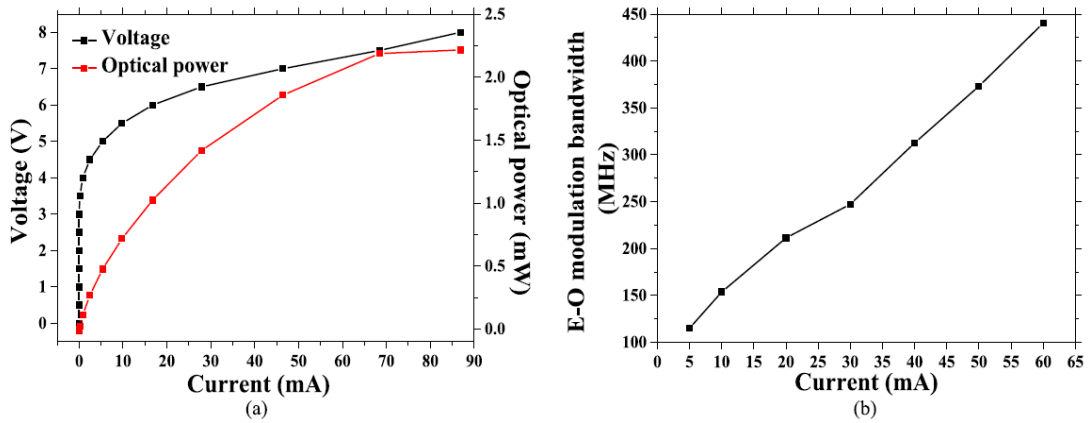
Figure 2.4: a) The LI and IV characteristics of a single pixel within the LED array. b) The E-O modulation characteristics of the same element [11].

values within the MATLAB^{TM} interface. The resultant output current from the CMOS drivers was directly proportional to the received integer value. The operating frequency of the LEDs is defined by modifying the clock speed of the CMOS drivers, which is also controllable through the MATLAB^{TM} interface. The output response was collected with a 1GHz APD (Hamamatsu C5658). The power supply to the μLED array was current limited to 70 mA per pixel with an upper limit of 9V during operation and all measurements were performed at room temperature.

Firstly a pseudo-random 2^8 OOK waveform was generated and sent to the μLED elements to test both their individual performance and the performance of four pixels. When testing multiple pixels, all were operated synchronously with the same waveform, though each was powered by a separate DAC. This data stream was transmitted at between 10-475 Mbps to test their bit error rates. The resultant waveforms and associated eye-diagrams for both individual and multiple pixels are shown in Fig. 2.5. Fig. 2.5a/b shows the performance of an individual μLED within the array at 300 MHz. This was able to be operated without observable bit error at up to 300 Mbps. Fig. 2.5c/d shows the performance of four adjacent pixels and shows a similar error free result though could only be driven up to 180 Mbps. The substantial drop in performance is attributed to additional heating effects as the pixels were in close proximity to each other. Also,
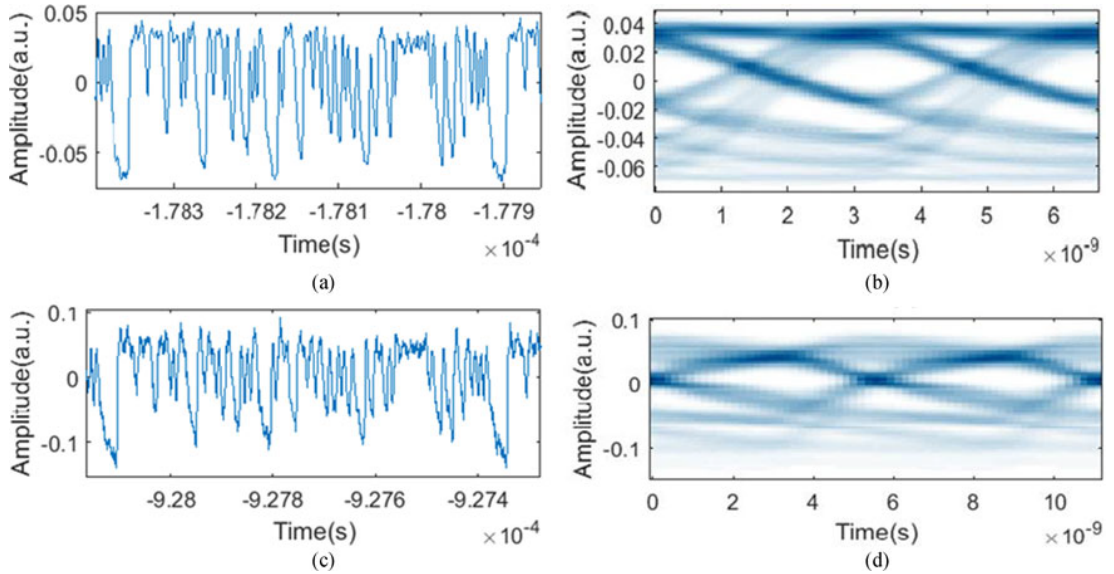
Figure 2.5: The received waveforms and their associated eye-diagrams for a,b) a single μLED element at 300 MHz and c,d) four elements at 180 MHz.

the device was operated with no heat sink attached so this may be circumvented to some degree in the future. It is important to note that the time jitter seen in both eye-diagrams is due to the reset times of the DACs after the OOK waveform is repeated and is not a result of the μLED performance.

Due to the control offered by the CMOS driver, the device is capable of producing more sophisticated data streams than simple OOK. For example, the modulation depth along with DC offsets can be altered. Moreover, the CMOS driver is capable of modulating each individual μLED independently and with distinct encoding schemes. To demonstrate this a single μLED element was modulated with a stepped sawtooth waveform, representative of PAM encoding, as shown in Fig 2.6. This waveform was generated with a 240 mA offset and a 16 mA modulation depth. The pixel was driven at 10 MHz with four distinct levels to demonstrate the CMOS capabilities in an error free environment. It is worth noting that as the LI characteristics of μLEDs are non-linear, the difference in emitted light intensities from the device become less pronounced as the driving current, based on the initial 0-255 value, increases. Therefore in order to achieve four evenly spaced optical power outputs, the initial integer data
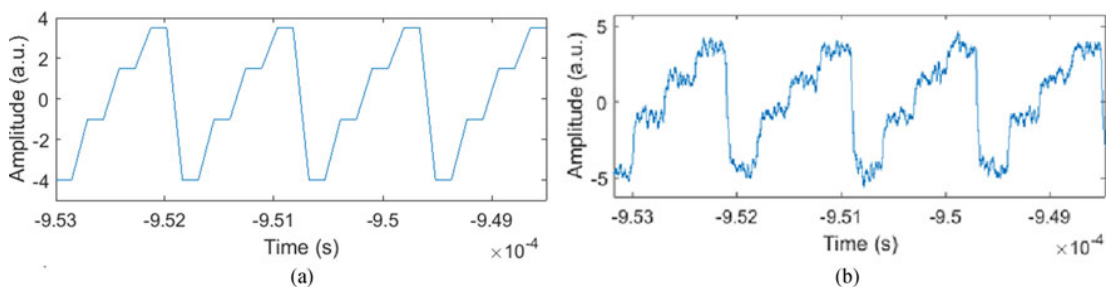
Figure 2.6: a) The 10 MHZ PAM-4 waveform sent from the CMOS driver used to drive the LED. b) The resultant optical output from the LED. Note that the time offset between the waveforms is due to the driving signal is the idealised depiction given through the MATLAB^{TM} interface and not the driving signal as seen at the LED.

stream must also be non-linear. The generated waveform sent to the device and the resultant transmitted data stream are shown in Fig. 2.6a/b respectively. It is key to note that although other previously reported μLEDs have been shown to have higher modulation bandwidths, they are still capable of being modulated at higher data rates than are possible with the CMOS drivers.

2.2 Photometric Stereo Imaging

The concept of photometric stereo imaging was introduced in Sec. 1.2.3. In this system a spatially separated array of light emitters can be used to sequentially illuminate an object from multiple angles as shown in Fig. 2.7. By doing so, a 3-dimensional image can be reconstructed from a single camera by combining multiple image frames with different shading characteristics [15]. An advantage of this technique is that no assumptions need to be made about the smoothness of any surfaces as is required by other techniques [16]. Although the imaging capability of photometric stereo systems has been studied in depth, by exploiting state-of-the-art LED technology the imaging function can readily be complemented by other capabilities, such as communications or positioning, by only modest modifications of the hardware. The concept behind how this would work is that the same array of emitters can be sequentially, or even simultaneously, used for other purposes. A good example of this is that LED arrays
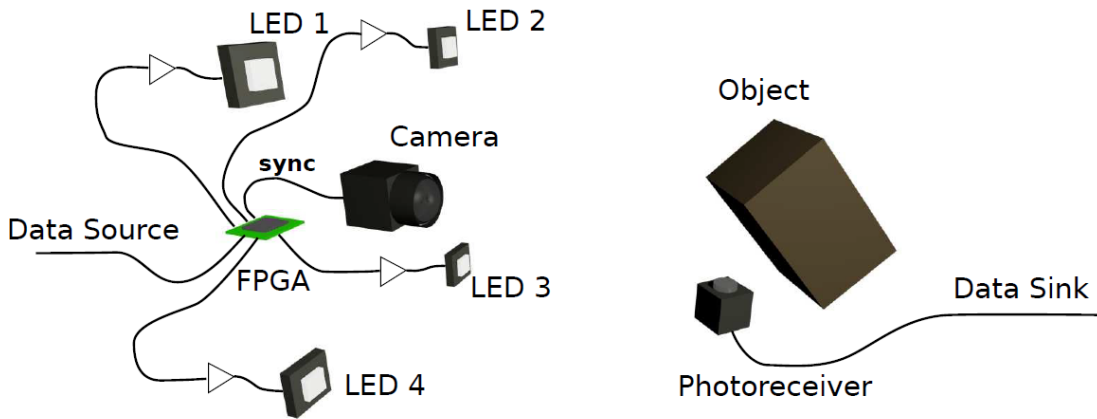
Figure 2.7: A schematic representation of the photometric stereo imaging setup [18].

have been used to implement structured illumination based functionality such as spatial tracking [17]. Furthermore, by using a suitable emitter, such as an LED, optical communication within the illuminated FOV is also possible. This creates the potential for systems which can have applications in manufacturing and robotics control. Thus, a motivation for my work was of the implementation of photometric stereo imaging systems with additional functionality based on μLED arrays.

2.2.1 Combination of Photometric Stereo-imaging with Optical Wireless Communications

The experimental setup, shown in Fig. 2.7, is designed to allow for both the 3D imaging of an object as well as data transmission within the FOV. In this configuration four LEDs surround a camera in an X-pattern. Here each of the LEDs are synchronised with the frame rate of the camera (60 fps) in order for them to sequentially illuminate with only one active element at any given frame. The object to be imaged by the setup is in this case a white cardboard box with a 1 MHz bandwidth photodiode alongside it. These are both placed at a distance of 0.5 m from the emitting LEDs.

Each LED was powered with an emitter-follower amplifier (BCX54) and is capable of emitting an optical power of 200 lm, and operating with an 8.6 MHz bandwidth.
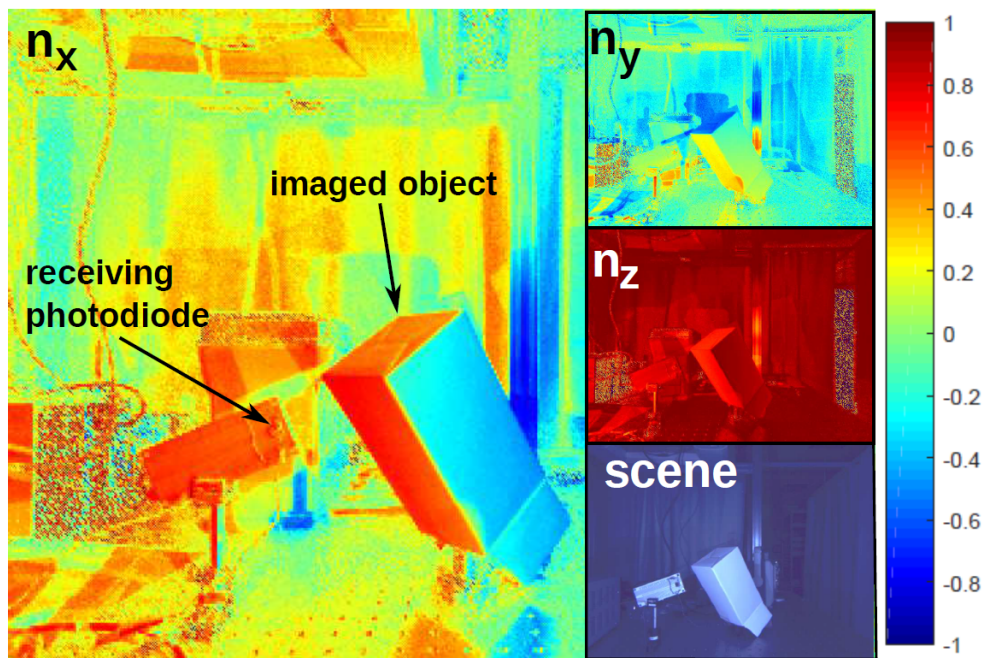
Figure 2.8: The individual vector components as determined by the setup along with a camera image of the scene [18].

An FPGA was used to drive the LEDs and superimpose the synchronisation signal with the data stream. The data stream itself was a pseudo-random 0.9 Mb/s OOK bit sequence of 2^{19} bits. This means that during the more general illumination used for the 3D imaging, the scene is simultaneously receiving this data stream. The LEDs were powered with an operational amplifier with a bandwidth of 1.6 MHz.

Fig. 2.8 shows how the component surface normal vectors, $\overrightarrow{n}$, of the box are generated. It shows the three coordinate axes being successfully identified and mapped i.e. the top of the box can be seen to be pointing left in the n_x image, all objects are pointing towards the camera in n_z, as would be expected. Note that the photodiode can be seen alongside the box. Not only is the box able to be successfully rendered but the integrated OOK signal was also present. The received data signal is shown in Fig. 2.9. This data demonstrates how over a longer millisecond timescale each individual LED contributes a different average optical power for each camera frame due to different alignments. This difference in average power is utilized by the photometric
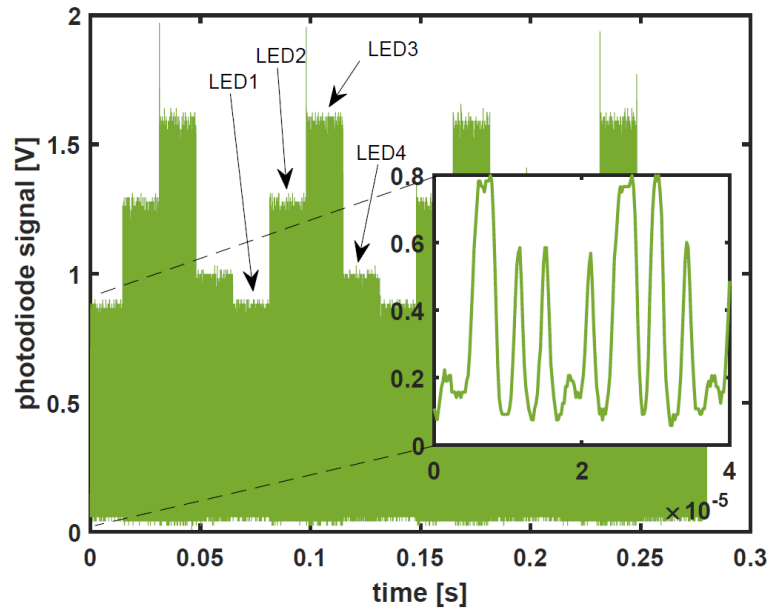
Figure 2.9: The received 0.9 Mb/s data stream. The four coarse intensity levels correspond to each of the LEDs within the array [18]. The inset shows the received signal over a shorter time period.

imaging element of this setup. However, within each average power level the OOK data stream can be detected by the receiver. Although what is shown here is a simple binary encoding scheme for the data transmission, other more sophisticated encoding schemes are possible.

The corresponding eye-diagram and bit error rate (BER) measurements results are shown in Fig. 2.10a/b respectively. Here Fig. 2.10a) shows four eye diagrams superimposed on top of each other. This is due to each LED having a different optical power intensity at the receiver. The '0' level is constant as each LED has the same 'off' state but the different LED positions each produce their own '1' level. Fig. 2.10b shows that the BER is below the detection limit up to 0.9 Mb/s and is limited by the speed of the op-amp voltage supply. This data rate can be increased through the use of different encoding schemes such as PAM or OFDM in addition to improving the frequency response of the driving circuitry [19].
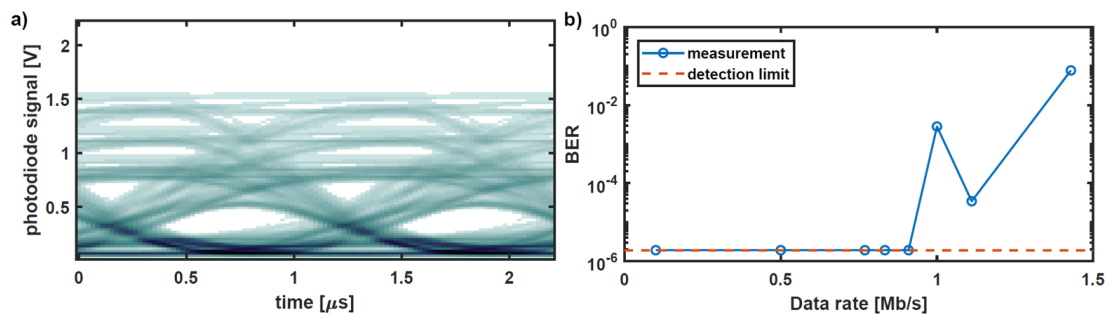
Figure 2.10: a) The eye diagram of the data stream. b) The BER at different data rates [18].

2.2.2 Orthogonal Frequency Carriers

Although the method above is powerful, as it only requires simple hardware to operate, it also requires the light sources to be synchronised with each other and the camera. There are several methods which can be employed to remove this requirement such as WDM or frequency division multiplexing (FDMA). WDM, although successfully implemented previously [20], has several significant problems, one of which is the limitations on available wavelengths. This is due to typical receivers sampling only the RGB contributions of light and hence only RGB light sources can be successfully identified. This in turn leads to another problem in that the differing colours operating at typical camera frame rates ($\approx$60 fps) can cause potentially uncomfortable non-uniform lighting in public space, if employed there. Secondly, coloured objects may cause issues in the imaging process. On the other hand, FDMA allows for all the light emitters to be white, thereby making it more suitable for public spaces. This technique works by modulating each emitter at different orthogonal frequencies, which can be resolved to produce a separate image for each emitter. It also has inherent advantages over the typical TDMA approach as the emitters' duty cycle is 50% instead of being inversely proportional to the number of emitters, therefore giving a more uniform general illumination of the FOV. In FDMA each emitter is modulated with a sinusoidal signal. Instead of the contributions from each emitter being resolved independently, like in TDMA or WDM, the individual power contributions can be recovered by taking a Fourier transform of
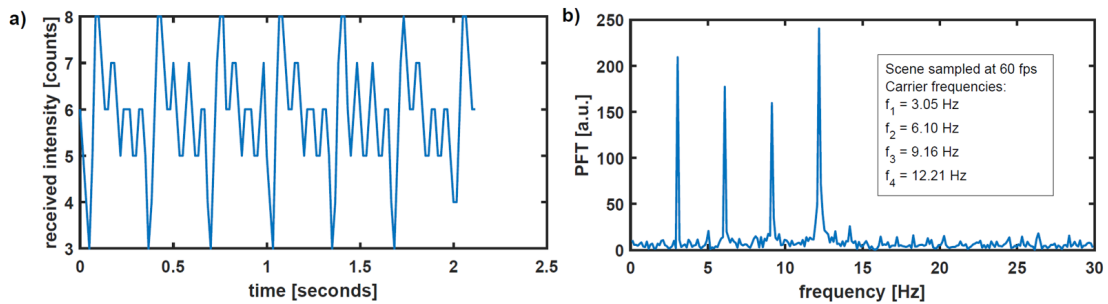
Figure 2.11: a) The received power intensities at a single pixel. b) The Fourier transform of the received signal [21].

the time sequence intensities for each camera pixel. This extraction process is shown in Fig. 2.11. Bu doing this each frequency creates a 'fingerprint' which can then be identified and extracted.

Here a photometric stereo imaging setup was developed which utilised FDMA for the above mentioned benefits. The light sources were four white LEDs (Osram OSTAR Stage LE RTDUW S2W). These were driven at 0.7 A and produced 200 lm at 8.6 MHz. This setup more accurately resembled a real world surveillance system as the FOV was illuminated from above whilst the camera viewed the scene perpendicularly to the emitters as shown in Figure, 2.12. This is typically how public indoor spaces are illuminated with ceiling based lighting, whereas typical photometric imaging setups place the camera and lighting in the same plane. The camera was operated at 60 fps. The LEDs were driven with a high fidelity sinusoidal wave by an FPGA with the respective emitters receiving a 3.05 Hz, 6.10 Hz, 9.16 Hz, and 12.21 Hz operating frequency as shown in Figures. 2.11 and 2.12. The object being imaged is in this case a 3-dimentional letter 'E'.

Figure 2.11a shows the received power intensities at the photodiode. It is clear that the signal periodically repeats every 0.33 s which relates to the lowest LED driving frequency. Figure. 2.11b shows the resultant Fourier transform of this data for a single pixel. Furthermore, it can also be seen that the four prominent peaks seen are at the driving frequencies and thus the power contributions for each LED can be determined
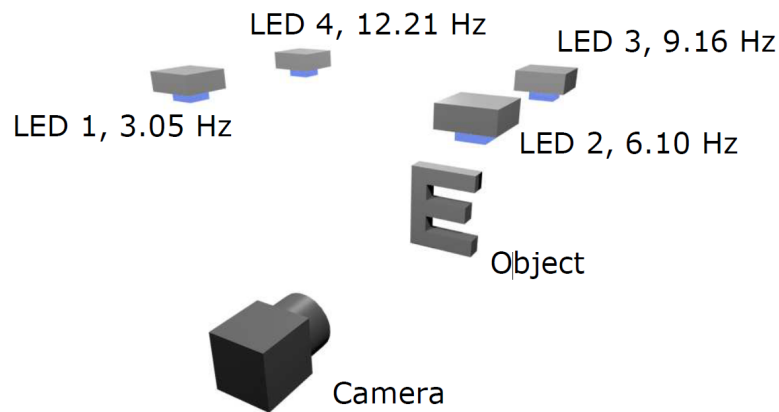
Figure 2.12: A schematic of the experimental setup [21].

from the peak amplitude. From this information a 3D render can be made in a similar fashion to a TDMA scheme. In this scheme the power from a single frequency can be represented with every pixel's recorded power at that same frequency, thus producing an image as if the scene had been illuminated by that LED alone. The insets of Figure. 2.13 show these images for each of the four driving frequencies. Figure. 2.13 also shows the reconstructed surface normal vectors generated from these component parts. The left and right oriented sides of the object can be clearly seen by the red and green shading respectively.

2.2.3   Combination of Photometric Stereo-imaging with Visible Light Positioning

In addition to providing a suitable light service for both 3D-imaging and data communications, the same LED array can be utilised for an object tracking function. In Sec. 1.4 a tracking technique using a μLED array and a fingerprinting approach was discussed. However, due to the reduced number of emitters in our photometric stereo setup, it will only offer a coarse target position. To improve upon this, triangulation offers a higher accuracy for the small number of emitters used whilst simultaneously requiring the same lighting geometry as used in photometirc stereo imaging. There are many different kinds of triangulation which can be defined into two categories; angulation
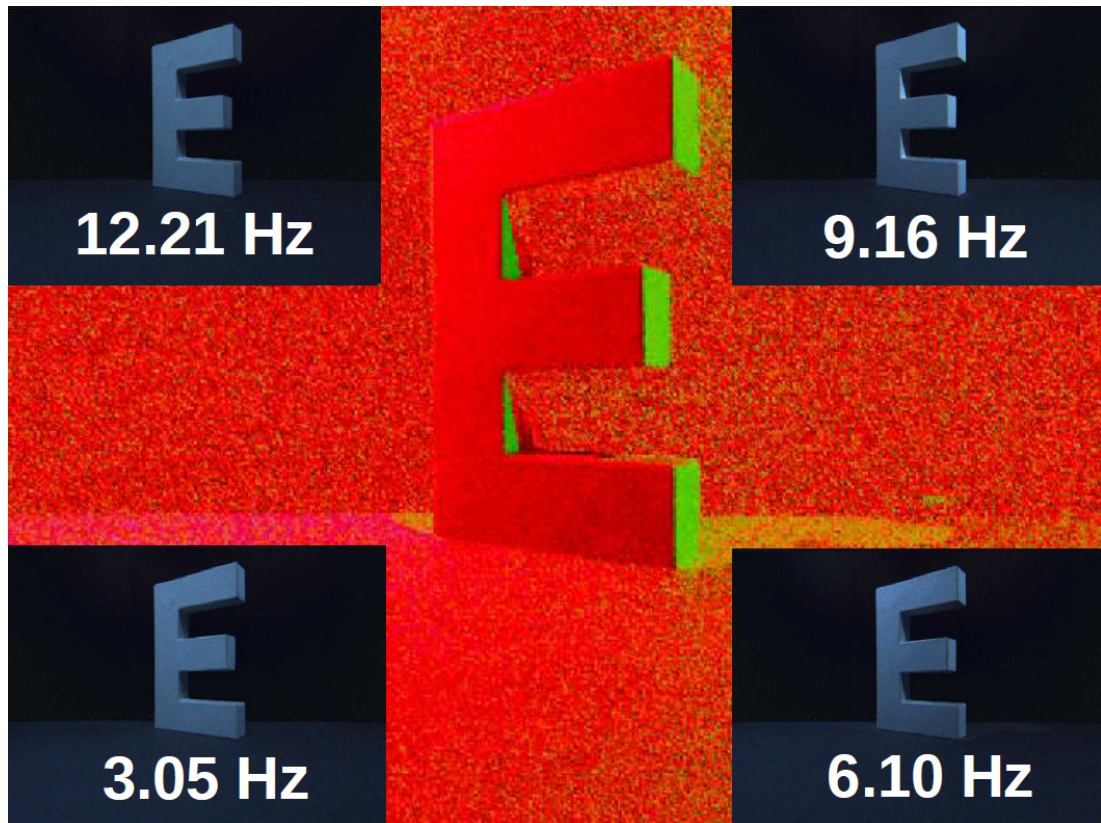
Figure 2.13: The reconstructed 3D image with the left and right orientations shown as red and green respectively. Insets: The different power contributions from the different LEDs modulated at different frequencies [21].
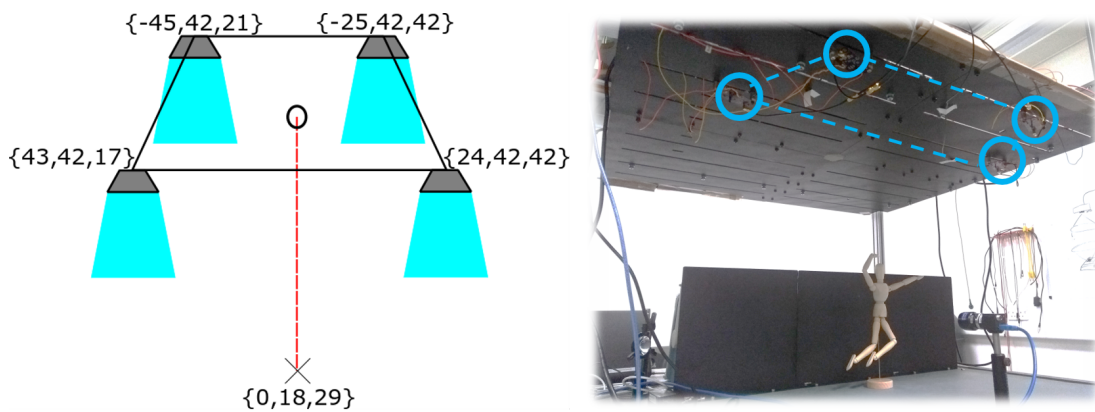
Figure 2.14: a) A schematic of the experimental setup used whilst testing the spatial tracking functionality including the coordinates of the emitters and receiver. b) An optical photograph of the same setup.

and lateration. Angulation maps the angle of arrival of the incident light from multiple emitters, whilst lateration determines a position using measured distances from multiple emitters. Typically the hardware requirements of angulation are higher due to needing receivers that can either physically pivot, and will also require an accelerometer or similar monitoring devices, or are capable of determining the angle directly, which are more expensive than typical photodiodes.

A lateration based tracking system was developed using the received signal strength ratios in a similar setup to that shown in Fig. 2.7 and 2.12. Here the emitters are arranged in a trapezium layout and the object within the FOV being a photodiode to read the optical power from each emitter. This is shown in Figure. 2.14a with the coordinates of the emitters and receiver (shown as a cross) shown.

In this system, instead of directly translating the received power from each individual emitter into a distance, due to the received optical power being inversely proportional to the distance from the emitter, we instead convert the power from multiple emitters into a distance ratio and determine the position from these ratios. This means that by comparing the relative strength of each LED when they are in known locations, it allows one to derive the location of the receiver. This has the added benefit of ignoring any errors caused by background light as this will typically cancel out across
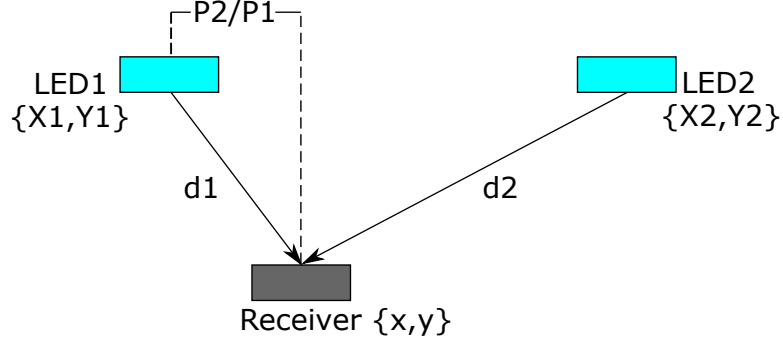
Figure 2.15: A simplified schematic demonstrating the power difference as a result of distance.

the LEDs. The LEDs themselves can be differentiated through either TDM or other methods such as FDM or WDM, which is compatible with the encoding schemes used in the 3D imaging element of this setup. The accuracy of the system can be increased through adding more LEDs to the array and by having the object within its confines, though it is not limited by this. A visual representation of the the power ratio derivation is shown in Fig. 2.15. After the power, and therefore distance ratios, have been found the specific coordinates of the receiver can be found. If (X_1,Y_1,h) and (X_2,Y_2,h) are the coordinates of the two LEDs whose power readings are being used for a ratio, Equation. 2.1 is true [22]:

$$\frac{\sqrt{(x - X_2)^2 + (y - Y_2)^2 + h^2}}{\sqrt{(x - X_1)^2 + (y - Y_1)^2 + h^2}} = \frac{d_2}{d_1}, \tag{2.1}$$

where x and y are the coordinates of the receiver and $d_{1,2}$ are the distances between the receiver and LED1,2 respectively.

This system is capable of not only determining the object's coordinates, but also its height, though to a lesser overall accuracy. Using the setup as shown in a grid of 90×25 a.u, positional errors between 0.05-1.3 were observed when LEDs are of known height, and between 0.5-11 when the LEDs are of unknown height. This data is given in table. 2.1. This setup was tested using both TDM and FDMA encoding schemes to differentiate between emitters, with both using and not using a known receiver height.

Table 2.1: A table giving the actual coordinates of the emitters and target along with the target's determined coordinates with different encoding schemes.

Object	Actual X-coordinate	Actual Y-coordinate	Actual Z-coordinate	
LED 1	-45	42	21	
LED 2	-25	42	42	
LED 3	43	42	17	
LED 4	24	42	42	
Receiver	0	-18	29	
Y-coordinate known	Modulation scheme	Determined x-position	Determined y-position	Determined z-position
Yes	TDM	0.05	-	28.7
Yes	FDMA	0.39	-	25.9
No	TDM	-0.5	-38	18
No	FDMA	-0.5	-27	13

2.3 Summary

This chapter has introduced how the structure and layout of a μLED array can be engineered to a specific application. The example discussed was the adaptation of a conventional p-contact based μLED array to a n-contact based one. Doing this allows for the driving electronics to be NMOS transistor based which brings several advantages. Each pixel of the resultant devices shows a bandwidth of 440 MHz with an optical power output of 2 mW. These devices were also integrated with a custom built NMOS based CMOS driver and were tested at 300 MHz with a single pixel and 180 MHz with four. Further demonstrated was their ability to emit at discrete, pre-determined output power levels in the form of a stepped wave function similar to that of 4-PAM encoding schemes.

This chapter went on to discuss the creation of an LED-based photometric stereo imaging system, which is capable of object tracking. First a TDM based system was introduced where the LEDs were synchronised. This was successfully able to distinguish different surface normals. However, in order to remove the need for synchronisation a FDMA approach was explored wherein each LED element was modulated at different frequencies and the resultant intensity recordings were decoded with a Fourier transform

to unpack the contributions from each LED. This setup was also used to implement a lateration based object tracking system due to its suitable layout. It was able to successfully track an object across two dimensions and, to a lesser extent, across three as required. This chapter has highlighted how some capabilities are enabled by state-of-the-art LED technology, in particular taking advantage of their direct electronic interfacing and modulation capability. In the following chapters it will be discussed how such functions can be incorporated in microfabrication.

Bibliography

[1] Z. Gong, S. Jin, Y. Chen, J. McKendry, D. Massoubre, I. M. Watson, E. Gu, and M. D. Dawson, "Size-dependent light output, spectral shift, and self-heating of 400 nm InGaN light-emitting diodes," *Journal of Applied Physics*, vol. 107, no. 1, p. 013103, 2010.

[2] J. J. McKendry, D. Massoubre, S. Zhang, B. R. Rae, R. P. Green, E. Gu, R. K. Henderson, A. Kelly, and M. D. Dawson, "Visible-light communications using a CMOS-controlled micro-light-emitting-diode array," *Journal of Lightwave Technology*, vol. 30, no. 1, pp. 61–67, 2011.

[3] D. Tsonev, H. Chun, S. Rajbhandari, J. J. McKendry, S. Videv, E. Gu, M. Haji, S. Watson, A. E. Kelly, G. Faulkner, *et al.*, "A 3-Gb/s Single-LED OFDM-Based Wireless VLC Link Using a Gallium Nitride μLED," *IEEE Photonics Technology Letters*, vol. 26, no. 7, pp. 637–640, 2014.

[4] H. Jiang, S. Jin, J. Li, J. Shakya, and J. Lin, "III-nitride blue microdisplays," *Applied Physics Letters*, vol. 78, no. 9, pp. 1303–1305, 2001.

[5] Z. Gong, H. Zhang, E. Gu, C. Griffin, M. D. Dawson, V. Poher, G. Kennedy, P. French, and M. Neil, "Matrix-addressable micropixellated InGaN light-emitting diodes with uniform emission and increased light output," *IEEE Transactions on Electron Devices*, vol. 54, no. 10, pp. 2650–2658, 2007.

Bibliography

[6] J. J. McKendry, B. R. Rae, Z. Gong, K. R. Muir, B. Guilhabert, D. Massoubre, E. Gu, D. Renshaw, M. D. Dawson, and R. K. Henderson, "Individually address-able AlInGaN micro-LED arrays with CMOS control and subnanosecond output pulses," *IEEE Photonics Technology Letters*, vol. 21, no. 12, pp. 811–813, 2009.

[7] J. Day, J. Li, D. Lie, C. Bradford, J. Lin, and H. Jiang, "III-Nitride full-scale high-resolution microdisplays," *Applied Physics Letters*, vol. 99, no. 3, p. 031116, 2011.

[8] E. F. Schubert, "Light-emitting diodes Cambridge University Press," *New York*, pp. 35–40, 2006.

[9] J. Herrnsdorf, J. J. McKendry, S. Zhang, E. Xie, R. Ferreira, D. Massoubre, A. M. Zuhdi, R. K. Henderson, I. Underwood, S. Watson, *et al.*, "Active-matrix GaN micro light-emitting diode display with unprecedented brightness," *IEEE Transactions on Electron Devices*, vol. 62, no. 6, pp. 1918–1925, 2015.

[10] S. M. Sze and K. K. Ng, *Physics of semiconductor devices.* John wiley & sons, 2006.

[11] E. Xie, M. Stonehouse, R. Ferreira, J. J. McKendry, J. Herrnsdorf, X. He, S. Ra-jbhandari, H. Chun, A. V. Jalajakumari, O. Almer, *et al.*, "Design, fabrication, and application of GaN-based micro-LED arrays with individual addressing by N-electrodes," *IEEE Photonics Journal*, vol. 9, no. 6, pp. 1–11, 2017.

[12] S. Rajbhandari, H. Chun, G. Faulkner, K. Cameron, A. V. Jalajakumari, R. Hen-derson, D. Tsonev, M. Ijaz, Z. Chen, H. Haas, *et al.*, "High-speed integrated visible light communication system: Device constraints and design considerations," *IEEE Journal on Selected Areas in Communications*, vol. 33, no. 9, pp. 1750–1757, 2015.

[13] J. Vučić, C. Kottke, S. Nerreter, K.-D. Langer, and J. W. Walewski, "513 Mbit/s visible light communications link based on DMT-modulation of a white LED," *Journal of Lightwave T-echnology*, vol. 28, no. 24, pp. 3512–3518, 2010.

Bibliography

[14] Y.-I. Nam and B.-T. Lee, "Investigation of Ti/Au and Ti2N/Ti/Au ohmic contacts to n-GaN films," *Semiconductor Science and Technology*, vol. 26, no. 8, p. 085014, 2011.

[15] T. Weise, B. Leibe, and L. Van Gool, "Fast 3d scanning with automatic motion compensation," in *2007 IEEE Conference on Computer Vision and Pattern Recognition*, pp. 1–8, IEEE, 2007.

[16] Y. Zhang, G. M. Gibson, R. Hay, R. W. Bowman, M. J. Padgett, and M. P. Edgar, "A fast 3D reconstruction system with a low-cost camera accessory," *Scientific reports*, vol. 5, no. 1, pp. 1–7, 2015.

[17] J. Herrnsdorf, M. J. Strain, E. Gu, R. K. Henderson, and M. D. Dawson, "Positioning and space-division multiple access enabled by structured illumination with light-emitting diodes," *Journal of Lightwave Technology*, vol. 35, no. 12, pp. 2339–2345, 2017.

[18] J. Herrnsdorf, J. McKendry, M. Stonehouse, L. Broadbent, G. C. Wright, M. D. Dawson, and M. J. Strain, "Lighting as a service that provides simultaneous 3D imaging and optical wireless connectivity," in *2018 IEEE Photonics Conference (IPC)*, pp. 1–2, IEEE, 2018.

[19] R. X. Ferreira, E. Xie, J. J. McKendry, S. Rajbhandari, H. Chun, G. Faulkner, S. Watson, A. E. Kelly, E. Gu, R. V. Penty, *et al.*, "High bandwidth GaN-based micro-LEDs for multi-Gb/s visible light communications," *IEEE Photonics Technology Letters*, vol. 28, no. 19, pp. 2023–2026, 2016.

[20] C. Hernández, G. Vogiatzis, G. J. Brostow, B. Stenger, and R. Cipolla, "Non-rigid photometric stereo with colored lights," in *2007 IEEE 11th International Conference on Computer Vision*, pp. 1–8, IEEE, 2007.

[21] J. Herrnsdorf, J. McKendry, M. Stonehouse, L. Broadbent, G. C. Wright, M. D. Dawson, and M. J. Strain, "LED-based photometric stereo-imaging employing

frequency-division multiple access," in *2018 IEEE Photonics Conference (IPC)*, pp. 1–2, IEEE, 2018.

[22] T.-H. Do and M. Yoo, "An in-depth survey of visible light communication based positioning systems," *Sensors*, vol. 16, no. 5, p. 678, 2016.

Chapter 3

Maskless Photolithography using μLEDs

This chapter will showcase the development of a maskless photolithography system capable of micrometre scale resolution direct writing and operating in the near UV spectrum. The optical sources used are CMOS integrated μLED arrays. The chapter will go on to describe the characterisation of the set up and present performance analysis.

The drive for maskless photolithography setups stems from the fact that the custom quartz masks typically used in optical lithography are expensive and time consuming to fabricate. Additional issues arise from these masks offering little to no flexibility with additional masks needed for each pattern which can become cumbersome when prototyping new designs or updating old ones. Also, if a large number of designs are being fabricated and updated continually, hard masks require physical storage which can take up unnecessary space. It has been shown in the past by our group that micro-LED arrays are well suited for maskless photolithography due to the innate spatio-temporal control they provide, along with the suitable emission spectra to expose typical photoresists. Additionally, the small size of the pixels means that by modest demagnification a good feature resolution down to 1μm can be achieved. Micro-LEDs

offer further advantages over laser sources as they are comparatively cheap, have a low power consumption and can interface easily with commonly available electronics, giving benefits to any photolithography system which incorporates them. With the need for photolithography in industry, maskless photolithography can provide quicker and cheaper device fabrication with minimal down time between fabricating runs due to not requiring the change of physical masks.

3.1   Motivations and Current Tools

The aim of this work is to produce a 'smart' maskless photolithography tool which is capable of functioning at micro-scale resolution, whilst also having the potential to incorporate other LED array based functionality. As explained in Sec. 1.2.2.1, photolithography typically uses a specially created quartz mask with the negative of the pattern imprinted upon it to achieve a desired exposure pattern. The problem with this mask based approach is that each pattern requires its own unique mask. These masks are both time consuming and expensive to fabricate, especially during prototyping or when only limited numbers of uses are required. This expense has spurred the development of alternative maskless techniques [1,2]. In these systems the mask is essentially replaced with an optical source, typically operating in the UV, with a beam profile which can be projected and focused on the microscale for local photocuring. A pattern can then be created with this narrow beam by either scanning across the sample surface or by moving the sample stage accordingly. This is usually achieved through direct laser writing [3], which typically uses diode lasers or optically pumped solid state lasers as the UV source [4]. In such cases, the sources have a relatively high power consumption and can be physically large which results in the equipment used in these methods being expensive to buy and operate. A low footprint alternative are LEDs emitting in the UV range which have been shown to be suitable emitters [5,6]. The use of LEDs as a light emitter means that a relatively cheap, compact and low

power consumption system can be created which produces competitive lithography results along with the ability to exploit the spatio-temporal control offered by CMOS integrated μLED arrays.

Further benefits of using LEDs over lasers in photolithography come from the LEDs having a diverse range of emitting wavelengths across the entire spectral range from deep UV (260 nm) to infrared (1550 nm). This diversity in available wavelengths introduces the potential for photocuring photosensitve materials both within and outside the typical i/h/g line values, i.e. 365, 405 and 435 nm. Not only are these non-standard wavelengths widely available, but unlike laser based emitters, a library of different wavelength devices can be relatively cheaply obtained and the interchanging of LED devices is a quick and easy process. Using an array of emitters for photo-curing also enables the potential for multi-pixel exposure meaning that instead of scanning the sample with a single optical spot, the array is capable of exposing multiple areas simultaneously for either creating a structure more efficiently or the simultaneous fabrication of a repeated structure across the substrate.

3.1.1   Current LED Based Photolithography Equipment

LED based photolithography equipment is an established technology which is quickly rivalling laser based systems. Unlike laser based systems, LED emitter have the added benefit of being able to be fabricated into arrays on controllable size, pitch and shape to give an innate spatial encoding to the emission patterns. This allows for multiple pixels to the be exposed simultaneously in addition to producing continuous photocured structures by activating adjacent pixels within the array. Along with this, the shape and pitch of the pixels defines the shape of their exposure profiles allowing for customised exposure patterns within the array. For example by having multiple pixels with different shapes and sizes capable of giving the user quick and easy access to pattern designs which purely circular spot profiles may be unable to achieve.

The work presented in this chapter is a progression of a previously reported μLED
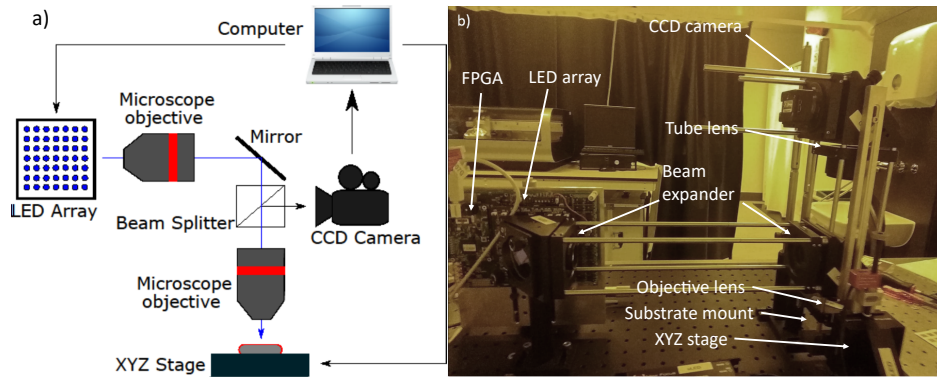
Figure 3.1: a)A schematic of a LED array based maskless photolithography system [7] and b) a optical photograph of the setup.

based maskless photolithography setup [7]. This setup also offers comparable or higher resolution than commercially available maskless photolithography equipment [8–10]. This system used a CMOS integrated 8×8 μLED array emitting at 370 nm. The pixels were circular with a 72 μm diameter and a 200 μm centre-to-centre pitch. The control of the emission patterns was achieved through custom software capable of defining patterns through a graphical interface and operating the LED array accordingly in either DC or pulsed modes. Pulsed operation was accurate down to 100 ms. This system, although functional, has several limitations in that multiple output patterns cannot be utilised without stopping to redefine a new pattern. This also extends to having no internal memory to store and then reuse old patterns. Another issue is that the setup relies on manual translation stages which reduces the potential for any automation or larger continuous structures being photocured. The optical setup uses microscope objectives to collect, collimate and refocus the light onto the sample. A beam splitter is placed between the lenses so that a CCD camera can observe the sample. This is shown in Fig. 3.1. The collecting objective lens is capable of viewing a 4×4 pixel area of the LED array.

By altering the exposure dose, this setup was capable of producing features size ranging between $\approx$8-24 μm in diameter, though with the potential to improve this to a size of $\approx$1 μm [7].

3.2 System Development

In order to improve on the system design described in Sec. 3.1.1, several initial target parameters were set. These were to produce a system with the following characteristics:

- LED based maskless photolithography

- Competitive photocured feature sizes

- Synchronised LED and motorised XYZ translation stage control

- All software achieved in a single MATLAB interface

- Capable of incorporating structured illumination through additional LED arrays

- Inexpensive, commercially available optical components

By developing a system with the above features, a 'smart' photolithography tool can be created capable of an unprecedented level of flexibility and control over automated photolithography based fabrication.

3.2.1 System Design and Components

3.2.1.1 Optical Setup

A schematic of this setup is shown in Fig. 3.2. In this setup the projected patterns from two μLED arrays (LED1,2), with wavelengths of 370 and 450 nm, respectively, are collected and collimated by aspheric lenses (f3,4), with a focal length of 10 mm, before being added to the main optical path with dichroic mirrors (D1,2). The light then passes through a beam expander made from two spherical lenses (f1,2 with a focal length of 250 mm and 50 mm, respectively) to properly demagnify the pattern to suit the required FOV before reflecting off a beam splitter (BS) and focused through a vertical infinity-corrected objective lens (10X) onto the sample. The sample itself is mounted onto a right-angle bracket attached to a motorised XYZ stage to allow automated movement

85
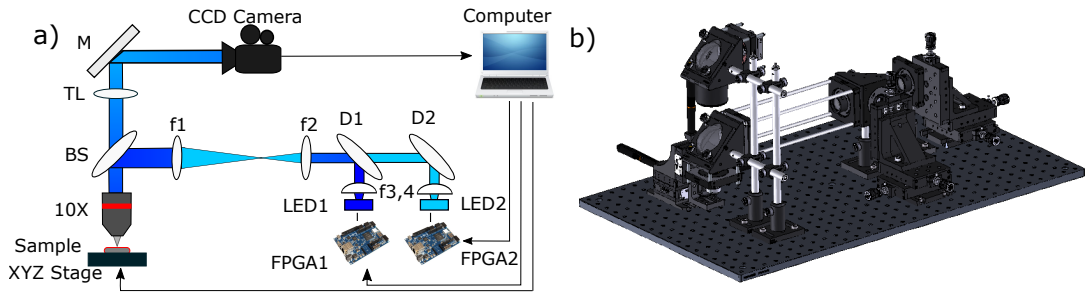
Figure 3.2: a) A schematic of the photolithography system. This also includes the second array which can be used for additional functionality and is not used in the photolithography process. b) A 3D render of the setup.

in coordination with the projected light to create larger, continuous direct writing structures. The sample is observed with a CCD camera mounted above the beam splitter using an infinity-corrected tube lens (TL) to control its FOV. Note that a mirror was used to alter the beam path to make the system more user friendly. The software is capable of simultaneously reading the input from the CCD camera, modulating the LED arrays through controlling the FPGAs (FPGA1,2) and controlling the motorised XYZ stage. For purely photolithography, the second LED array, FPGA, aspheric lens and dichroic mirror are not required. These additional parts are included for the future incorporation of structured illumination to produce the 'smart' aspects of this setup which will be described in Chapter 4.

The motorised stage is capable of a 0.5 μm step resolution at a maximum translation speed of 1 mm/s, though due to the driving electronics only one axis may be changed at any given time. With a spot size of $\approx$20 μm in diameter at the sample, the combination of a 16 $\times$ 16 LED array and the stage's 25 mm $\times$ 25 mm movement range, this allows for up to 20,700 separate exposure patterns without changing or remounting the substrate.

A simple beam expander was included to effectively change the size of the projected patterns. It is important to note that for purely photolithography implementations the spot size should be at a minimum in order to increase the system's resolution. However, in order to implement any form of practical structured illumination (described later) a reasonable FOV is required for the projected patterns. This effectively creates a trade-

off between having a small enough spot size to maintain a reasonable photocured feature resolution and power density, and the requirement of a low enough demagnification to give an effective coverage to allow for this structured illumination. Along with this trade off, the maximum FOV which can be achieved is limited by the FOV of the camera, and the minimum size is limited by either the diffraction limit of the wavelength of light used for curing, or the resolution of the camera.

Here an aspheric lens is used to collect and collimate the emitted light from the μLED arrays. When compared to the initial setup detailed in Sec. 3.1.1 which used a microscope objective, an aspheric lens was instead used in order to capture light from a significantly larger area of the LED array. With the microscope objective only a 4×4 pixel area of the array was captured and with the aspheric lens the entire 16×16 pixel array could be seen. Yet this brings with it the disadvantage that the collimation of the light is inferior and hence more optical power is lost through divergence. These divergence losses are detailed in Sec. 3.2.2. In order to minimise these losses, 2-inch optics were used in the setup to maximise the light collection throughout. Although the light collimation with aspheric lenses is non-perfect, it is adequate enough so that there is no observed spot overlap at the sample for LED arrays with a high pixel fill factor ($\approx 98\%$).

The optical setup was built with the following components:

- Manual XYZ translation stages to mount the LED and driving electronics onto (Thorlabs PT3/M - 25 mm)

- A motorised XYZ translation stage (Newport 9064-XYZ-PPP), and appropriate driver (Newport 8742-4)), to mount the sample onto

- FPGA driver (XEM3010-1000 from Opal Kelly)

- The μLED array used for photocuring

- 490 nm wavelength transmission cutoff dichroic mirror (D2 - Thorlabs DMLP490L)

- 425 nm wavelength transmission cutoff dichroic mirror (D1 - Thorlabs DMLP425L)

- A 50/50 beam splitter (BS - Thorlabs BSW16)

- Three 90° lens mounts (Thorlabs KCB2/M)

- Two spherical lenses (f2 - Thorlabs LA1131-A) and (f1 - Thorlabs LA1461-A)

- A 10× microscope objective (10X - Thorlabs RMS10X)

- A mirror (M - Thorlabs PF20-03-P01 - Ø2")

- Two aspheric lenses (f3,4 - Thorlabs AL1210M-A - Ø12.5 mm S-LAH64)

- A tube lens (TL - Thorlabs TTL200-A)

- A CCD camera (FLIR CM3-U3-13Y3C)

- Mounts, mechanical parts, and a laptop for control

3.2.1.2 LED Devices

As described in Sec. 1.3, CMOS integrated micro-LED arrays can be used to produce emitters capable of high frame rate and high fidelity pattern projection. Here a 16×16 micro-LED array was used as the UV source for photocuring. This array consists of 256 individually addressable circular pixels. This array was developed in-house at the Institute of Photonics and was integrated with a custom built CMOS driver (developed at the University of Edinburgh). The LED fabrication details and functions of the CMOS driver are described in Sec 1.3. This array can be driven by an FPGA and a subsection of it is shown in Fig. 3.3. The pixels are of 72 μm diameter with a 100 μm centre-to-centre pitch.

The CMOS driver is capable of supplying each pixel with a maximum of 5 V and 100 mA of current. As the LED ground connection is independent of the 'global ground', it is possible to negatively bias this terminal to artificially increase the effective voltage
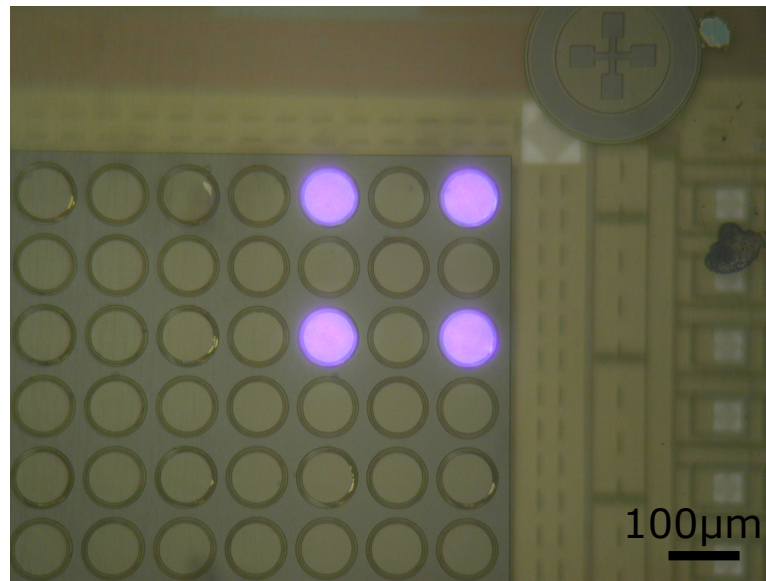
Figure 3.3: A plan view optical micrograph image of a FPGA compatible μLED array sub-section. Here, four pixels are shown turned on.

across the array. Although this is not required for the array used here, it is useful to note for LEDs which may require a higher turn on voltage (for example devices in series, different wavelengths or large bandgap larger devices). The IV and LI characteristics of devices comparable to those used in this setup are shown in Fig. 3.4. This figure demonstrates how the the CMOS driver's supply capabilities are able to meet the required voltage and current conditions per pixel before efficiency droop dominates the LED optical power output. On top of the suitable electrical characteristics, the optical modulation bandwidth of the pixels are high enough that the overall performance is limited to the driving modulation rate supplied by the CMOS electronics [11]. Here the unbonded LED elements are capable of a modulation bandwidth of 400 MHz for a single pixel, whilst the maximum rate achieved after bonding to its driver is 110 MHz for OOK signals. This, however, is further limited due to the serial data link only allowing a full array pattern refresh rate of 2 kfps [12], though this only applies when changing the pattern itself and not the modulation of any pre-loaded pattern.

Due to these devices being designed for communication of OOK signals [11] the
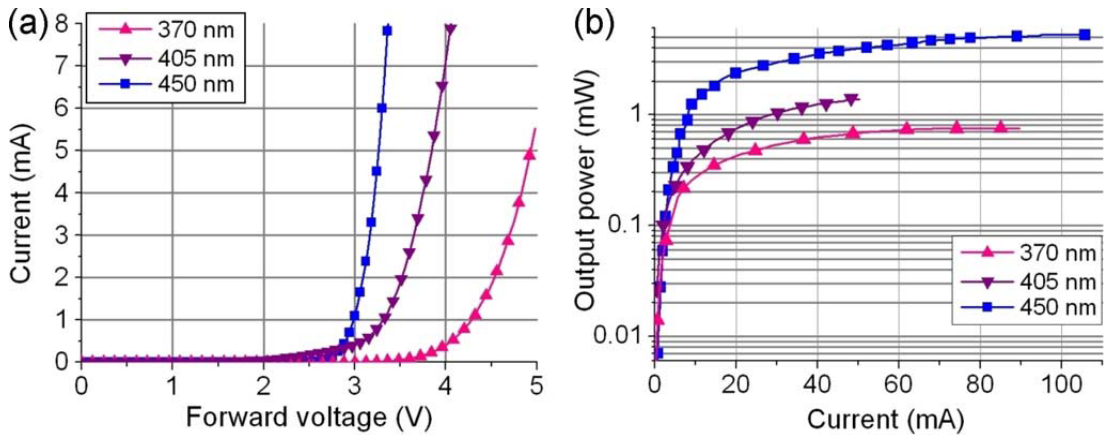
Figure 3.4: The a) IV and b) LI characteristics of comparable devices to those used in the photolithography system, fabricated in a similar methodology [11].

LED elements are unable to produce variable light intensity (greyscale) outputs with the driving software. This is problematic for photolithography systems as having a controllable exposure power output enables the production of different line thickness in the photocured structures. Note this is only an issue in this setup for continuous structures which requires the translation stages to be in motion, as static exposure doses can be controlled by modifying the exposure time. This is explained in Sec. 3.2.2.

3.2.1.3 Software Development

The software for this work was developed within MATLAB^{TM}. Patterns can be defined and added to a library for use, where each pattern defines whether each pixel is ON or OFF. These patterns can be created by either individually defining the state of every pixel within the array, or by generating a i $\times$ j matrix where i and j represents the size of the array. This matrix requires either a '0' for an OFF state or a '1' for ON. This library of patterns can be uploaded to the FPGA at a rate of 2 kfps and up to 512 patterns can be stored on the FPGA. As mentioned previously, the FPGA is unable to drive the LED arrays outside of OOK streams. To accommodate this, instead of modifying the output power of the devices, it is possible to control the exposure dosage though PWM and reducing the duty cycle of the LEDs. It is worth noting that the

power output of the LED's will decrease as they approach the 110 MHz bandwidth as explained in Section. 1.1.5.2. This PWM encoding is generated using a 100MHz clock and its upper limit is governed by the the time taken to load in a new pattern (250 μs). This can be used to effectively decrease the exposure times beyond the limitations of the data link. By controlling both the exposure time and the movement speed of the stage, the exposure dose at the sample can be either fine tuned giving control over the feature sizes created, or more coarsely tuned for different photosensitive materials. This can be used in tandem with controlling the rate at which patterns are projected, along with the stage movement to give good control over the sample exposure. Note that the motorised stage is synchronised with the LED array meaning that patterns or stage movements can be triggered or ended simultaneously.

3.2.2   Initial Characterisation

Between the LED array characteristics and the optical components used, the setup is capable of controlling many aspects of the projected optical spot profile and sample exposure. Whilst the exposure dosage is a product of both the LED power performance and software control, the shape of the optical spot seen at the sample also closely matches the shape of the emitting area of the μLED which is illuminating it. For example a circular pixel used in this work, with a 72μm diameter, creates a circular illumination spot on the sample. The spot size was set to be $\approx$20 μm using the beam expander, meaning that a full pattern is within the limits of the CCD camera's FOV and still produces a cured feature size which is competitive with other optical photolithography systems. The FOV of the camera was determined to be 370 $\times$ 460 μm^2 and the projection FOV was seen to be 320 $\times$ 320 μm^2. This spot size was measured by projecting it onto a sample with known feature sizes and pixel counting the resultant images using a power threshold of the spot's spatial FWHM. Another aspect which effects the spot profile is the imaged spot intensity profile of the LEDs themselves. Each pixel within the array inherently produces a 'top hat' shape profile which usefully
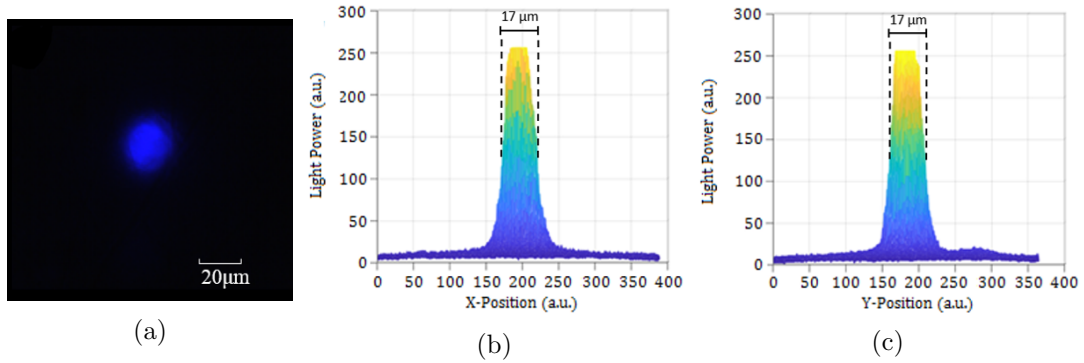
Figure 3.5: a) Optical image of a single projected spot. b) The x-axis intensity profile of the same spot. c) the y-axis intensity profile of the spot.

provides a FWHM that is similar to total spot size. Here the FWHM was measured to be 17 μm for a 20 μm target spot size as shown in Fig. 3.5. This also shows that the power distribution across the spot is uniform across multiple axes which is required for reliably producing repeated features. Fig. 3.5b) and 3.5c) were was produced by extracting the intensity values from Fig. 3.5a) in both the X and Y directions, crossing through the centre of the spot each time. Another factor which can impact LED emissions is non-uniformity's and defect in the actual μLED's themselves. During the fabrication process defects can be developed which can reduce the electrical and optical characteristics resulting in a lower power output. For example, if problems arise during an etching process then pixels can be shorted together whilst issues during the bump bonding process can mechanically damage the pixels causing them to fail. Along with this, LEDs will naturally degrade during operation, typically through heating effects, which will eventually result in device failure.

Other effects which were observed stem from the physical components of the setup. Firstly, due to the non-coherent nature of the light source and non-perfect collimation of light from the aspheric lenses, chromatic aberration could occasionally be seen at the sample. This can typically only be seen when the setup is poorly aligned, specifically in terms of the dichroic mirrors as is the case shown in Fig. 3.6. Chromatic aberration presents a problem for photolithography as the light is spread over a larger area resulting

in a lower resolution. It also produces a non-uniform spot, which in turn produces non-uniform features. This is made worse by the different wavelengths being aberrated by different amounts, meaning that the wavelength at the photoresist's peak sensitivity may have shifted position causing miss-alignment. This issue was rectified by the implementation of a single 60 mm mechanical cage system for all optical components to ensure correct alignment. Another issue, stemming from the equipment, is that the edge of the sapphire die in the LED array produces reflections from the outer two rows of pixels. This can be simply avoided by only using the inner 12 $\times$ 12 array of pixels although the detrimental effects of these reflections are explained further in Chapter. 4. It should also be noted that the dark region which can sometimes be seen in the centre of the imaged spot is the result of local damage to the p-contact caused during the bump bonding process. This feature does not typically cause any issues during the photocuring process as it results in a well defined feature edge when compared to a Gaussian profile, although the ideal case is the flat top profile shown in Fig. 3.5b,c. Note that this dark spot is not always present and is an issue with pixel uniformity during the fabrication process.

The average optical power was measured using a calibrated power meter on the sample stage at an equivalent height to give proper focus. Each LED was driven independently in DC mode and the average power of a single pixel at focus was 15.3 μW at a driving current density of 1950 A/cm^2. This results in a average power density of 4.87 W/cm^2 across the 20 $\times$ 20 μm^2 spot and a power density of 6.74 W/cm^2 at the half maximum intensity position.

Due to the modulation bandwidth of the LEDs grossly exceeding the full frame modulation capacity of the FPGA driver, the rise/fall times of any signal were considered to be minimal and the exposure dosage was assumed to scale linearly with exposure time/duty cycle. When the sample is static the exposure dose is determined simply by multiplying the intensity with the exposure time. Assuming an ideal flat top emission profile, the exposure dose whilst the sample is moving is given by:
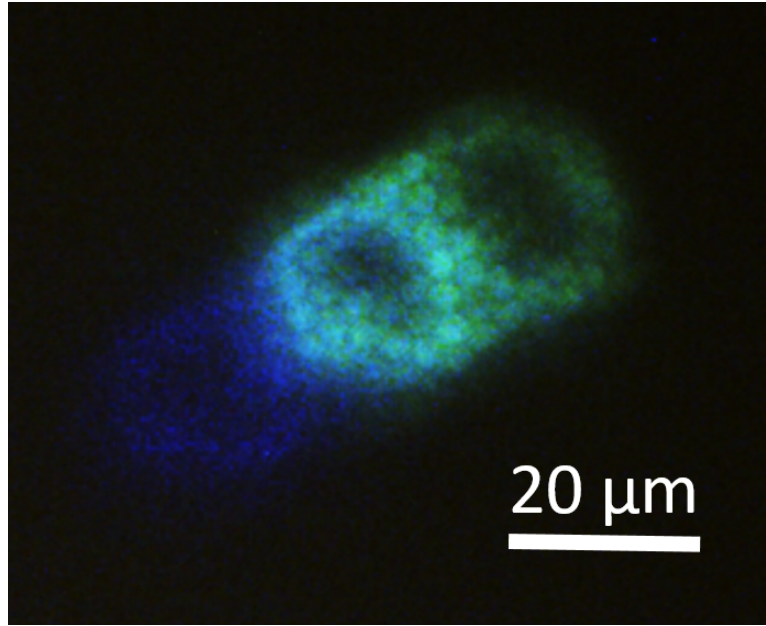
Figure 3.6: An optical image of the chromatic aberration shown at the sample plane from a single pixel. Note that the decrease in brightness in the centre of some of the pixels is an artifact from the bump bonding process. Substructure of the patterned sapphire substrate substrate is also evident in this image.

$$E = \frac{2P}{\pi R^2 v}\sqrt{R^2 - y^2}, \tag{3.1}$$

where P is the total spot power, R is the pixel radius, v is the stage velocity and y is the coordinate perpendicular to the velocity.

Whilst the transmission losses throughout the system are low, there are some losses particularly in the initial light capture with the aspheric lens and in the beam expander. These divergence losses can be calculated using:

$$\text{Divergence Angle} = 2arcsin(\frac{\eta_{air}}{\eta_{air}}\frac{l}{2d}), \tag{3.2}$$

where the refractive indices are assumed to be air on each side of each lens, l is the diameter of the emitter and d is the distance between lenses. For example, between the spherical lenses in the beam expander where we see a divergence of $8°$ this escalates to

an optical power loss of $\approx$89%. These losses can be minimised by simply using larger optics though with a 60 mm cage system, however further increasing the lens diameters is impractical. Another substantial loss comes from the 50/50 beam splitter which is used to allow the camera to monitor the sample. This simply incurs a 50% power loss after the beam expander. Note that this is not an issue for imaging as the camera is sensitive enough to fully saturate despite this loss occurring twice before detection. To address this, a 90/10 beamsplitter could be used to project more light onto the sample. Another potential solution is to use another dichroic mirror if the camera is not required for that specific application.

In order to produce larger continuous structures the motorised XYZ stage can be used to scan the spot across the sample. To ensure this reliably produces features of uniform size and width, the step size and speed of the stage must be consistent and known.

The XYZ stage used throughout this work has several potential issues which negatively effect the reliability of photocuring. For example, although the pico-motors have a step size of 30 nm, the stage itself has a resolution of 500 nm and a roll out of 2.5 μm [13]. This led to significant translation errors when moving larger distances (<1000 steps). The ability to correct these errors is a motivation for employing structured illumination as will be discussed in Chapter 4. Other issues come from the fact that the step size and translation speed vary depending on the weight of the sample. Also the step size has been seen to vary depending on the stage velocity. This error will typically be uniform if similar substrates are used for patterning. However, the step size also varies depending on the translation speed defined in the software control. This means that if the exposure dose is increased by slowing down the stage, the distance travelled will also increase or decrease giving different-sized features.

3.3   Photo-Sensitive Materials

Throughout this work a commercially available, photosensitive resin was used as the photocuring material (ANYCUBIC). This is due to both the ready availability of the material and its desirable properties for both curing and the resultant polymer. This material acts as a negative photoresist which has a peak sensitivity to 370 nm light and can be spin coated to 5-15 μm thickness, this was measured using a stylus profilometer (DekTak) for multiple spin speeds and times. The samples in this test were made by spin coating, the material across a glass substrate partially covered with electrical tape. After the spin coating the sample was fully cured and the tape subsequently removed giving a clear step which can be measured. Fig. 3.7 shows the results from a sample produced with a spin speed of 3200 rpm for 20 seconds. This $\approx$9 μm film thickness gives a good lateral feature resolution.

The resin also shows a good adhesion to borosilicate glass which allows for microscope slides to be used as a substrate. The process for cleaning and producing photocured samples is given below:

- A borosilicate glass slide is cleaned for two minutes in an ultrasonicated acetone bath. This process is repeated for methanol, IPA and DI water.

- The substrate is then baked at 120°C for 15 minutes to thoroughly dry it.

- The substrate is placed in the spin coater and the resin is carefully dropped onto it. Care must be taken to avoid bubbles.

- The substrate is spun at 3200 rpm for 20 s to produce a film thickness of 9 μm.

- The sample is placed directly onto the motorised XYZ stage in the lithography setup.

- The resin is then photocured using the μLED array and stage as required.

Figure 3.7: The film thickness results produced from the DekTak. Labelled (red rectangles) is the height of the glass coverslip substrate and the cured resist film (9 μm). The sharp peak is due to the deformation of material as the tape is removed.

Figure 3.8: An optical image demonstrating how the cured resin can be handled and mechanically flexed without damage. This grey film was cured on a flat microscope objective and easily peeled off and bent.

- The cured features are then developed by submerging and gently moving it in toluene for 10s before being rinsed in DI water.

- The finished sample is then gently dried with a flow of nitrogen.

Although the toluene used in development is removed with DI water, despite it not being soluble to it, the use of water-miscible solvents such as IPA or methanol is not possible due to the degradation of the cured photoresist. Once the material is cured it also shows a good resistance to physical damage. This extends to being resistant to scratches and mechanical stresses such as bending and tearing. An example of this is shown Fig. 3.8.

As some of the chemical components of the resin are unknown due to it being a commercial material, H^1 and C^{13} nuclear magnetic resonance (NMR) spectra were taken. These are shown in Fig. 3.9 respectively and were performed by colleagues at the University of Glasgow[1].

These spectra show the presence of several components. The first is isooctyl acrylate which is a monomer that becomes part of the final cured structure. The second is urethane acrylate which is a photocurable oligomer. This is a generic description as

---

[1]Thanks go to Joseph Cameron for taking the above H-1 and C-12 spectra
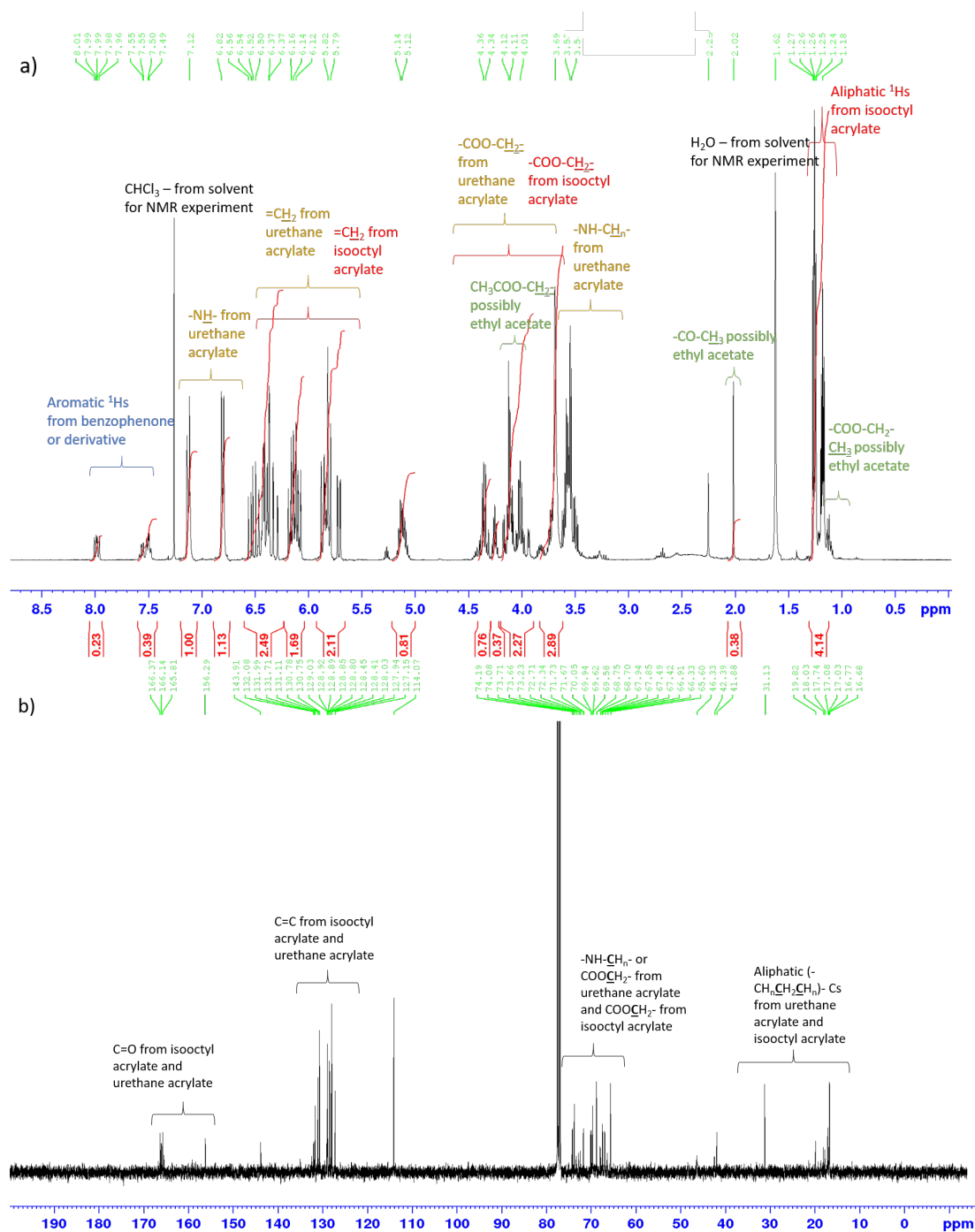
Figure 3.9: The a) H-1 and b) C-12 NMR spectra of the resin used in photocuring experiments.
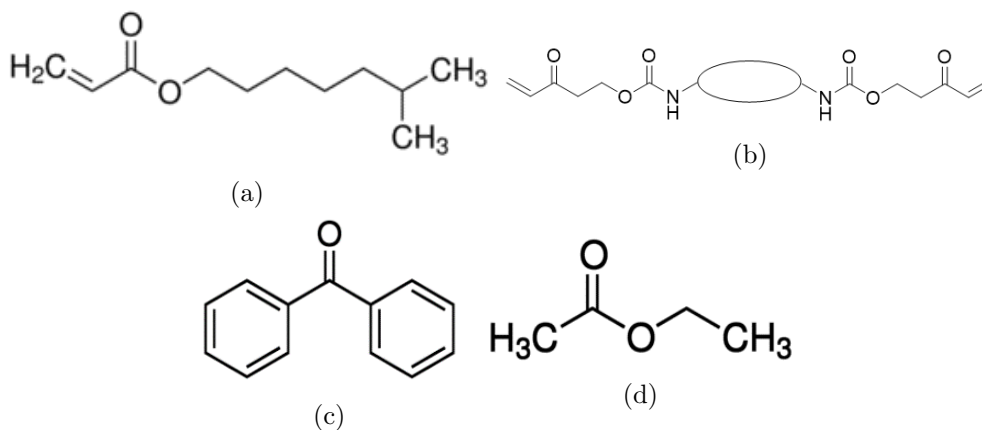
Figure 3.10: The skeletal structures of the three components seen in the resin through nmr spectroscopy. a) isooctyl-acrylate b) urethane-acrylate c) benzophenone d) ethyl-acetate

the middle block of the molecule cannot be determined using NMR. It is unlikely to be aromatic (containing benzene for example) as there is no signal in this region from the NMR, therefore it could be either a straight alkyl chain, cyclic alkyl chain or a combination of these. The other identified components are benzophenone which is a photoinitiator, and ethyl acetate which is a solvent allowing for the product to be spin-coatable. This is in line with the documentation of the material, however it cannot be ruled out that what is used in this blend is a slight variation. These molecules are shown in Fig. 3.10.

Although this resin was used throughout this work, other photosensitive materials can be used as required.

3.4 Maskless Photocuring results

The LED-based photolithography setup is capable of producing three different styles of features. These are individual spots from static exposure, straight features and curved features. An example of static features in shown in Fig. 3.11. Here the IOP logo was produced by simultaneously activating selected pixels within the LED array. This is also a good example of how spatial encoding of the emitted light can allow for multiple
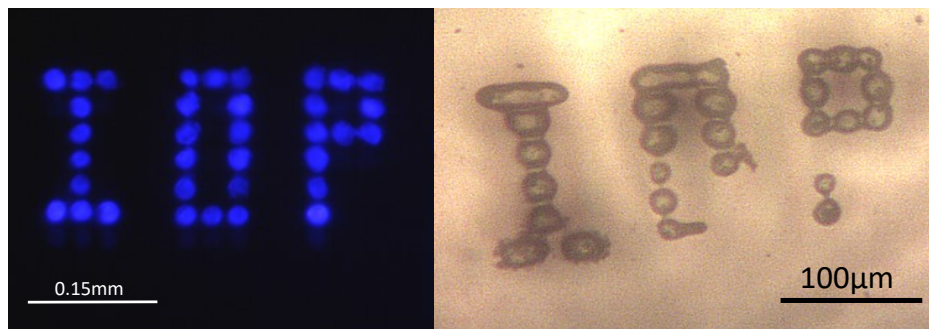
Figure 3.11: An optical image of a) the emission of selected pixels spelling the IOP logo and b) the resultant cured photoresist. The missing material in the cured structure is due to underexposure from LEDs with degraded performance compared to the average across the array.

areas within the FOV to be simultaneously exposed. This figure also shows how the physical shape of the LED emission region effects the physical shape of the resultant features. These features were fabricated using circular pixels with a 72% fill factor, thus resulting in a similar fill factor in the cured features.

The second type of feature which can be fabricated are continuous lines. Continuous lines also test the system's ability to create uniform and larger continuous structures. Such lines are created by moving a single axis of the stage during exposure. Whilst the line length is dictated by the translation distance, the line thickness is governed by both the optical spot size and the exposure dose. Line thickness control can be achieved by either altering the stage velocity, i.e. for slower speeds there is a higher exposure dosage, or by reducing the duty cycle of the illuminated pixels. Fig. 3.12 shows how the change in duty cycle can produce linewidths ranging from 14-35 μm as measured by an optical profiler (Wyko NT1100). Here we chose to modify the duty cycle and not the stage speed so we could maintain high writing speeds. The duty cycle, along with the stage speed, can be redefined at any point during the curing process allowing for continuous structures of varying width or multiple independent structures to be generated within the same fabrication process. Fig. 3.13 shows how the lines produced in this setup give good uniformity along their length. Note that the difference in linewidth in x and y directions is due to different stage velocities for the different axes and is a result of the
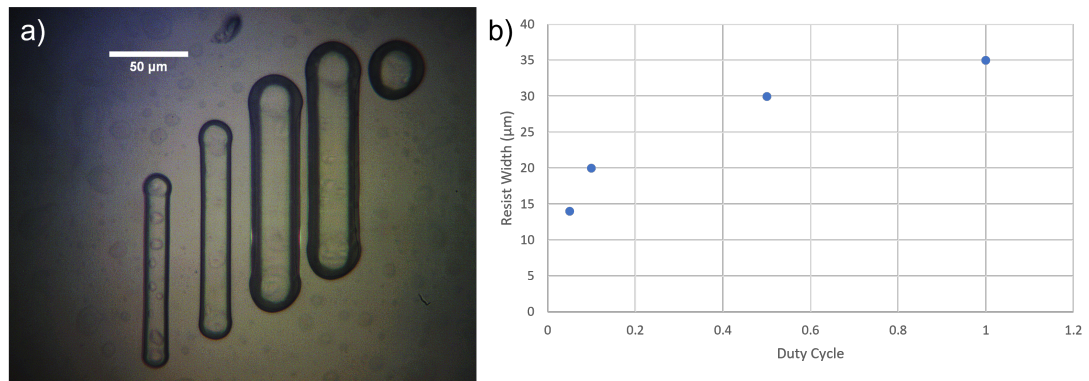
Figure 3.12: a) An example of different resist line thicknesses created by altering the duty cycle of the emitted light, ranging from 14-35 μm with a writing speed of 40 μm/s. Duty cycles of 0.05, 0.1, 0.5 and 1 were used from left to right. b) A graph demonstrating the resultant linewidths from differing duty cycles.

inherent stage performance.

The final variation of available feature are continuous curves. These can be achieved by translating both Y and Z stages with the same effective curing dosage as given in equation 3.1. Due to the limitations of the XYZ stage only a single axis can be moved at any given time meaning that resultant curves are a product of small linear increments. This means that smaller curved features will appear to be more like a step function whilst larger structures appear more curved though this is ultimately defined by the minimum step size of the motorised XYZ stage (0.5 μm). To minimise this effect the software control allows for the radius of the curve to be defined and the number of points across the curve vector the stage will move to. With an increased number of points the higher resolution the curve will appear. An example of a straight line transitioning into multiple sized curves is shown in Fig. 3.14. This also demonstrates how more complex structures can be developed and that classic masks are not required for the reliable fabrication of photocured structures.
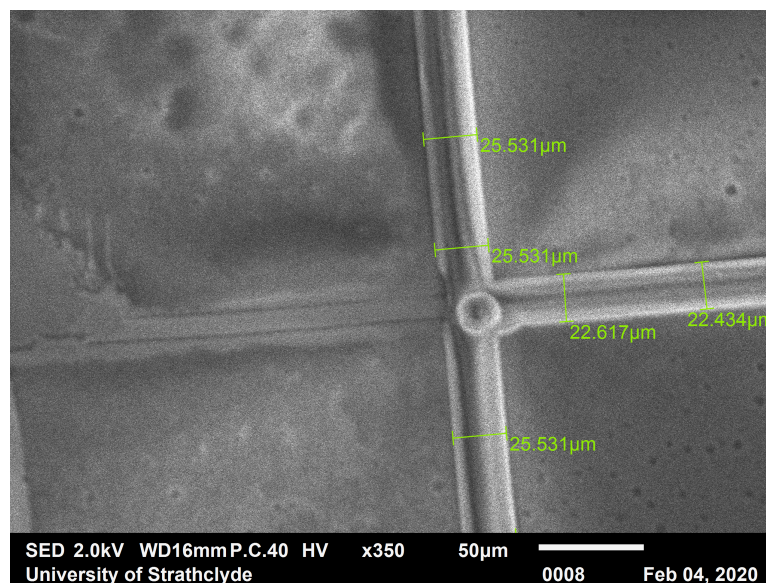
Figure 3.13: An SEM image of a photocured cross with an alignment marker in the centre. Shown are the line thicknesses across its arms demonstrating the sub-micron control of feature sizes.
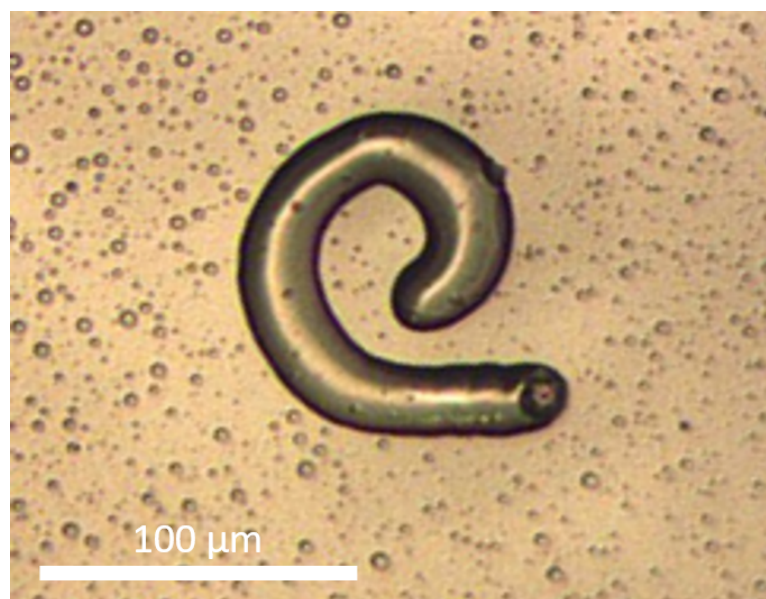
Figure 3.14: A photocured resist straight line transitioning into two curves of different radius. All three segments of the structure were completed within a single run.

3.5 Summary

This chapter discussed the design and implementation of a maskless μLED-based photolithography system. In this the spatio-temporal control made possible through CMOS drivers allowed for a maskless setup utilising monolithic LED arrays with individually addressable pixels. This was achieved using cheap and simple optical components mounted to a 60 mm cage system. The sample is placed on a motorised XYZ stage which is synchronised to the emission patterns of the LED array allowing for continuous structures to be created.

The profiles of the projected optical spots were investigated showing how the inherent intensity profiles produced by the used μLEDs are suitable for photolithography applications due to their top hat shape. Along with this, the power output of the device is shown to be sufficiently high that the curing times are low.

The setup was shown to be capable of producing continuous structures of both controllable and uniform thickness. The thickness of any resultant photocured structures can be defined by manipulating the duty cycle of the exposure patterns giving a range of line widths between 14-35 μm, though this range can be further altered through controlling the stage translation speed as required. Also presented in this chapter is the system's capability of producing curved structures along with linear patterns. These curves also show a uniform and controllable linewidth. All exposure patterns and stage movements are controlled and defined through a MATLAB^{TM} interface.

Bibliography

[1] Z. Gan, Y. Cao, R. A. Evans, and M. Gu, "Three-dimensional deep sub-diffraction optical beam lithography with 9 nm feature size," *Nature Communications*, vol. 4, no. 1, pp. 1–7, 2013.

[2] R. Menon, A. Patel, D. Gil, and H. I. Smith, "Maskless lithography," *Materials Today*, vol. 8, no. 2, pp. 26–33, 2005.

[3] M. T. Gale, M. Rossi, J. Pedersen, and H. Schuetz, "Fabrication of continuous-relief micro-optical elements by direct laser writing in photoresists," *Optical Engineering*, vol. 33, no. 11, pp. 3556–3567, 1994.

[4] O. Krüger and R. Grundmüller, "UV Laser Processing for Semiconductor Devices: Highly flexible laser-assisted fabrication for gallium nitride based devices," *Laser Technik Journal*, vol. 10, no. 5, pp. 26–30, 2013.

[5] B. Guilhabert, D. Massoubre, E. Richardson, J. J. McKendry, G. Valentine, R. K. Henderson, I. M. Watson, E. Gu, and M. D. Dawson, "Sub-micron lithography using InGaN micro-LEDs: mask-free fabrication of LED arrays," *IEEE Photonics Technology Letters*, vol. 24, no. 24, pp. 2221–2224, 2012.

[6] M. Stonehouse, Y. Zhang, B. Guilhabert, I. Watson, E. Gu, J. Herrnsdorf, and M. Dawson, "Digital Illumination in Microscale Direct-Writing Photolithography: Challenges and Trade-Offs," in *2018 IEEE British and Irish Conference on Optics and Photonics (BICOP)*, pp. 1–4, IEEE, 2018.

105

Bibliography

[7] D. Elfström, B. Guilhabert, J. McKendry, S. Poland, Z. Gong, D. Massoubre, E. Richardson, B. Rae, G. Valentine, G. Blanco-Gomez, *et al.*, "Mask-less ultraviolet photolithography based on CMOS-driven micro-pixel light emitting diodes," *Optics Express*, vol. 17, no. 26, pp. 23522–23529, 2009.

[8] R. Guijt and M. Breadmore, "Maskless photolithography using UV LEDs," *Lab on a Chip*, vol. 8, pp. 1402–4, 08 2008.

[9] T. Naiser, T. Mai, W. Michel, and A. Ott, "Versatile maskless microscope projection photolithography system and its application in light-directed fabrication of DNA microarrays," *Review of Scientific Instruments*, vol. 77, no. 6, p. 063711, 2006.

[10] C. Jeon, E. Gu, and M. Dawson, "Mask-free photolithographic exposure using a matrix-addressable micropixellated AlInGaN ultraviolet light-emitting diode," *Applied Physics Letters*, vol. 86, no. 22, p. 221105, 2005.

[11] J. J. McKendry, D. Massoubre, S. Zhang, B. R. Rae, R. P. Green, E. Gu, R. K. Henderson, A. Kelly, and M. D. Dawson, "Visible-light communications using a CMOS-controlled micro-light-emitting-diode array," *Journal of Lightwave Technology*, vol. 30, no. 1, pp. 61–67, 2011.

[12] J. Herrnsdorf, M. J. Strain, E. Gu, R. K. Henderson, and M. D. Dawson, "Positioning and space-division multiple access enabled by structured illumination with light-emitting diodes," *Journal of Lightwave Technology*, vol. 35, no. 12, pp. 2339–2345, 2017.

[13] Newport, "Piezo XYZ Linear Stage, Triple Divide, 25.4 mm, Picomotor, M4, M6."

Chapter 4

Integration of Structured Light Positioning into the Direct Writing System

In the previous chapter, an optical lithography setup was introduced utilising CMOS integrated μLED arrays to provide spatio-temporal control over the emitted light. This chapter will describe the incorporation of a second similar LED array of a longer wavelength which will provide additional functionality through structured illumination. This additional array results in a system which is capable of automatically recognising and tracking a randomly located marker and aligning itself to it. An overview of the LED arrays used for this development will be provided. Through this chapter information on the development and characteristics of different types of markers will be explored. Finally, the results of the automated positioning system will be discussed, including its performance when combined with the photolihography aspect of the setup, in terms of repeat accuracy across multiple lithographic steps.

Different methodologies can determine a marker's spatial location through the projection of optical patterns, as discussed in Section 1.4. This is achieved by each pixel
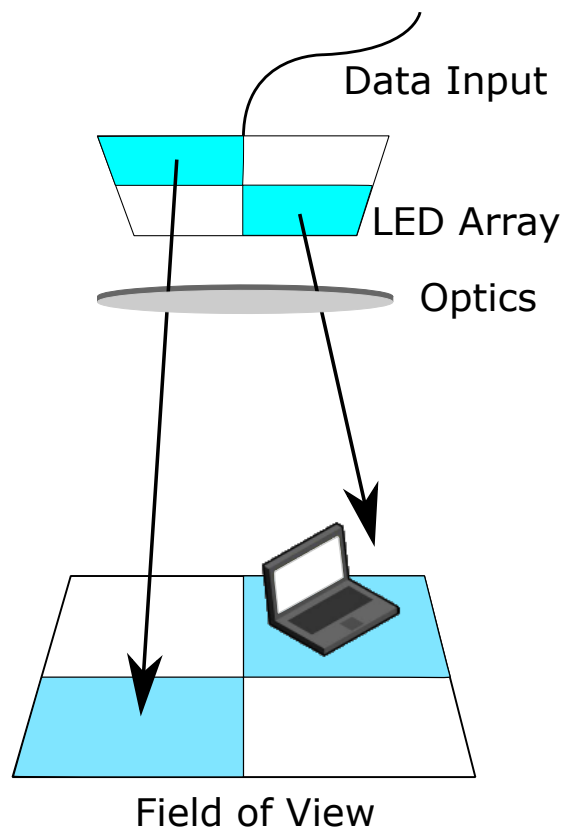
Figure 4.1: An example schematic showing how the spatial layout of an LED array directly translates into a similar checkerboard style layout.

within the LED array representing a coordinate of a projected 'chequerboard style' grid as shown by Fig. 4.1. Assuming that each pattern within a sequence of binary mask pattern frames is properly designed, each coordinate in the field of view (each chequerboard square) will receive a unique fingerprint data stream over the full frame sequence which can, in turn, be decoded to provide location information.

This section will demonstrate how this pattern projection can be utilised to achieve structured illumination based functionality.

4.1 LED Arrays and Target Characteristics

Optical signals can be generated through the use of CMOS controlled μLED arrays, as discussed in Section 1.3. The innate spatio-temporal control over a 2-dimensional array
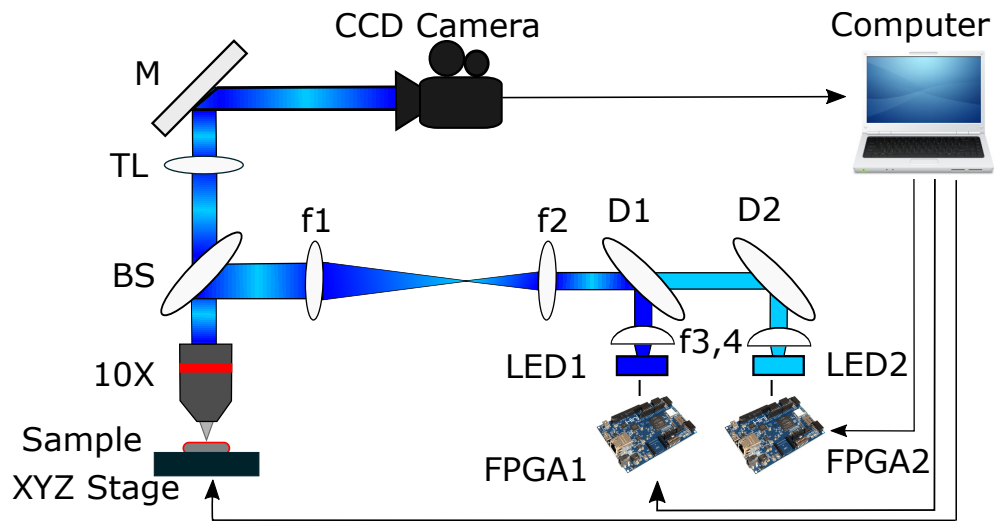
Figure 4.2: A schematic of the photolithography system. This also includes the second
array which can be used for additional functionality as well as the components required
for maskless photolithography.

allows for the projection of structured illumination patterns as defined in Section 1.4.

These CMOS devices allow for the individual LEDs to be modulated in a on-off fashion.

As the array directly operates from the output CMOS logic levels, it acts as a digital

to light converter and does not require a digital to analogue converter [1]. This has

previously been used for both the parallel transmission of OOK data streams and the

projection of structured light patterns [2, 3]. Here similar devices were incorporated

into a photolithography setup and used to provide support for an automated alignment

function.

4.1.1 CMOS Devices Used

Two CMOS-controlled GaN μLED arrays were used to perform photolithography while

implementing the automated alignment functionality. These arrays were both of 16×16

pixels with a 100 μm pitch and show a modulation bandwidth of $\approx$100 MHz, limited by

the maximum driving frequency of the CMOS electronics [4]. This is shown in Fig. 4.2.

A more detailed description of this setup and the optics involved are given in Sec-

tion 3.2.1.1. This shows how the second FPGA driver and associated μLED array can

be integrated into the setup without impacting the existing photolithography functionality. Care must be given to the alignment of this array so that the resultant optical spots at the sample from both arrays directly overlap. This is to ensure that that after alignment the correct area can be photocured. The process can be made made simpler by using the existing cage system and by mounting the array onto a manual XYZ stage for fine tuning. The light is collected in a similar way to the first LED array in that is is initially captured and collimated with an aspheric lens (f4) and added to the main optical path with a dichroic mirror (D2).

In order to be suitable for providing structured illumination in an optical lithography setup, the devices should satisfy certain criteria:

- The operating wavelength must be chosen such that it:

    - does not interact with either any photosensitive materials, or the substrate on which the photoresist is deposited.

    - does interact with any alignment markers should they require it, for example with these based on fluorescent targets.

    - does not overlap with the emission spectrum of any alignment markers, for example with fluorescence.

- The fill factor of the pixels must be suitably high so that the projected patterns reliably illuminate any alignment markers.

- The emission intensity profile of the projected spot must be suitably flat topped so that any markers which lie on the coordinate edge receive an adequate optical power.

Several of these points can be mitigated through choosing suitable materials as alignment markers, and are not an exclusive design criteria for the LED arrays. For example, using larger markers reduces the need for high fill factors, or the photoresist can be chosen to be sensitive at the wavelength emitted by the array.

110
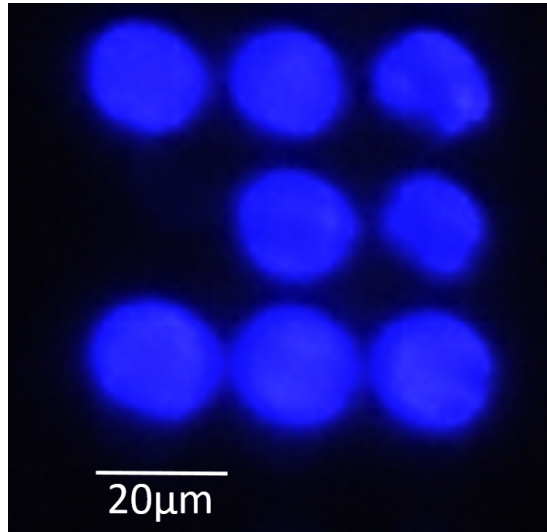
Figure 4.3: A projected and de-magnified 3 x 3 grid of circular pixels of 72 μm diameter and 100 μm pitch resulting in areas of no illumination, particularly in the corners of each LED site but with noticeable gaps around the entire edge.

The first of the CMOS driven LED arrays used comprised circular pixels with a 72 μm diameter, resulting in a $\approx 41\%$ fill factor. The operating wavelength in this case was centred at 405 nm. This is the same array which is currently being used for curing photoresists though the array was initially used to explore how different LED shapes and wavelengths can be used for structured illumination purposes. As shown in Fig. 4.3, after projection onto a substrate, there are large areas with no illumination between the pixels and especially in the corners of each coordinate. This can potentially cause issues as these dark areas can obscure any relatively small alignment marker that may be present and cause null readings.

Fig. 4.4 shows the spot cross-sectional power profile of a typical micro-LED within the array. It shows the typical pattern shown by similarly fabricated CMOS integrated devices as it has an inherent flat top with a FWHM measurement (17 μm) which is similar to the full beam spot diameter (20 μm). This satisfies the above criteria requiring a uniform power output across each pixel.

A 'heat map' of the output optical power density per pixel in the array is shown
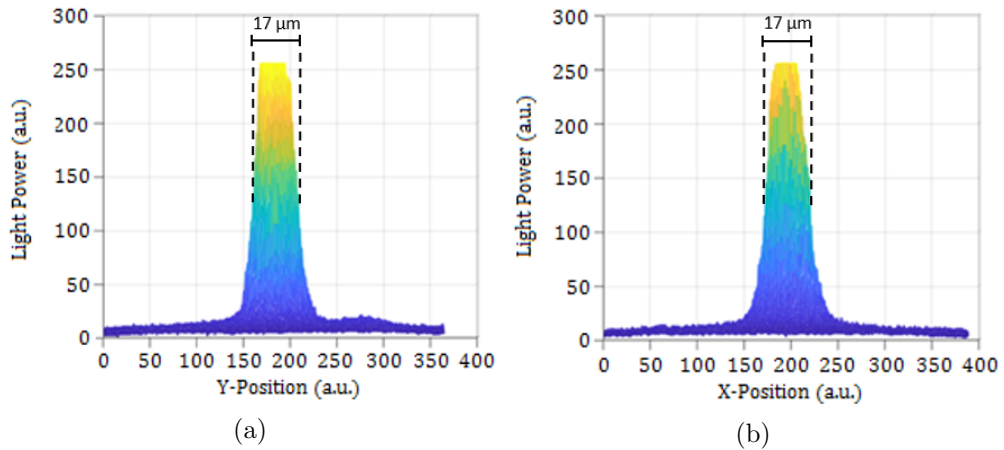
Figure 4.4: The intensity profiles of the optical spot of the 4th generation circular pixel device as seen at the substrate in the a) Y axis and b) X axis.

in Fig. 4.5. This shows an average power density of 4.87W/cm^2 across the array whilst operating at a current density of 1950 A/cm^2 per pixel. This map shows the non-uniformity's of pixel emission throughout with more severe degradation in the outer rows. The varied power output is likely increased by multiple pixels activating simultaneously whilst only addressing one, or reduced by problems with edge defects or short circuits made during the fabrication process. The outer pixels with an observed substantial increase in output power could also be influenced by reflections from the edge of the sapphire die. These defects can cause issues as they will provide a different intensity than expected from any alignment markers making it appear as though the marker has a greater or lesser surface area within that coordinate. This is important due to the fact that the entirety of a fluorescent marker will fluoresce when only a part of it is illuminated. If the marker is to react strongly to a neighbouring coordinate then it will give false readings. However, assuming adequate spectral filtering of the resultant fingerprints these non-uniformity's are seen to provide minimal issues as long as the resultant signal from the marker is strong enough.

The second array which was tested featured tessellated pixels each measuring 99 x 99 μm^2, resulting in a 98% fill factor. This device also has a higher central operating wavelength
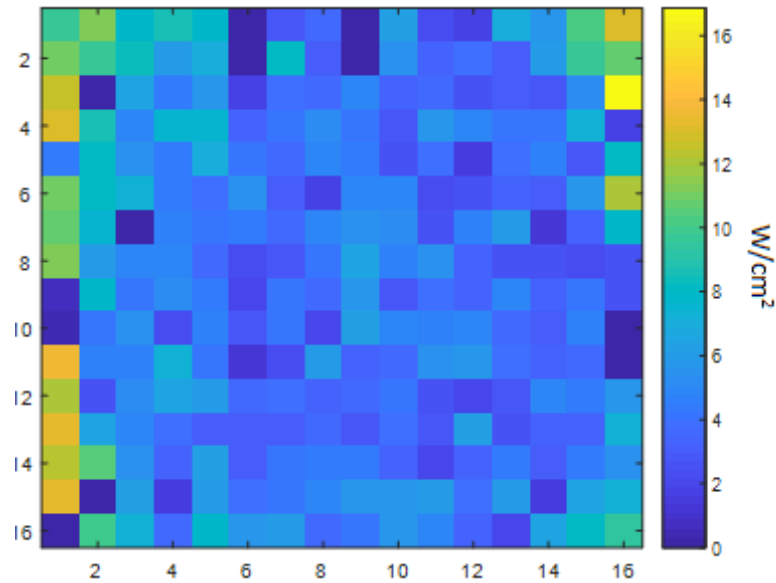
Figure 4.5: A heat map showing the power density produced by each LED within the LED array when individually modulated. This shows how the outer rows show a higher error rate with multiple pixels showing significantly higher power outputs.

of 450 nm which is further away from the typical i-line values common photoresists are sensitive to. By having a substantially higher fill factor, it allows for more reliable data acquisition as there is only a minimal area in which the marker can be obscured. This is shown in Fig. 4.6. A potential problem with this, however, is that by having a larger fill factor it increases the chance of overlapping optical spots due to beam divergence. Although this could potentially be used for sub-grid resolution by carefully controlling the amount of overlap, in this instance it causes problems. This is somewhat helped by the steep edges in the optical intensity profile as shown in Fig. 4.7b. This optical cross-talk is also reduced through the appropriate use of pattern projection and using explicitly coarse patterns.

As with the circular device, the emission profile shows steep sidewalls with a fairly uniform and flat top. Also like the circular device, this makes this profile a suitable candidate for structured illumination. Using the same optical setup as in Chapter 3, this device shows a projected spot size of ≈ 20 μm. However, again like the circular device, the full array shows consistent non-uniformities in power output throughout
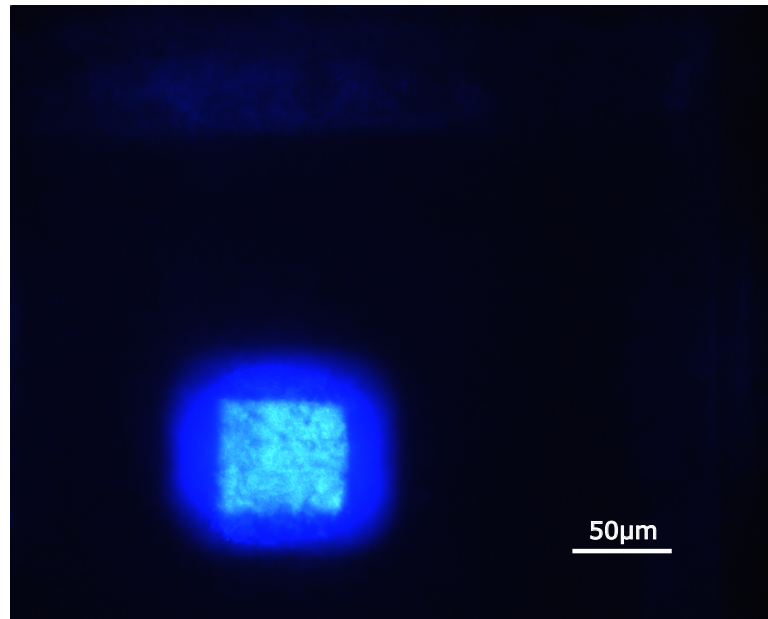
Figure 4.6: An optical image at the sample stage demonstrating the high fill factor of a 3×3 grid of the tessellated array showing full coverage within the FOV.

with more extreme values in the outer rows.

Both arrays were tested with the automated alignment functions described further below, although after comparing the two the tessellated device shows more promise due to its higher fill factor and longer operating wavelength.

4.1.2 Target Characteristics

During the photolithography process it is important to ensure that the correct areas of a sample are being exposed at the correct time. To achieve this, alignment markers are typically used as a reference point which can be aligned to prior to exposure. Here we investigate the use of such markers during an automated alignment process. For this work three different marker styles were investigated to test which would be the most effective. These were absorptive, reflective and fluorescent targets, respectively. All samples were made using borosilicate glass as a substrate. The main criteria which these markers had to meet is that they are easily distinguishable from both the substrate and the light from the structured illumination patterns. Additionally they should not

(a)   (b)
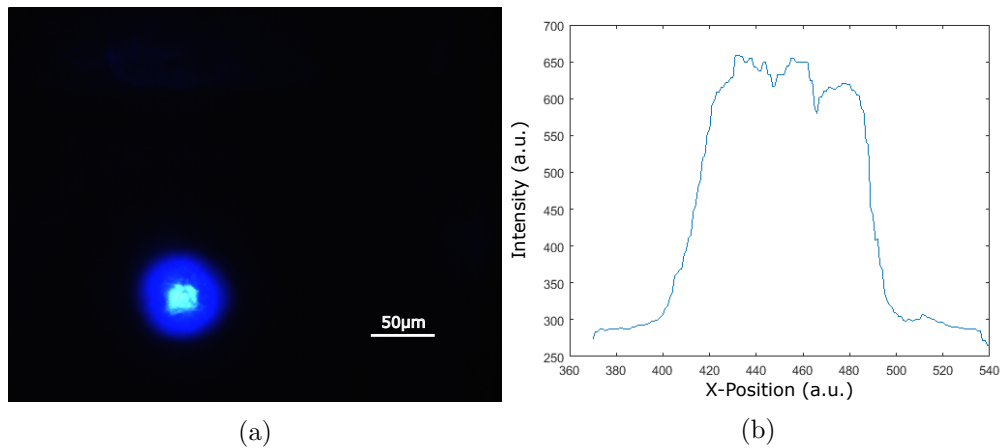
Figure 4.7: a) An optical image of the emission of a single LED within the array as seen at the substrate. b) The intensity profile of the same optical spot showing a relatively uniform profile power distribution across the spot with sharp rise and fall times at its edges.

interfere with any photosensitive materials whilst being spin coated or photocured. The latter also means that any materials used to fabricate them must not be damaged by any solvents in the resist itself or used during the development of the final structures. Another preferable criteria is that these markers can be easily and cheaply applied in order to optimise any production processes. As normally implemented alignment markers are etched into the substrate which requires a customised quartz mask to define its size and shape which adds additional costs onto any fabrication methods.

4.1.2.1 Absorptive Targets

The first style of target investigated used materials that would absorb the light from the LED illumination patterns and provide a contrast to the surrounding illumination by having an area of lower intensity. This was achieved by using a photosensitive material and curing a desired shape which could then act as the marker once the excess material was cleaned away. In this way the marker can be applied both cheaply and without permanent damage to the substrate. Two different materials were used to test this method. The first was SU-8, shown in Fig. 4.8a, and a photosensitive resin (ANYCU-

115

(a)   (b)
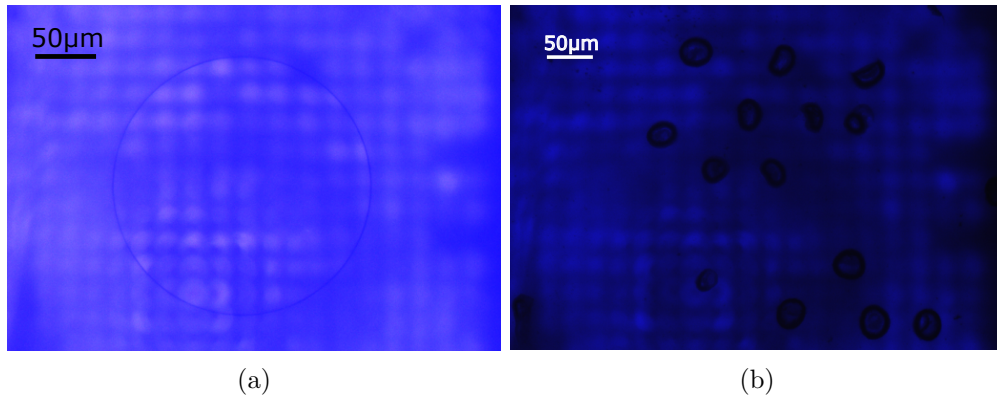
Figure 4.8: Plan view optical micrograph of a) an alignment marker fabricated with SU-8. This material shows no contrast across its surface with only minimal shown within the sidewall. b) multiple markers created with a photosensitive resin showing similar performance with only spectral shifts in the sidewall.

BIC), shown in Fig. 4.8b. As shown in these figures, the materials provide little to no contrast with the background illumination due to these materials having low absorptive properties for blue light. The resultant images with an absorptive marker present were simply too similar to the initial projection pattern, with any areas of absorption being similar to any coordinates being illuminated by a damaged or degraded LED. Along with this, due to the imperfect fill factors of the LED arrays themselves, should the materials have proven more effective then they would have blended with areas between pixels. Within the markers themselves there is also inconsistent absorption with the side walls being significantly more absorptive than its main body. Should these materials have proven more suitable, this property would have caused issues regardless, as the inconsistencies would create errors when trying to find an area with the biggest intensity change after filtering, as discussed in section 4.2.1. This is because the coordinate which had the largest length of sidewall would be seen most clearly and not the coordinate which had the largest surface area of marker.

A practical problem with using materials which are specifically designed for absorbing light is that they are typically unsuitable for use with solvents and are expensive when compared to other suitable materials [5,6]. Overall, then, we found that absorp-
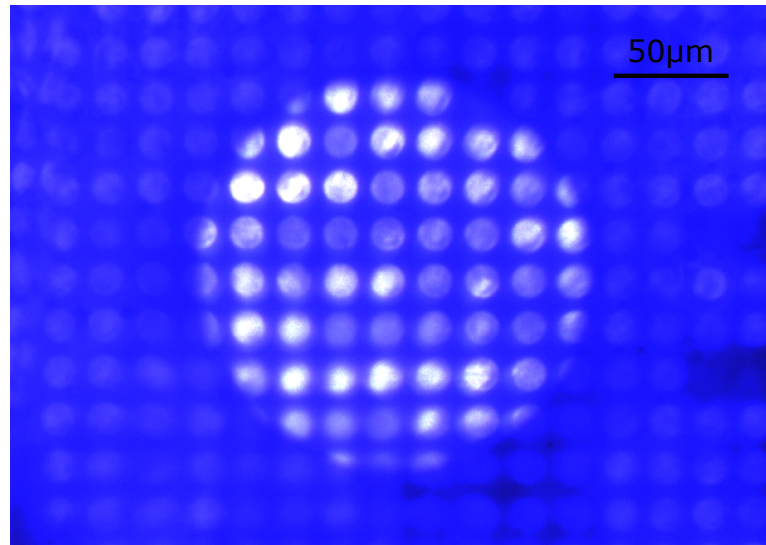
Figure 4.9: Plan view optical micrograph of large TiAg target (diameter of 170 μm) under full illumination from the LED array (circular pixels) demonstrating its high reflectively and spectral shift when compared to the blank substrate (surrounding area).

tive targets were not suitable for the alignment purposes required for this application.

4.1.2.2 Reflective Targets

As absorptive materials were found to be inadequate, reflective targets were investigated. For this, TiAg and aluminium targets of varying sizes were made through PVD sputtering. A large (i.e. fully encompasses multiple coordinates) target was created to test the uniformity of reflections across its surface, as shown in Fig. 4.9. This shows that the surface reflections are uniform and there is a clear contrast between the background and the target. The non-uniformities shown in the resultant images align with the non-uniformity in the projected light intensities from the LED array. This means that this type of material can be easily used as a marker, although this large example is unsuitable due to its size being considerably larger than each coordinate with the projected pattern.

A smaller aluminium marker ($\approx$20 μm diameter) was exposed to the 'moving bars' scanning pattern sequence, introduced in Chapter 1. Each frame was then extracted

(a)   (b)   (c)
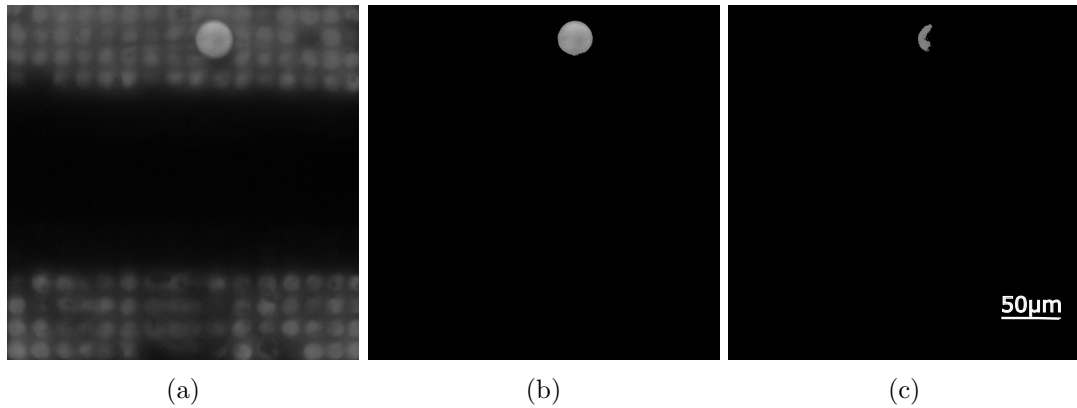
Figure 4.10: Plan view optical micrograph of a) a representative frame from the moving bars pattern sequence which illuminates a reflective Al target before and b) after a spectral filter is applied. c) A frame after filtering which only half illuminated the target from the same alignment data set. The Al markers are 20 μm in diameter.

and spectrally filtered in the same way as for the absorptive targets. This process was successful as illustrated by Figure. 4.10a/b showing the same frame before and after the spectral filter respectively. Figure. 4.10c shows the target whilst only half illuminated.

Although the results from using reflective targets are promising, there are a few problems with this approach. Firstly the fabrication process requires the aluminium marker to be deposited onto the substrate which requires specialised equipment. Also, the non-uniformities in the LED array can cause issues. If a pixel is faulty or has degraded, then a weaker reflected signal from the marker will be seen and some or all of the reflections can be filtered out. This is shown by the non-perfect edges in Fig. 4.10b/c. Another issue with this technique is that it introduces limitations on what substrates are compatible with the marker. For example, metallic or other reflective substrates will also provide reflections which will be similar to the marker. Along with this the substrate will have to be suitable for the PVD deposition of the metallic marker, which may not be possible with some materials.

(a)　　　　　　　　　　　　　　　(b)
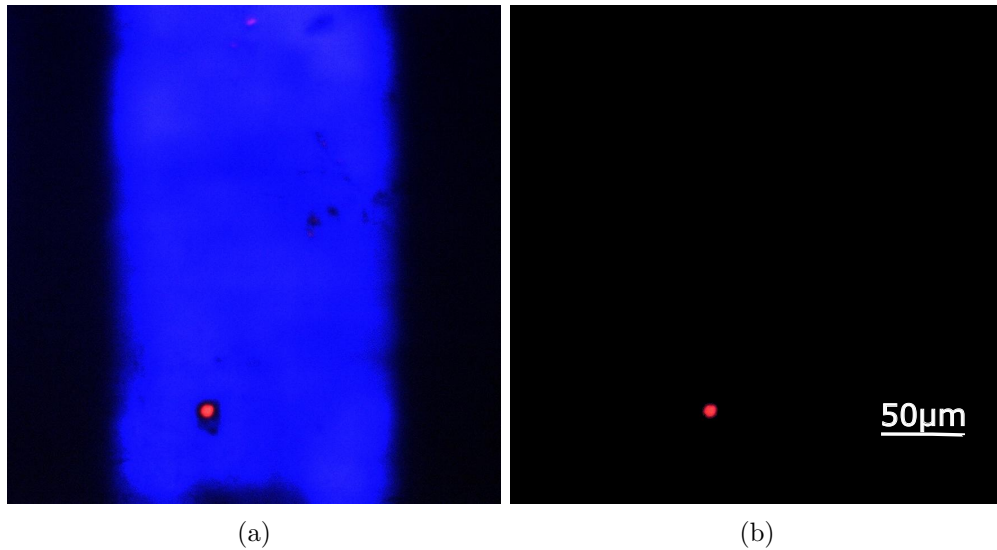
Figure 4.11: Plan view optical micrograph of representative frame from the moving bars pattern sequence illuminating a QD cluster a) before a spectral filter and b) after the spectral filter is applied removing the blue excitation light.

4.1.2.3　Fluorescent Targets

The third style of alignment marker investigated utilised fluorescent materials (here quantum dot clusters developed at the 'Institute of Photonics' and commercially available fluorescent microbeads purchased at Cospheric). The operating principle here is that when exposed to certain wavelengths, the fluorescent material will absorb light and emit at a longer wavelength. This light can then be used to provide a high contrast signal which is somewhat independent of the non-uniformity's within the LED array emission intensity. The materials chosen for this test were sensitive to blue light and emit red, with further details provided in Section 4.2.2 and 4.2.3. As with the other materials the 'moving bars' pattern sequence was projected onto a example marker of this material and then each frame was spectrally filtered to remove any background illumination. This is shown in Fig. 4.11, for the case where a cluster of colloidal quantum dots was used.

The spectral bandpass filter was able to remove all background light and leave a highly defined marker due to the high contrast given by the red emission. This
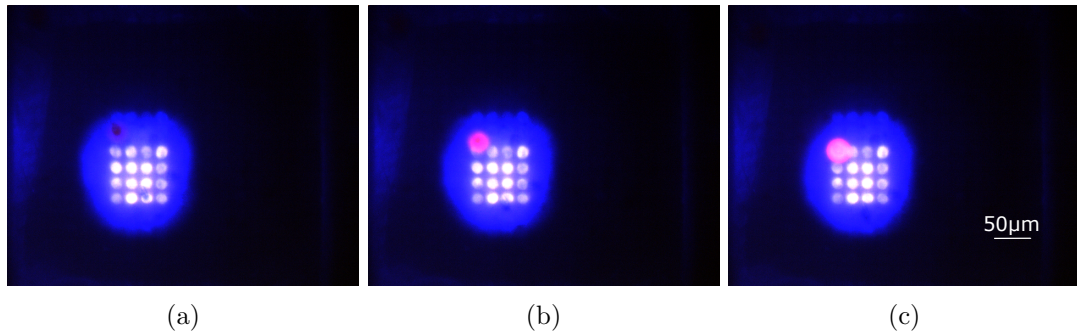
Figure 4.12: The different emission intensities of a fluorescent microbead under a) no direct illumination b) half the bead under direct illumination and c) fully illuminated. The diameter of the fluorescent marker is 25 μm in this case.

makes fluorescent materials a good candidate for alignment markers. Fig. 4.12 shows how these materials (in this case polyethylene microbeads) behave when only partially exposed to the illumination patterns. As shown, the marker fluoresces brightly whilst fully illuminated, fluoresces slightly whilst partially illuminated and remains inert when not illuminated at all. This behaviour is to be expected, however it raises an interesting point that whilst only partially illuminated the entirety of the marker fluoresces, albeit at a lower intensity. Despite this, if the marker straddles between two coordinates during the tracking process, then the coordinate in which it has the greater surface area will generate the stronger signal and will therefore be seen as its location. Another important point is that fluorescent markers such as these can be bought commercially (Cospheric) and can be dispersed onto the substrate as required without the need for specialist deposition equipment or additional growth steps.

4.2 Self Alignment and Positioning

This section will discuss the development of the automated alignment software and final fabrication process for creating custom structures of photosensitive materials whilst aligned to a marker. We will also include additional information on the practicalities of choosing and applying alignment markers. Next the section will go on to detail the

limitations of the equipment and how these may be circumnavigated through software control.

4.2.1 Software Development

The development of the automated positioning software was influenced by several external factors including the choice of pattern sequence and alignment marker. Other factors that played a role in the development included the limitations of the components used within the optical setup and the non-perfect characteristics of the LED arrays. With this in mind, the pattern sequence used for these tests was the moving bars series, as discussed in Section 1.4.4, and the alignment markers are based on fluorescent materials, as discussed in Section 4.1.2.3. The software itself was developed in MATLAB^{TM} and is simultaneously able to control the LED arrays and motorised XYZ stage whilst reading in information from the CCD camera. The LED array and CCD camera run asynchronously with each other so that the pattern sequence can be continuously projected and the data acquisition can sample as and when it needs to. By doing this it will provide more uniform general purpose illumination if required, and reduce the complexity of the software control.

The first consideration is what data rate the pattern sequence should be transmitted at, and in turn what frame rate the camera should be operating at. In this case, the limiting factor is the rate at which the laptop is able to read in the video frames at the chosen resolution. Consequently, the maximum rate at which the pattern sequence can be reliably read is 12 fps, and therefore the CCD camera will operate at that frame rate. The pattern sequence itself, however, cannot be run at this speed. Although the CMOS electronics are capable of running significantly faster than this, in order for the system to run the patterns and record the data asynchronously, it must be projected at a lower frame rate. This is because by running the pattern sequence at the same frame rate as the camera there is the potential to record the data during a transition period between patterns where multiple or no patterns could be shown at the same time. By

| (a) | (b) | (c) |
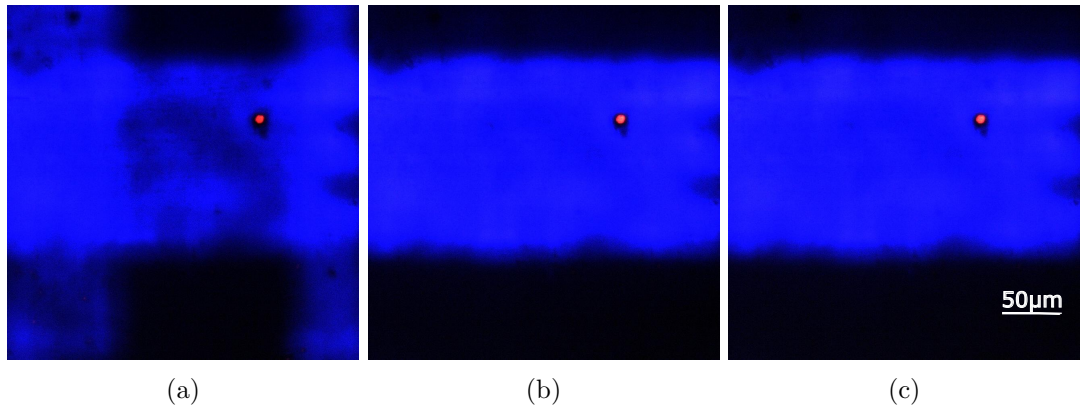
Figure 4.13: sEQUENCE OF IMAGES SHOWING of how a transitional image can be captured whilst the LED array changes pattern.

running the sequence at a third of the camera frame rate, three frames per pattern are recorded meaning that the middle frame will always record the correct data, providing the start of the pattern can be determined. This is still the case even if the first or third frame triggers during a transitional period, as shown in Fig. 4.13. For this to work, a way of finding the start frame of the sequence must be established. To do this an additional pattern was added to the positioning sequence which was simply blank. This then allows for a simple comparison of light intensities to be made across the full sequence and the frames with the lowest values would represent the start. Along with having a reliable start frame it is also important, when running asynchronously, to ensure that a complete sequence of thirty three frames is recorded. To do this each time the camera was triggered it would record 195 frames. This guaranteeD a complete sequence of 33 patterns with the blank frame being either at the start or end of the cycle, with each frame being imaged three times.

Another design factor which must be accounted for is that the patterns themselves will not be perfect, and that the environment in which this process is taking place may have sources of noise. This can be seen Fig. 4.14. Here an illumination pattern is defined and projected onto the sample, shown as the inside of the red outline. However, the pattern seen at the sample is different and features additional optical spots. This is
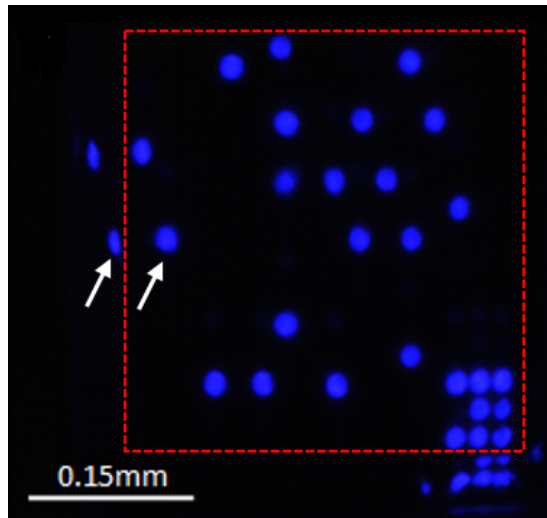
Figure 4.14: A projected pattern featuring 28 pixels of similar output power spread across the array. The red dotted array shows the intended outer perimeter of the FOV with the arrows highlighting the additional optical spots produced from peripheral spots within the frame. The red dotted line also shows where the spatial filter is applied to remove these artifacts.

due to the light of the outer rows of pixels in the array reflecting off the outside edge of the sapphire die, and being projected into the FOV as discussed in Section 3.2.2. These additional spots can cause problems for both the photolithography and the structured illumination. As this is due to the LED arrays themselves, this problem is unavoidable without fabricating LED arrays specifically with addressing this in mind. This problem can be resolved for photolithography by simply not using the outer rows of pixels. However, for structured illumination this acts as a source of noise which weights the light intensity measurement when trying to discover the pattern start frames. It may however be another cause of the higher output power intensity values seen at the array periphery.

This noise, along with any other light sources which are from the environment, can be removed by applying a pixel mask around the desired FOV and discarding anything outside it. An example of this is shown as the red dotted square in Fig. 4.14.

Further hardware issues were addressed through software control, such as the inaccuracies inherent to the motorised XYZ stage. These consist of the pico-motor step

movement of <30 nm which is attached to a stage with a resolution of 500 nm and a roll out of 2.5 μm [7]. This has the potential to lead to large errors when travelling across long distances (<1000s steps). To improve the accuracy of positioning results, the marker's current location is continuously tracked and fed into a differential controller so that after each XY movement of the stage its current location is determined and any refining movements to finalise its position to the desired alignment can be made. This is only reliably possible if the grid coordinates are small enough to be more accurate than the movement errors. This system essentially replaces the movement inaccuracies of the stage with any errors within the alignment system.

Other inaccuracies cannot be reasonably improved through software control. These can include having a <100% fill factor for the devices, leading to areas of non-illumination of the marker, and by having a marker which is too large. Ideally, the marker should be smaller than the individual grid coordinates to minimise the chance of it lying within several optical spots, but larger than the camera's maximum resolution to ensure detection.

The full flow of how the system determines the marker's location is as follows, and illustrated graphically in Fig. 4.16:

- **Pattern Exposure**. Here the moving bars sequence, along with the additional alignment pattern, is projected onto the sample. Simultaneous recording of the sample is done with the CCD camera.

- **Extract Frames**. Each of the 195 frames in the recording is extracted.

- **Spatial Filter**. Each of the frames has a spatial filter applied to remove any noise from outside of the FOV. This is shown in Figure. 4.15.

- **Define Start Frame**. Each of the frames' total pixel intensity is summed with the intensities of the frames before and after it. The cluster with the lowest intensity is deemed to be the three blank patterns and the middle frame is selected as the start point of the sequence.

(a)   (b)
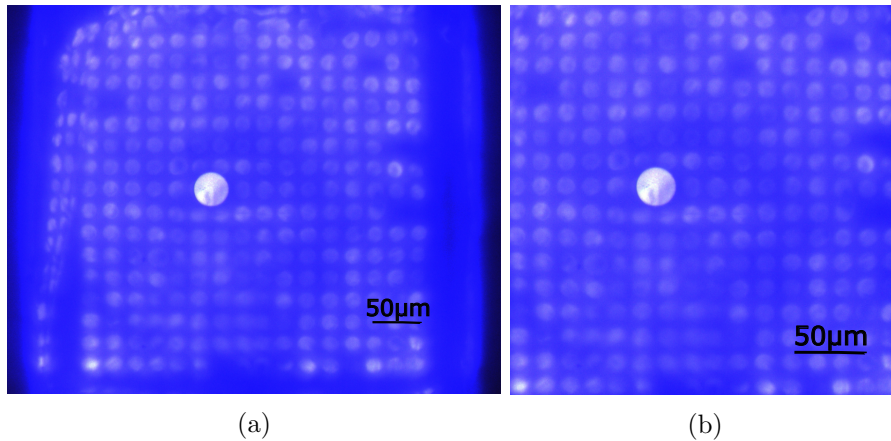
Figure 4.15: Plan view optical images showing how the artifacts created by reflections in the LED array packaging are removed with a spatial filter. a) The full image as seen by the CCD camera. b) The image after filtering, with everything outside of the intended FOV of the pattern projection removed.

- **Regenerate Original Pattern Sequence**. Every third frame from the designated start point is extracted to reform the initial 32 pattern sequence.

- **Spectral Filter**. The frames have a spectral filter applied which removes all colours apart from the red emission spectrum of the fluorescent marker.

- **Location Determination**. The 32 frames are then analysed to determine the markers location.

- **Stage Movement**. The stage is appropriately moved to align the marker to its pre-designated coordinate. Its location is continuously monitored and moved further when required until it is in its designated final location.

The array used for structured illumination is independent of the array used for photolihography and can therefore be used to continue to track the marker movements during that process. This also means that multiple alignments can be done for large structures.
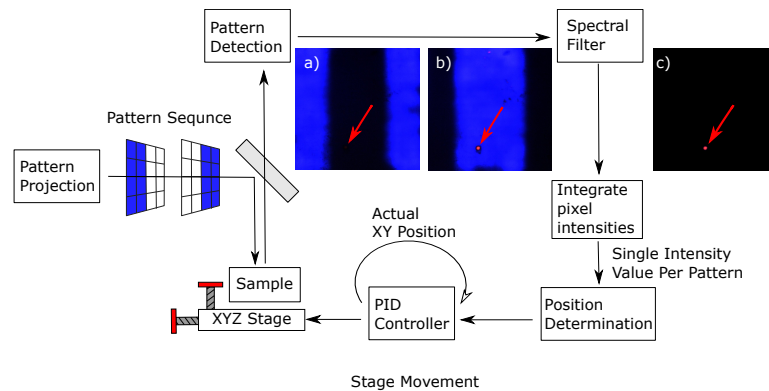
Figure 4.16: A schematic diagram showing how the pattern sequence is analysed. Insets: a) An example illumination pattern where the alignment marker is not illuminated. b) The inverse pattern of inset A where the marker is illuminated. c) The illumination pattern from inset B after the spectral filter is applied.

4.2.2 Quantum Dot Cluster Application

Several different fluorescent marker types were tested. The first were quantum dot (QD) micro-clusters made from CdSSe quantum dots with a ZnS outer shell. These clusters are approximately 20 μm in diameter with a peak emission of 630 nm, as shown in Fig. 4.17. The clusters themselves are stored suspended in deionised water. Although not optimised for 450 nm excitation light, the QD clusters are able to fluoresce sufficiently brightly for the camera and software to detect. When tested with the structured illumination patterns the software was accurately able to locate these microstructures.

These microstructures are also able to be in contact with the solvents present in photoresists and resins which allows them to be used in photolithography samples without them degrading.

Although these QD microstructures are able to be located and used with the resin, it was found that the QD/DI water left behind a residue of contaminants, or shown in Fig. 4.18. This residue proved difficult to remove as cleaning it before the resist was applied also removed the quantum dot clusters. Also if the residue was not removed, it would form either a base layer which the resist would sit on, lowering surface adhesion

(a)   (b)
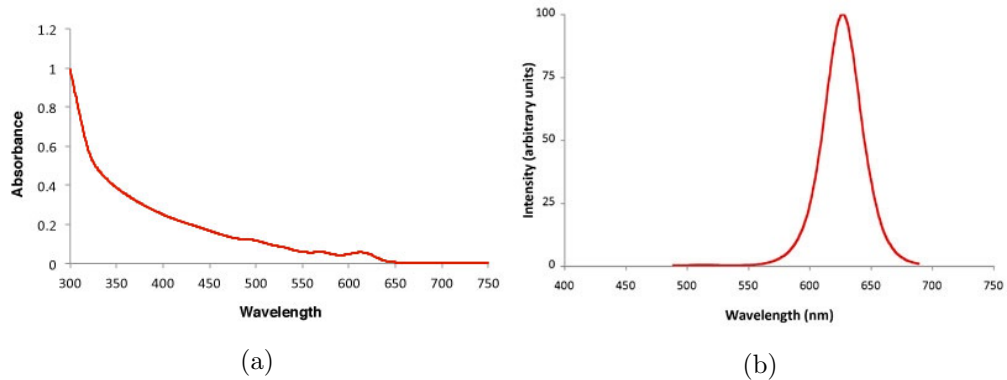
Figure 4.17: a) The absorbance spectrum of the quantum dot clusters. This shows a significant overlap with the typical i-line values common photoresists are sensitive to but with a reasonable absorption at 450 nm. b) The emission spectrum of the cluster with a peak at 630 nm and no overlap with the wavelengths used in the structured illumination patterns.

or even contaminating the resist itself, as discussed in Section. 4.2.4. Because of this problem, cured structures would seemingly randomly fail to adhere to the substrate and successful patterns would be created with a layer of irremovable contaminants.

4.2.3   Micro-Spheres

A second type of fluorescent marker that was tested were polyethylene microbeads. These have a peak emission wavelength of 607 nm and absorb at 450 nm as shown in Fig. 4.19, meaning that they are also suitable for structured illumination in our setup. Polyethylene is also able to interact with the photosensitive materials without degradation. The beads can be stored in a solution with deionised water making them practical to store and apply.

Along with having desirable qualities in terms of physical characteristics, these beads also do not deposit a layer of debris when drop cast onto a substrate. However, a potential issue is that during development the toluene degrades the beads which causes them to stop fluorescing. This typically is not a problem during a single exposure run but if multiple steps are required the beads lack of fluoresce means they cannot be tracked.
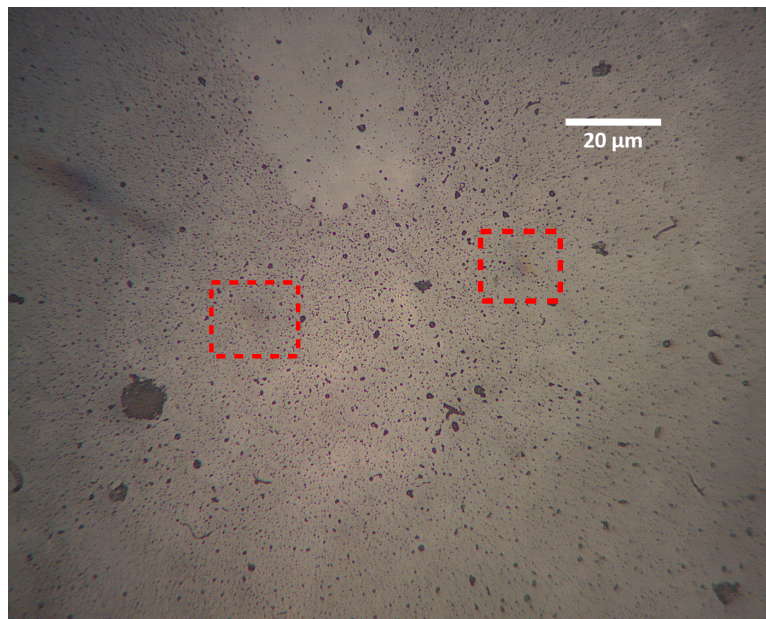
Figure 4.18: An image taken with a 10x microscope objective lens highlighting a residue and contaminants on the substrate after depositing quantum dot clusters. The slide was cleaned as described in Section. 3.3 prior to depositing the solution. Highlighted is the out of focus clusters.
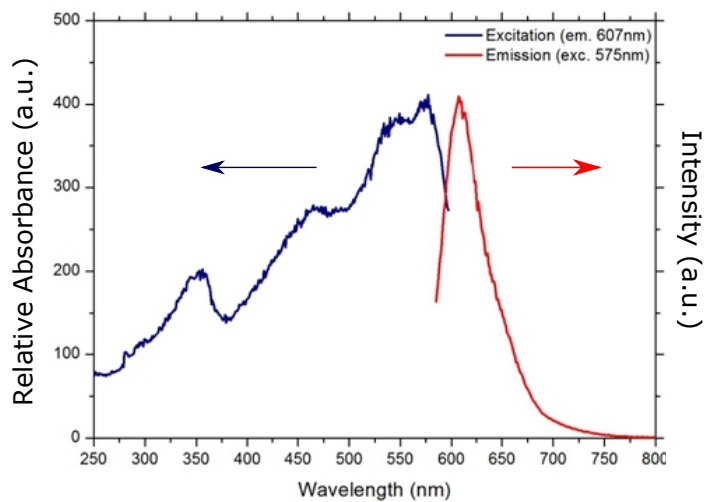
Figure 4.19: Blue) The microbeads' absorption spectrum and Red) photoluminescence spectrum

4.2.4 Marker Application

To start the alignment process the marker must first be deposited onto the sample. This can be done in several ways, although to test this system ideally the markers will be randomly distributed to ensure that the automated alignment can function with fully randomised marker locations. The first method tested was to deposit the markers by drop casting the marker-DI water solution onto the substrate, allowing the water to evaporate, then spin coating the resin on top as normal. By controlling the concentration of markers within the solution, and how much solution is deposited onto the substrate, the concentration and therefore the separation of the markers can be controlled. A problem with this technique is that solid material which is drop cast in this way is subject to the 'coffee stain' effect [8]. In this the material is deposited in rings centred about where the initial drop(s) land. This happens due to any liquid evaporating from the edges of the droplet being replaced by liquid from the centre via an induced capillary flow [9]. The flow of liquid also takes with it any suspended particles thus resulting in a ring formation once evaporation is complete. This means that the markers tend to cluster in certain areas and are therefore not randomly distributed. There are some methods to prevent this [10], although fortunately during the spin coating process the markers move with the resist and shift towards the edges of the substrate, thereby giving a more random distribution.

Another problem is that the quantum dot clusters' solution deposits contaminants. Drop casting the solution prior to applying the resist creates a layers of debris over which the film is spun. This not only gives a film of non-uniform height, as the debris is randomly deposited, it also means the resist has a lower adhesion to the substrate. Therefore, structures have an increased likelihood of lifting off during the development process. As the debris does not create a consistent layer, larger structures were seen to resist this effect somewhat due to having a larger area to adhere to the glass between contaminant islands. A further problem is that by having a layer of dirt underneath
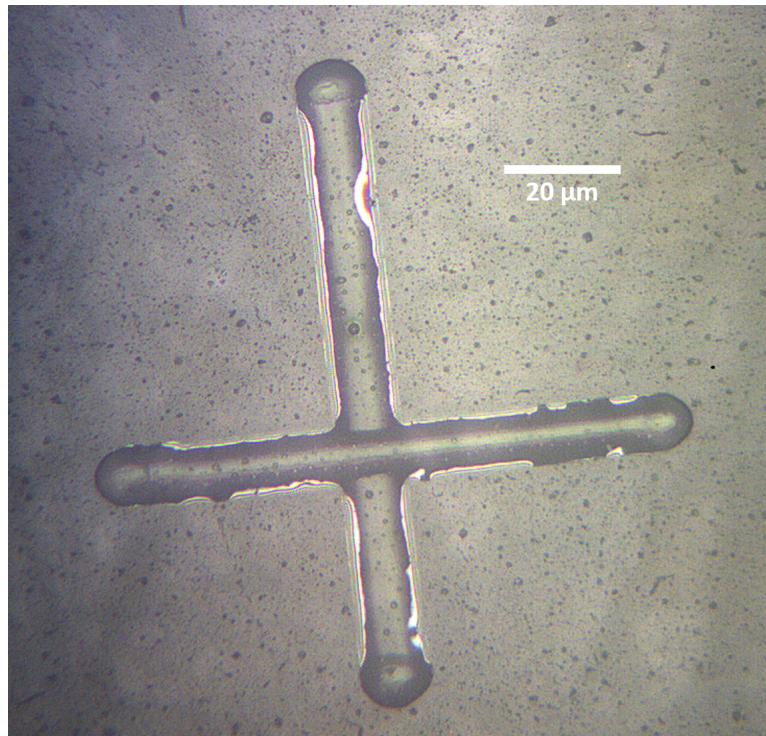
Figure 4.20: An optical image from the underside of the substrate showing where the development process causes under etching of the photocured structure due to removing dirt underneath it.

the structure, it means that in order to fully remove the dirt the cleaning process also under-etches the resist which can cause lift off. This is shown in Figure. 4.20. This results in dirty samples which are impossible to fully clean and maintain a structure.

The second method which was tested was to directly incorporate the markers into the resist. By doing this the initial step of depositing then drying the substrate can be skipped as the markers can be applied along with the resist. As with the previous method the concentration of the markers can be easily controlled before application, to ensure a sufficient separation to minimise the chance of multiple markers within the FOV and accidentally curing over other markers unintentionally. The contaminants present with the QD solution, as with contaminants in general, also present problems with this method. Although this was not tested, instead of producing a layer of debris underneath the resist, the residue would be incorporated and dispersed throughout the

resist and any resultant structure created with it. This could cause problems with surface adhesion, the photocuring process, the development process or the integrity of the material during processes after the photocuring process is finished.

4.3 Results

By incorporating structured illumination functionality, the production of photocured structures as described in Chapter 3 was achieved whilst aligned to non-standard and randomly distributed alignment markers.

4.3.1 Alignment Results

The quantum dot clusters and microbeads were seen to perform similarly during the alignment experiments.

Whilst using the moving bars pattern sequence, the tessellated device showed an average of two sets of XY movements to reach a designated coordinate from its random start position. Between each movement the marker's location was redetermined to ensure accuracy. The amount of XY movements required varied depending on how far the stage had to travel, with larger distances producing more XY movements. This is due to the inaccuracies inherent to the motorised stage. The most observed movements before the marker was seen at its target was three, with the start position being aligned to coordinate (1,1) and the target location defined at (16,16). This is the largest movement possible with the arrays we used. A plot of a quantum dots cluster's actual trajectory, along with its computed position as seen by the tracking algorithm, is shown in Fig. 4.21. In this test the marker was randomly positioned, seen to be at coordinate (13,11), and was moved to a pre-designated target location of coordinate (15,15). This alignment took two sets of XY movements to successfully complete and was achieved using illumination with the array with circular pixels.

Fig. 4.21 shows that the alignment process is still possible with an illuminating
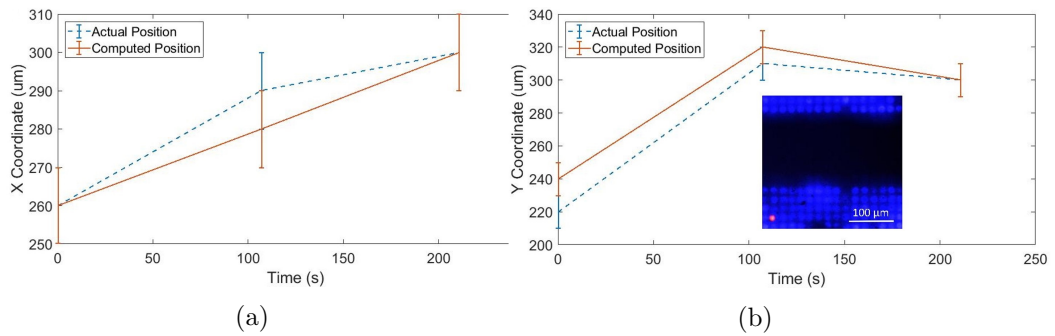
Figure 4.21: The movement of a fluorescent cluster during an alignment process. Shown here is the computed position determined by the structured illumination process and the actual position as monitored by the camera through conventional imaging. Error bars represent the coordinate grid resolution for the computed position and the pixel size and resolution of the CCD camera. a) The x-coordinate, and b) the y-coordinate with respect to time. The inset of b) shows an example frame in the marker's final position.

LED array which had a relatively low fill factor. However, the reliability of successfully determining the markers location is sometimes poor as the large areas with no light coverage can result in incorrect measurements. This is true when the marker happens to be in the corner of a coordinate and its main body cannot be seen apart from its edges which may lie in adjacent areas. This only happens a small percentage of readings and typically shows similar performance to the tessellated devices.

4.3.2   Photocuring to Alignment Marker Results

After the alignment function is completed the system can then operate as a maskless photolithography setup as described in Chapter 3. For these experiments the alignment marker itself was used as the starting location, or centre target, in order to encapsulate it into the polymerised structure for demonstration purposes.

Fig. 4.22 shows a developed cross with a QD marker at the intersection, highlighted with a red arrow. This was achieved by aligning to the markers, drawing a line, then re-aligning before drawing the second line. Fig. 4.22 also shows the extent of the contaminants across the substrate which could be removed. The alignment itself, however, shows a good accuracy with any inaccuracies within the tolerances brought on by the
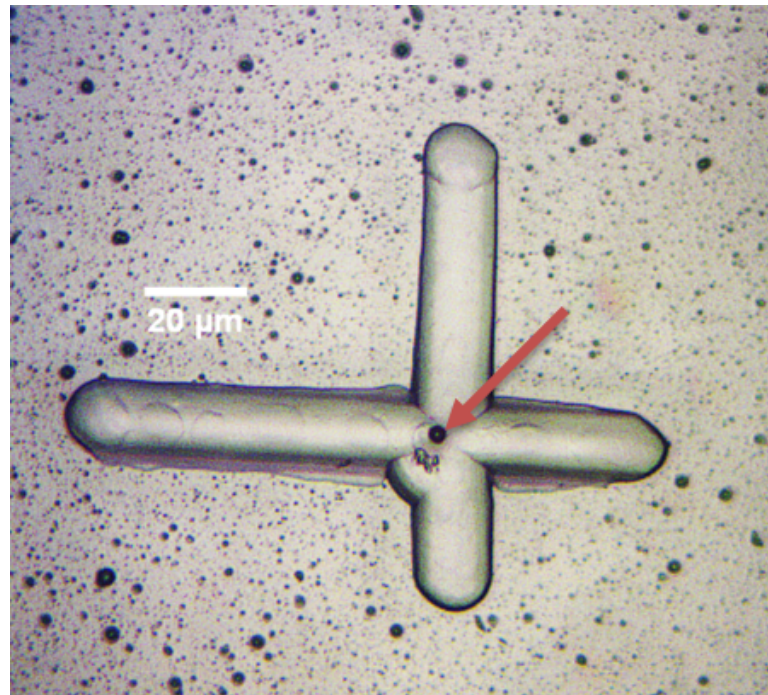
Figure 4.22: An optical image of the first photocured structure created with a fluorescent marker aligned to its centre. The red arrow highlights the fluorescent alignment marker.

spot size of the illumination patterns. The difference in arm lengths demonstrates how the inaccuracies in the stage motors results in inconsistent travel distances.

A similar structure created with an identical methodology, although with microbeads as the alignment marker, is shown in Fig. 4.23a with a 3D render demonstrating its profile in Fig. 4.23b. This clearly shows how the alignment capabilities are similar for both marker materials though with the microbeads the contaminants can be successfully removed post cure. Fig. 4.23b was created using data obtained with an optical profiler (Wyko NT1100), and shows that the structure remains uniform until reaching the marker. Note that the optical profiler is unable to resolve the microbead and is shown as an area of less than zero height.

Figure. 4.24 shows that the photocured lines are similar to those produced in the absence of alignment markers and additional materials. This demonstrates how the photolithography capabilities are not impacted by the introduction of fluorescent mi-
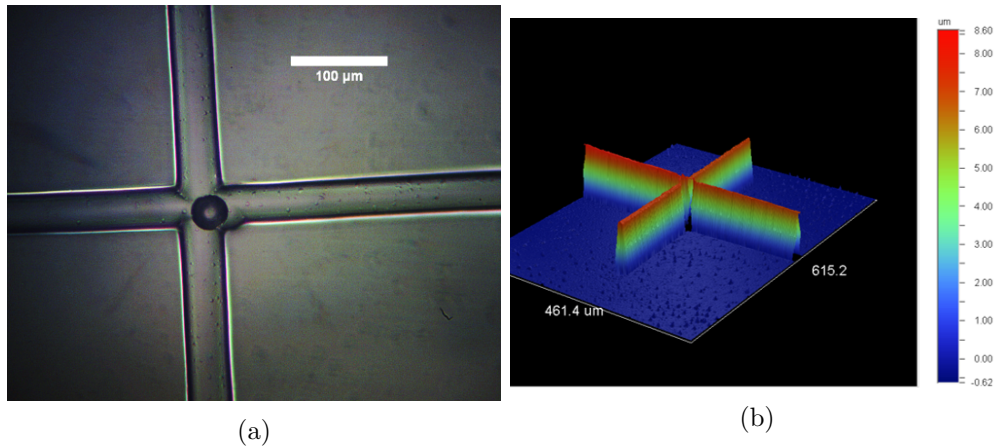
Figure 4.23: a) An optical image of a photocured structure created with a fluorescent marker aligned to its centre similar to that shown in Fog. 4.22 although with further cleaning steps to remove contamination. b) A 3D render created by an optical profiler showing the shape of the structure sidewall.

crobeads.

4.4 Summary

In this section a structured illumination based tracking and automated alignment system was introduced. By introducing a second μLED array of a suitably longer wavelength, spatially modulated patterns can be projected into the FOV which can provide information about a randomly distributed alignment marker. This was implemented onto the photolithgraphy setup described in Chapter. 3 without compromising any of the existing functionality. By utilising the existing driving software and camera, both the alignment and photocuring functions can be synchronised resulting in a 'smart' system which can constantly monitor the FOV and automatically correct any translation errors, whilst the same error correction can be applied during the photocuring process to ensure reliable finished structures.

Three different alignment markers were discussed with the most successful being fluorescent microbeads. These have been shown to be easily distinguishable from any background illumination allowing for precise tracking. Different methodologies of ap-
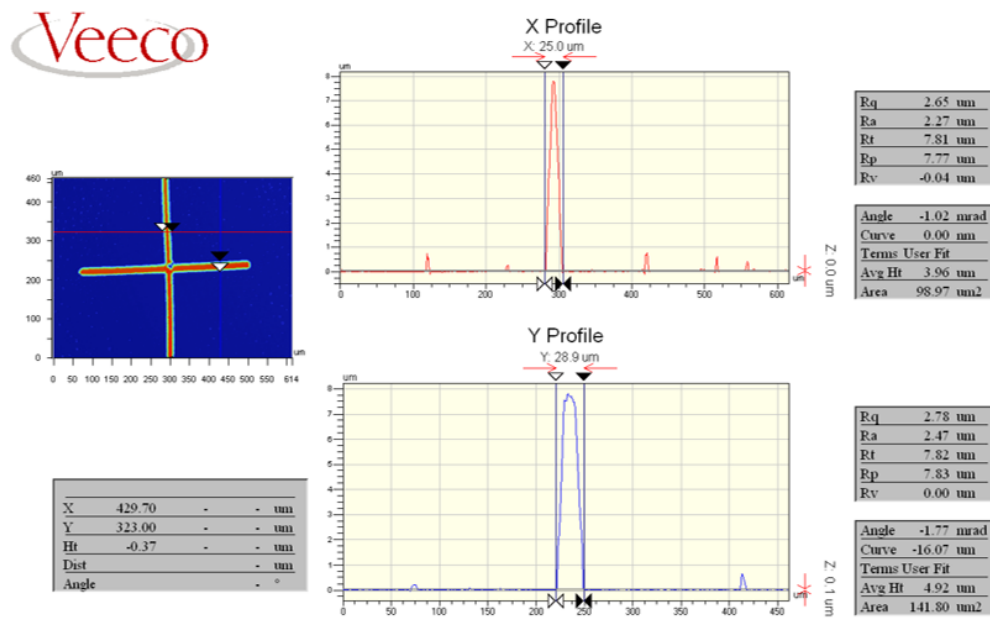
Figure 4.24: The line-width of the cross shown in Fig. 4.23a as measured by an optical profiler.

plying these markers were detailed along with an analysis on the impact of contaminants within any applied material and their effects on any photocured products.

The setup was capable of producing directly written structures whilst aligned to a marker which was demonstrated by encapsulating a marker within a cross shape, thus proving the system's ability to work reliably across multiple alignments.

Bibliography

[1] J. Herrnsdorf, J. J. McKendry, R. Ferreira, R. Henderson, S. Videv, S. Watson, H. Haas, A. E. Kelly, E. Gu, and M. D. Dawson, "Single-chip discrete multitone generation," in *2015 IEEE Summer Topicals Meeting Series (SUM)*, pp. 47–48, IEEE, 2015.

[2] S. Zhang, S. Watson, J. J. McKendry, D. Massoubre, A. Cogman, E. Gu, R. K. Henderson, A. E. Kelly, and M. D. Dawson, "1.5 Gbit/s multi-channel visible light communications using CMOS-controlled GaN-based LEDs," *Journal of Lightwave Technology*, vol. 31, no. 8, pp. 1211–1216, 2013.

[3] J. Herrnsdorf, M. D. Dawson, and M. J. Strain, "Positioning and data broadcasting using illumination pattern sequences displayed by LED arrays," *IEEE Transactions on Communications*, vol. 66, no. 11, pp. 5582–5592, 2018.

[4] J. J. McKendry, D. Massoubre, S. Zhang, B. R. Rae, R. P. Green, E. Gu, R. K. Henderson, A. Kelly, and M. D. Dawson, "Visible-light communications using a CMOS-controlled micro-light-emitting-diode array," *Journal of Lightwave Technology*, vol. 30, no. 1, pp. 61–67, 2011.

[5] P. W. Baumeister, "Optical coating technology," *Optimization*, vol. 10, p. 7, 2004.

[6] D. Zhu and S. Zhao, "Chromaticity and optical properties of colored and black solar–thermal absorbing coatings," *Solar Energy Materials and Solar Cells*, vol. 94, no. 10, pp. 1630–1635, 2010.

Bibliography

[7] Newport, "Piezo XYZ Linear Stage, Triple Divide, 25.4 mm, Picomotor, M4, M6."

[8] G. Berteloot, A. Hoang, A. Daerr, H. P. Kavehpour, F. Lequeux, and L. Limat, "Evaporation of a sessile droplet: Inside the coffee stain," *Journal of Colloid and Interface Science*, vol. 370, no. 1, pp. 155–161, 2012.

[9] R. D. Deegan, O. Bakajin, T. F. Dupont, G. Huber, S. R. Nagel, and T. A. Witten, "Capillary flow as the cause of ring stains from dried liquid drops," *Nature*, vol. 389, no. 6653, pp. 827–829, 1997.

[10] H. Li, D. Buesen, R. Williams, J. Henig, S. Stapf, K. Mukherjee, E. Freier, W. Lubitz, M. Winkler, T. Happe, *et al.*, "Preventing the coffee-ring effect and aggregate sedimentation by in situ gelation of monodisperse materials," *Chemical Science*, vol. 9, no. 39, pp. 7596–7605, 2018.

Chapter 5

Conclusion

LEDs offer a number of benefits which make them suitable for varied applications. μLEDs are an extension of this in that they offer high modulation rates when compared to conventional broad area devices. This thesis has described the development of a 'smart' photolithography tool which utilises two LED arrays to provide additional layers of complexity and allow structured illumination based capabilities such as object recognition and tracking. This technology has promise as it allows for maskless photolithography systems with additional functionality which is currently unavailable in commercial products. By fully utilising the advantages of μLED arrays with individually addressable pixels, and their ability to be directly bonded to and driven by CMOS electronics, this system can be re-purposed to perform a variety of tasks both cheaply and easily.

In chapter 1 the basic operating principles of LEDs, applications of light, CMOS electronics and structured illumination based pattern sequences were introduced. An emphasis was put on the applications of light and how modern LED arrays are capable of implementing structured illumination based functions. To achieve this functionality, the driving CMOS electronics was also introduced. Along with these, the theory behind photolithography was also discussed along with how modern emitters can benefit this field.

Chapter 5. Conclusion

Chapter 2 introduces how LED technology is versatile enough to be implemented across multiple different applications. Firstly, the fabrication of individually addressable n-electrode μLED arrays was presented. Reversing the typical p-addressable epitaxial structure allows for arrays to be driven by NMOS transistor based CMOS based driving circuitry. This has the advantage of having higher driving speeds and smaller driving electronics. Along with this, the fabrication process was optimised to improve pixel uniformity and yield. The VLC functionality of the device was demonstrated through multi-level encoding schemes driven by a custom built NMOS transistor-based CMOS driver. Secondly, a photometric stereo imaging setup was shown. This setup was capable of successfully rendering a 3D image using a single camera and four LEDs. These LEDs were operated simultaneously with individual contributions from each decoded using FDMA schemes. Along with this, a similar a similar system architecture was shown to be capable of 2-dimensional object tracking. Three-dimensional tracking was also demonstrated though to a significantly lower accuracy.

Chapter 3 discusses the design and development of a maskless photolithography setup which uses CMOS integrated μLED arrays as the light source. This setup was able to create uniform, customised structures in photosensitive materials at micrometre scale using a MATLAB interface. This setup is powerful as the array can be easily interchanged to provide different wavelengths and pixel shapes, etc, to suit the application requirements. Through using an array of emitters, multiple areas of the photoresist may be exposed simultaneously to mass produce repeating structures or create large structures more efficiently. We used this system to demonstrate the fabrication of both straight and curved structures of controllable width ranging from 14-35 μm. Control over the created structure properties comes from both the driving software, through PWM and manipulating the motorised stage speed, and by changing the simple optical components used within the setup.

Finally chapter 4 introduces a second CMOS integrated LED to the optical setup discussed in chapter 3 in order to incorporate additional structured illumination based

functionality. Integrating a second array with a longer emission wavelength than that used for photocuring, allows for a 'smart' lithography tool with features such as automated alignment and feature tracking. This setup was shown to be capable of tracking and aligning to non standard fluorescent markers which have been randomly distributed across a substrate to micrometre scale precision. Along with this, fabrication of structures in photo-sensitive materials are shown whilst aligned to these markers to the specifications shown in Chapter 3. A comparison of different alignment markers was discussed along with an evaluation of different LED specifications to test the limitations of the tracking software.

5.1 Future Work

Due to the multi-functional nature of the photolithography setup there are various ways in which it can be further improved. Firstly, by changing the μLED array responsible for photocuring to a device emitting in the deep UV, the direct write into photoresists can be achieved via photoacid generators without the need for fluorescent materials used in some photoresists. This goes hand in hand with the capability of the setup to be used to full characterise novel photoresists developed by colleagues at the University of Glasgow. With the easily controllable emission wavelengths, through changing the LED array, this setup provides the perfect testing platform for these materials. Alterations to the optical components within the setup will have to be made to host UV friendly optics, although these changes are limited to the easily changeable lenses.

Another essential improvement is changing the CCD camera used here to a spectrometer detector as the structured light positioning is required when a pixelated detector is not available. This will allow for hyper spectral imaging (HSI) and expand on the RGB wavelengths which we are currently limited to whilst imaging. The software to achieve this is already in place as the positioning software effectively mimics the input received through a HSI setup in that it uses structured illumination based patterns and

spectral filtering to decode the markers location. Another potentially useful detector to use would be a single photon avalanche diode. This would enable technologies such as surface profiling measurements which would allow for the setup to not only fabricate structures but to also characterise them. A potential method for achieving this would be through time of flight measurements utilising the same structured illumination pattern and emitters. With regards to the characterisation of custom photoresists developed at the University of Glasgow, this metrology capability could add further functionality and would allow for additional information to be extracted. Along with this, the implementation of a spectrometer probe as the detector would allow for any fluorescence within the materials to be observed.

Other potential improvements to the photolithography setup come in the form of additional automation of operating procedures. For example, by analysing the relative signal strength of each coordinate during pattern projection, it is possible to characterise the optical power intensity and hence performance of each element of the μLED array. This information can then be used to fine tune the duty cycle of each pixel to meet specific exposure dose requirements and optimise the physical size of any photocured structures. Other improvements to the software can come in the form of enabling the ability to read in multiple alignment markers simultaneously. This would be useful when creating a pattern over a significant area which expands outside of the cameras FOV and would require multiple alignment markers to sufficiently cover. In order to maintain a good alignment there will need to be a period where several alignment markers are visible to allow for a seamless transition between them. The distinction between markers could be done through physical size, shape or colour etc.

Appendix A

Publications

A.1   Journal Publications

M. Stonehouse, A. Blanchard, B. Guilhabert, Y. Zhang, E. Gu, I. M. Watson, J. Herrnsdorf and M. D. Dawson, "Automated Alignment in Mask-Free Photolithography Enabled by Micro-LED Arrays," Electronics Letters, 2021.

E. Xie, M. Stonehouse, R. Ferreira, et al., "Design, Fabrication, and Application of GaN-Based Micro-LED Arrays With Individual Addressing by N-Electrodes," IEEE Photonics Journal, 9.6, (2017).

A.2   Conference Submissions

M. Stonehouse, A. Blanchard, B. Guilhabert, I. M. Watson, E. Gu, J. Herrnsdorf and M. D. Dawson, "Microscale automated alignment and spatial tracking through structured illumination," 2019 IEEE Photonics Conference (IPC), IEEE, 2019.

Appendix A. Publications

M. Stonehouse, Y. Zhang, B. Guilhabert, I. M. Watson, E. Gu, J. Herrnsdorf and M. D. Dawson, "Digital Illumination in Microscale Direct-Writing Photolithography: Challenges and Trade-Offs," 2018 IEEE British and Irish Conference on Optics and Photonics (BICOP), IEEE, 2018.

J. Herrnsdorf, J. J. D. McKendry, M. Stonehouse, L. Broadbent, G. C. Wright, M. D. Dawson and M. J. Strain "LED-based Photometric Stereo-Imaging Employing Frequency-Division Multiple Access," 2018 IEEE Photonics Conference (IPC), IEEE, 2018.

J. Herrnsdorf, J. J. D. McKendry, M. Stonehouse, L. Broadbent, G. C. Wright, M. D. Dawson and M. J. Strain "LED-based Photometric Stereo-Imaging Employing Frequency-Division Multiple Access," 2018 IEEE Photonics Conference (IPC), IEEE, 2018.

Automated Alignment in Mask-Free Photolithography Enabled by Micro-LED Arrays

M. Stonehouse, A. Blanchard, B. Guilhabert, Y. Zhang, E. Gu, I. M. Watson, J. Herrnsdorf and M. D. Dawson

We present an automated control system for positioning on the micro scale, based on the principles of single pixel imaging and fluorescence. By using the projected output of a chequerboard array of CMOS controllable μ-LEDs at a suitable wavelength, we are able to spatially locate, track and automatically align to fluorescent markers. Using this system, positioning is demonstrated with accuracy on the order of 20 μm. We present a maskless photo-lithography system using the automated control capability and a second μ-LED array to photo-cure customisable structures in photoresist with alignment referenced to the fluorescent markers.

Fig. 1. Schematic of the optical setup

Introduction: Automated control is a vital part of any large scale manufacturing capability. To achieve accurate and scalable automation on the microscale is of profound importance in areas such as electronics and optoelectronics, where photolithography is often the technique of choice for wafer patterning and device definition [1]. Mask-less photolithography is an increasingly important lithographic technique, thus far dominated by use of lasers and digital micromirror-based sources for producing patterned exposure[2, 3]. The rapidly emerging gallium nitride μ-LED (Micro-Light Emitting Diode) technology, utilizing arrays of LED pixels with individual size from a few to a few 10's of microns directly interfaceable to CMOS (Complementary Metal–Oxide Semiconductor) control electronics, offers an attractive, versatile and power efficient alternative [4, 5]. This has shown to be independent of pixel shape, with square [4] and [5] circular pixels used.

In this paper we demonstrate the further potential of electronically-interfaced μ-LED arrays in achieving various alignment and control functions in mask-less photolithography. We specifically target microscale feature recognition and tracking capability to enable closed loop automated positioning. In our demonstration, spatio-temporally modulated illumination patterns at 450 nm were used to align to red-emitting fluorescent markers at arbitrary locations in the exposure plane, in the form of CdSe/ZnS colloidal Quantum Dot (QD) microstructures or dye-doped microbeads. Photoresist patterns aligned to the markers were then generated using illumination from a single 405 nm μ-LED within an array, and the programmed motion of an XYZ stage. We thus demonstrate a self-aligning, multi-step photolithographic capability, where μ-LED technology is used both to locate and align to fluorescent positioning markers as well as to define and expose further photo-patternable microscale features in registry with these markers.

Optical Setup: A schematic of the optical setup used for this work is shown in Fig. 1; a variant of this set-up was used in our earlier work [6]. Note that while we have used a CCD (Charge Coupled Device) camera here to give coarse spectral resolution, the imaging capability of the camera is not essential to the demonstrated operation and is only used here for monitoring and characterisation purposes. In the experiments below, we employ the principles of computational single-pixel imaging [7, 8] and therefore the same results can be obtained with a single-element detector in place of the camera. Both μ-LED arrays used were fabricated in the Institute of Photonics. The gallium nitride μ-LED array used in the photo-curing process (LED2) is a 405 nm wavelength (corresponding to h-line), 16×16 pixel array of circular pixels 72 μm in diameter and 100 μm pitch, giving a 41 % fill factor. The array used for structured illumination (LED1) is a 450 nm wavelength, 16×16 pixel 'chequerboard' array of square pixels of 99 μm edge length and 100 μm pitch, giving a 98 % fill factor. FPGAs (Field Programmable Gate Arrays) 1 and 2 control the LEDs. The μ-LED arrays were previously fabricated by a colleague(How should I finish this?). A series of lenses is used to collimate and image the respective outputs of the arrays, demagnified by a 10X objective to illuminate the sample stage. The respective f-numbers of these lenses are f/10 for f1, f/2 for f2, and f/0.8 for both f3 and f4. The setup shown here results in projected μ-LED spot sizes of $\sim$20 μm, defining the positioning precision.

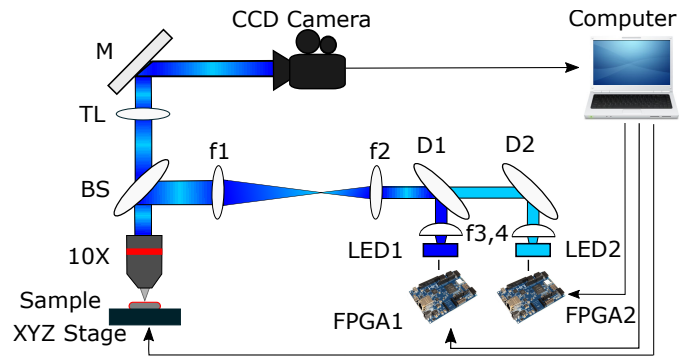*Sample Preparation:* In this work we have used borosilicate glass slides throughout as substrates on which to define photopatterns, with two types of fluorescent markers: red-emitting QD clusters, 20 μm in diameter and fluorescent dyed microbeads, (Cospheric fluorescent red polyethylene microbeads), 10-22 μm in diameter. The term "marker" used henceforth refers to both the QD clusters and the microbeads, and the experiments shown here can be done with either marker type. For microphotolithography, the QD clusters are added to the glass slide via an evaporation process to randomise the distribution of the clusters, to which resin was drop cast. The microbeads, in comparison, are directly added into a small amount of a UV (UltraViolet) sensitive acrylate resin (Anycubic clear UV resin), which is then drop cast onto the sample. This resin is light-sensitive enough at 405 nm for our purposes, whilst not curing when illuminated at 450 nm.

Automated Positioning: The first step in our demonstration is automated positioning. During automated positioning, the 450 nm wavelength LED array projects a sequence of chequerboard-style binary illumination patterns onto the sample with the X,Y position of each individual LED representing a coordinate on the board and in the image plane. We can send a series of custom illumination patterns (known as a 'Moving Bars' sequence due to its form [9, 10]) designed to create a unique temporally modulated 'fingerprint' at each location in the image plane. As these light patterns illuminate the sample they generate photoluminescence from any markers in the FOV (Field Of View) which can be detected remotely. Thus identifying the temporally modulated pattern of luminescence and relating this to the position-dependent modulation of the illumination permits the recognition and location of designated luminescent features within the FOV. The alignment process used a 450 nm wavelength LED array with a 98 % fill factor, so that the FOV has a near-continuous light coverage.

Fig. 2 shows the process sequence whereby the coordinates of the marker are obtained, with Fig. 3 showing camera images of representative frames from our pattern sequence. In this process the blue light from our emitter is removed by a processing filter, leaving only the luminescence the illumination produces from the specific markers. In general, this technique is not limited to blue light and/or red fluorescing markers, but rather can be applied to μ-LEDs emitting at any peak wavelength obtainable from gallium nitride devices in conjunction with markers capable of absorbing that light to produce longer-wavelength emission. Also shown in Fig. 2 is the PID (Proportional Integral–Derivative) control loop whereby the software uses the current location of the marker to manipulate the sample-mounted XYZ mechanical stage during alignment. The stagte is limited to 1 mm/s and 25.4 mm in the XY coordinates.

Temporally Modulated Fluorescent Response: To check the fluorescent response of the markers, markers were placed randomly on the glass slide. An area with only a single marker visible in the FOV of the 450 nm chequerboard array was then selected, and the full 'Moving Bars' sequence projected, with three camera frames recorded for each projected frame, recording the moving bars sequence twice. This ensures that the full pattern is captured and one usable frame is recorded for each projected frame.

The recorded frames are then spatially and spectrally filtered, only showing areas within the FOV of the LED1 array that record on the red channel of the CCD camera, showing the fluorescence. Then, the sum of the filtered image's intensity is calculated to simulate a single pixel detector such as a spectrometer. A rolling three frame sum is used to find the start frame; the smallest value for this sum indicates the start frame. If this start frame is calculated to be in the latter half of the recorded frames, it is shifted to use the full frame sequence.
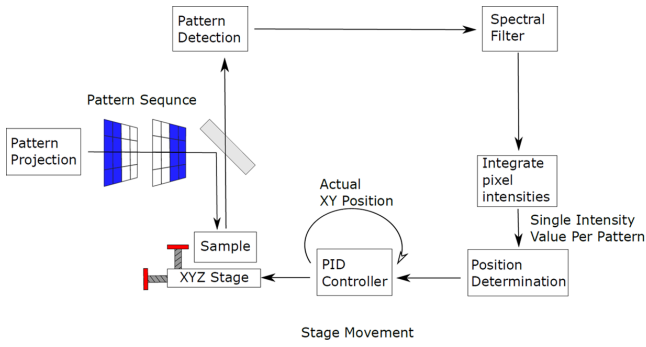
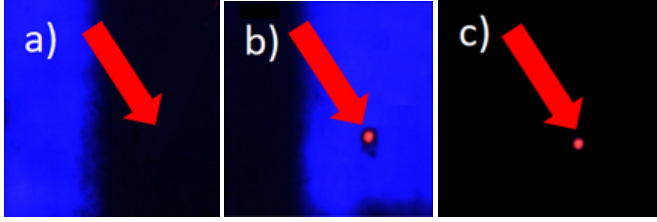Fig. 2. A schematic diagram showing how the pattern sequence is analysed.

Fig. 3 *Images taken during the pattern detection. a) An example illumination pattern where the alignment marker is not illuminated. b) The inverse pattern of part a) where the marker is illuminated. c) The illumination pattern from part b) after the spectral filter is applied. The marker shown in red is roughly 20 μm in diameter.*

Fig. 4a) shows the Temporal Fluorescent Modulated (TFM) data, the spectral response from each frame recorded for a representative marker. There is a pattern of three frames on and then three frames off, based on the position of the fluorescent marker and the 'fingerprint' pattern for that position, meaning that sequence will only be seen if the marker is in that position in the projected pattern. The different heights of the peaks reflect the relative overlap between the marker and projected LED pattern; the higher the peak, the more the two overlap.

The TFM data is used as the basis of the automated positioning system. The high difference between the on and off frames when the marker is fully in the FOV of the LED array in Fig. 4a) allows us to reduce the inherent errors when using this data for positioning purposes. A minimum search is applied onto the TFM data to find the position of the marker, which requires co-ordinates to be assigned in the FOV of the chequerboard array (LED1 in Fig. 1). Fig. 4b) shows the temporal illumination modulation data, the illumination of the LED in each frame at the co-ordinate where the marker was calculated to be; a strong resemblance can be seen between this and the TFM data.

Marker Trajectory: In order to test the automated positioning system, we again randomly dispersed markers, from which an area was manually selected in which only one marker was visible in the FOV of the 450 nm chequerboard array, then assigned a target co-ordinate to position to. The system was run until the marker was reported to be on the assigned coordinate, which was verified with the camera.

Typically, the mechanical stage controlled by the system's reference to the makers is seen to require two sets of XY movements before successfully arriving at its target location, though this varies depending on the distance that the stage travels. This is due to inherent inaccuracies coming from both the stage pico-motors themselves, and that the fill factor of the LED emitted area is not 100 %. The highest number of cycles observed during alignment is from one corner to the opposite corner of the FOV (i.e. 630 μm distance) which required three detection and movement cycles. As shown in Fig. 1, the absolute precision of the setup is dependent on the projected image size, rather than physical size of the μ-LEDs in the LED2 array.

Fig. 5 shows an example of the trajectory of the marker during alignment and the inaccuracies in its position, as determined by camera verification. Here we took a marker which was aligned to coordinate (13,11) in the 16×16 array and set its final location to (15,15). As shown, the positioning required only two sets of XY movements. This was repeated from corner to corner, requiring three sets of measurements
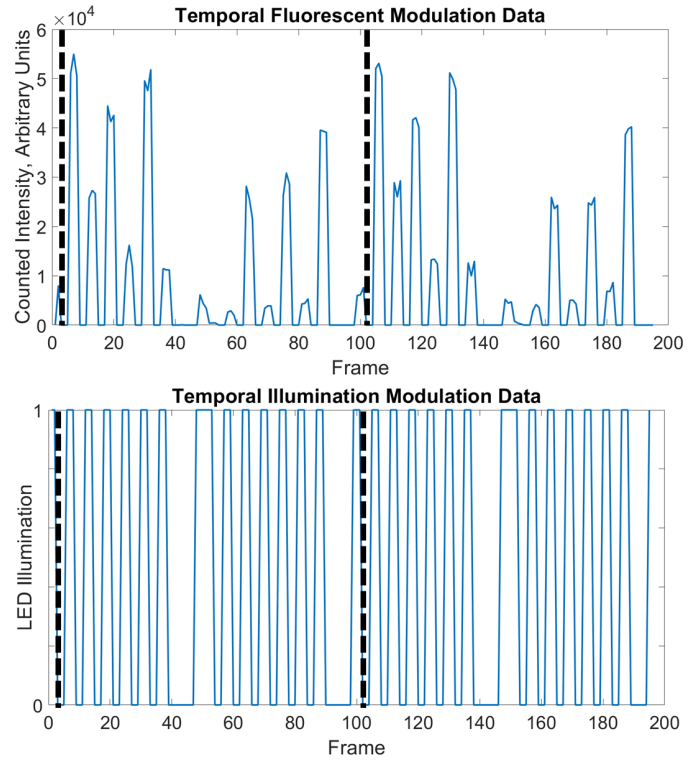

Fig. 4 *a) Graph showing the temporal modulated fluorescent data for the system from the moving bars imaging sequence. The dotted lines indicate the start frame of the imaging sequence. b) Graph showing the temporal illumination fluorescent data for the system from the moving bars imaging sequence. The dotted lines indicate the start frame of the imaging sequence.*

instead. Note that this particular measurement was done with a 405 nm wavelength 16×16 array of circular pixels with a 41 % fill factor, not the tessellated device with a 98 % fill factor, as shown in Fig. 1. These results show that the requirements on device uniformity and fill factor are not demanding, and any light which does not interfere with either the photo-resist or the fluorescent emission can be used. The higher fill factor of the chequerboard device results in lower inaccuracies during alignment compared to the circular device.

Aligned Micro-Photolithography: The second μ-LED array in our set-up, operating at 405 nm, is capable of mask-free exposure of resists and polymers patternable by h-line photolithography. To demonstrate the basic characteristics of this system under 10X demagnification as shown in Fig. 1, we used a commercially available UV sensitive resin (Anycubic). This was then applied to the slide and spun to a film thickness of 9 μm. After alignment to the curing μ-LED array, the sample is cured with a dosage of approximately 181 mJ/cm^2, at a stage travel speed of 25μm/s, up to 25mm in any one dimension. After photocuring, the sample was developed and cleaned.

The CMOS integrated μ-LED arrays allow spatial and temporal control of the emitted light through pulse width modulation, allowing control of the line width and feature size produced in the resist while keeping the writing speed constant. We achieved line thicknesses ranging from 14-35 μm, as measured by an optical profiler (Wyko NT1100), at a maximum height of 9 μm. By using smaller μ-LEDs, it is possible to achieve sub-micron resolution in such a system [11]. A reduced feature size can also be achieved by reducing the size of the projected μ-LEDs via stronger demagnification at the beam expander. However, by doing so, the FOV for the structured illumination will also be reduced, meaning that the tracking capability discussed earlier can only operate over a smaller area. Because of this, there is an inherent trade off between feature resolution and FOV. The write speed is limited by the stage speed to 1 mm/s and the stage range of 25.4 mm limits any patterns made.
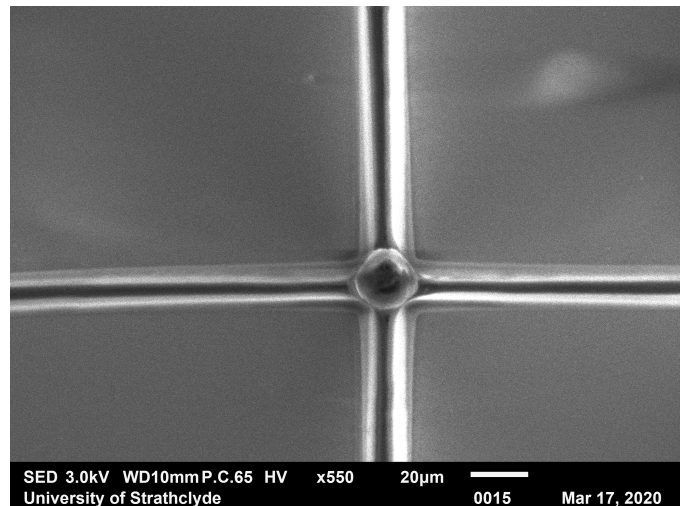
We then combined this 405 nm direct writing with our active alignment capability demonstrated above. As a representative example, in Fig. 6, we located and calibrated the system's positioning on a fluorescent marker using the patterned light sequences at 450 nm, and then wrote at 405 nm a cross pattern in resist which aligned with the marker at the crossing
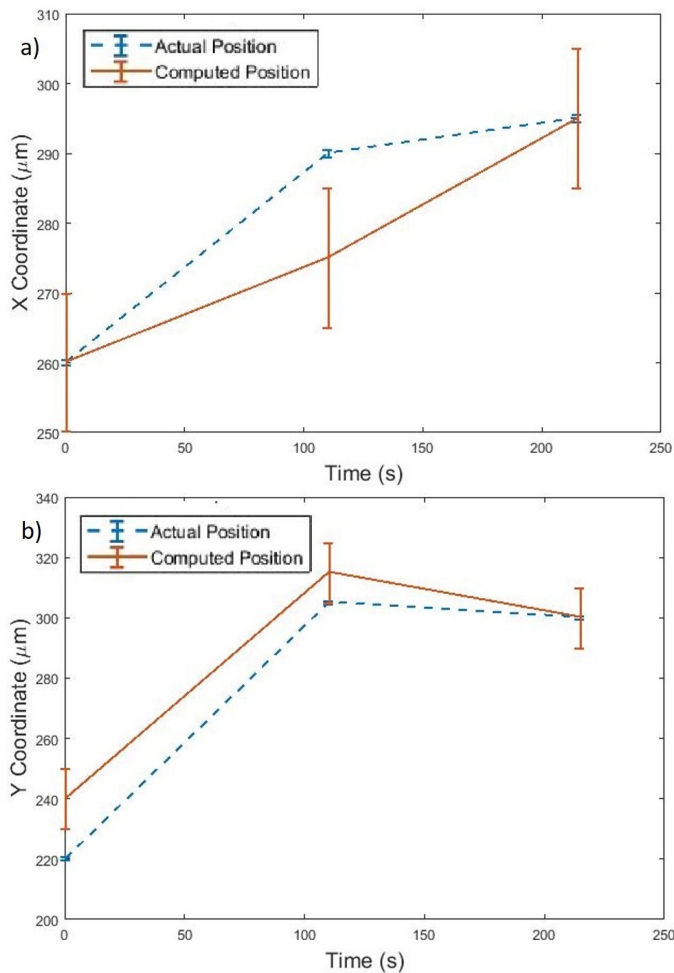
Fig. 5 *The movement of a fluorescent marker during the alignment process, for a) the x-coordinate, and b) the y-coordinate with respect to time. The computed position determined by the structured illumination process and the actual position as monitored by the camera through conventional imaging are shown. The error bars represent the coordinate grid resolution for the computed position and the pixel size and resolution of the CCD camera.*

Fig. 6 *An SEM plane-viewed image of a cross with the alignment marker contained at the intersection. The marker at the centre is 21 μm in diameter.*

point. This shows the basic capability of this active alignment and direct writing system to produce aligned multi-step processing, for example, by encapsulating luminescent microstructures within or between separately microstructured polymer encapsulation or other functionality layers. Fig. 6 uses environmental-mode operation of the SEM to suppress charging without application of any conductive coating and was taken with a curing dose of 181 mJ/cm^2 from an LED duty cycle of 0.062, with a photoresist thickness of 9 μm.

Conclusion: We have developed and demonstrated an automated alignment system using a CMOS integrated 16×16 μ-LED array for structured illumination, measuring the fluorescent response of a microscale marker to a temporally dependent fingerprint signal. This positioning capability was then used as the basis for an automated alignment system, tracking the movement of the fluorescent marker to a pre-determined co-ordinate, taking two or three alignment cycles to do so. The positioning was then independently verified by a camera. The positioning system is used as the basis of a micro photo-lithography tool, using another CMOS integrated μ-LED array at a different wavelength for photo-curing at the aligned coordinate. The two arrays having different wavelengths means that the alignment does not affect the curing. Although we have used fluorescent markers here, it is also possible to align to reflective markers. Spectral analysis is possible at the detector end of the alignment process, demonstrated here with the RGB channels of the camera, but extendable to finer wavelength resolution taking advantage of the principles of single-pixel imaging. This can be explored via use of a spectrometer as the detector, allowing for narrower spectral signatures to be aligned to instead of a broad RGB signal for enhanced target identification from the spectral signatures.

*M. Stonehouse, *A. Blanchard, B. Guilhabert, E. Gu, J. Herrnsdorf, I. M. Watson and M. D. Dawson (*Institute of Photonics, Department of Physics, University of Strathclyde, Glasgow, UK*)

E-mail: alexander.blanchard@strath.ac.uk

Y. Zhang (*Information Optoelectronics Research Institute, Harbin Institute of Technology at Weihai, Weihai, China*)

*These authors contributed equally to this work.

References

1 Levinson, H.J.: 'Principles of lithography'.
  (SPIE Bellingham, WA, 2019)
2 Dinh, D.H., Chien, H.L., Lee, Y.C.: 'Maskless lithography based on digital micromirror device (DMD) and double sided microlens and spatial filter array', *Optics & Laser Technology*, 2019, **113**, pp. 407–415
3 Rydberg, C.: 'Laser Mask Writers in Handbook of Photomask Manufacturing Technology'.
  Rizvi, S., editor. (CRC Press, Boca Raton, USA, 2005)
4 Herrnsdorf, J., McKendry, J.J.D., Zhang, S., Xie, E., Ferreira, R., Massoubre, D., et al.: 'Active-Matrix GaN Micro Light-Emitting Diode Display With Unprecedented Brightness', *IEEE Transactions on Electron Devices*, 2015, **62**, (6), pp. 1918–1925
5 Elfström, D., Guilhabert, B., McKendry, J., Poland, S., Gong, Z., Massoubre, D., et al.: 'Mask-less ultraviolet photolithography based on CMOS-driven micro-pixel light emitting diodes', *Opt Express*, 2009, **17**, (26), pp. 23522–23529
6 Stonehouse, M., Blanchard, A., Guilhabert, B., Watson, I.M., Gu, E., Herrnsdorf, J., et al.: 'Microscale automated alignment and spatial tracking through structured illumination', *IEEE Photonics Conference (IPC)*, October 2019,
7 Edgar, M.P., Gibson, G.M., Padgett, M.J.: 'Principles and prospects for single-pixel imaging', *Nature photonics*, 2019, **13**, (1), pp. 13–20
8 Xu, Z.H., Chen, W., Penuelas, J., Padgett, M., Sun, M.J.: '1000 fps computational ghost imaging using LED-based structured illumination', *Optics express*, 2018, **26**, (3), pp. 2427–2434
9 Herrnsdorf, J., Strain, M.J., Gu, E., Henderson, R.K., Dawson, M.D.: 'Positioning and space-division multiple access enabled by structured illumination with light-emitting diodes', *Journal of Lightwave Technology*, 2017, **35**, (12), pp. 2339–2345
10 Herrnsdorf, J., Dawson, M.D., Strain, M.J.: 'Positioning and data broadcasting using illumination pattern sequences displayed by LED arrays', *IEEE Transactions on Communications*, 2018, **66**, (11), pp. 5582–5592
11 Guilhabert, B., Massoubre, D., Richardson, E., McKendry, J.J., Valentine, G., Henderson, R.K., et al.: 'Sub-micron lithography using InGaN micro-LEDs: mask-free fabrication of LED arrays', *IEEE Photonics Technology Letters*, 2012, **24**, (24), pp. 2221–2224

Design, Fabrication, and Application of GaN-Based Micro-LED Arrays With Individual Addressing by N-Electrodes

Enyuan Xie
Mark Stonehouse
Ricardo Ferreira
Jonathan J. D. McKendry, *Member, IEEE*
Johannes Herrnsdorf, *Member, IEEE*
Xiangyu He
Sujan Rajbhandari, *Member, IEEE*
Hyunchae Chun
Aravind V. N. Jalajakumari
Oscar Almer
Grahame Faulkner
Ian M. Watson
Erdan Gu, *Member, IEEE*
Robert Henderson
Dominic O'Brien, *Member, IEEE*
Martin D. Dawson, *Fellow, IEEE*
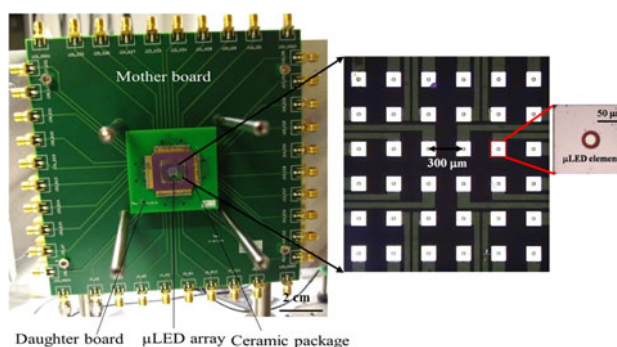
Design, Fabrication, and Application of GaN-Based Micro-LED Arrays With Individual Addressing by N-Electrodes

Enyuan Xie [ID],[1] Mark Stonehouse [ID],[1] Ricardo Ferreira [ID],[1]
Jonathan J. D. McKendry,[1] *Member, IEEE*,
Johannes Herrnsdorf [ID],[1] *Member, IEEE*, Xiangyu He [ID],[1]
Sujan Rajbhandari [ID],[2,4] *Member, IEEE*, Hyunchae Chun [ID],[2]
Aravind V. N. Jalajakumari [ID],[3] Oscar Almer,[3] Grahame Faulkner,[2]
Ian M. Watson [ID],[1] Erdan Gu,[1] *Member, IEEE*, Robert Henderson,[3]
Dominic O'Brien,[2] *Member, IEEE*,
and Martin D. Dawson [ID],[1] *Fellow, IEEE*

[1]Institute of Photonics, Department of Physics, University of Strathclyde, Glasgow G1 1RD, U.K.
[2]Department of Engineering Science, University of Oxford, Oxford OX1 3PJ, U.K.
[3]CMOS Sensors and Systems Group, University of Edinburgh, Edinburgh EH9 3JL, U.K.
[4]Centre for Mobility and Transport, School of Computing, Electronics and Mathematics, Coventry University, Coventry CV1 2JH, U.K.

Abstract: We demonstrate the development, performance, and application of a GaN-based micro-light emitting diode (μLED) array sharing a common p-electrode (anode), and with individually addressable n-electrodes (cathodes). Compared to conventional GaN-based LED arrays, this array design employs a reversed structure of common and individual electrodes, which makes it innovative and compatible with n-type metal-oxide-semiconductor (NMOS) transistor-based drivers for faster modulation. Excellent performance characteristics are illustrated by an example array emitting at 450 nm. At a current density of 17.7 kA/cm^2 in direct-current operation, the optical power and small signal electrical-to-optical modulation bandwidth of a single μLED element with 24 μm diameter are over 2.0 mW and 440 MHz, respectively. The optimized fabrication process also ensures a high yield of working μLED elements per array and excellent element-to-element uniformity of electrical/optical characteristics. Results on visible light communication are presented as an application of an array integrated with an NMOS driver. Data transmission at several hundred Mb/s without bit error is achieved for single- and multiple-μLED-element operations, under an ON–OFF-keying modulation scheme. Transmission of stepped sawtooth waveforms is also demonstrated to confirm that the μLED elements can transmit discrete multilevel signals.

Index Terms: GaN, micro-light emitting diode array, Individual addressing by n-electrodes, visible light communication.

1. Introduction

Gan-Based light emitting diodes (LEDs), which have achieved great importance in conventional chip formats as indicators and in solid-state lighting, can also be fabricated into arrays of micro-scale LED elements with lateral dimensions of less than 100 μm [1]. The operating current densities and optical power densities of these micro-LED (μLED) elements are significantly higher than for conventional broad-area LED devices [2] and the devices can be fabricated in high-desity 1D and 2D arrays. Thanks to these properties, μLED arrays are attractive for applications including micro-displays (μdisplays) [3], projection [4], optoelectronic tweezers [5] and maskless photolithography [6]. Furthermore, the high operating current density leads to a short differential carrier lifetime [7], thus making μLED arrays promising for high-speed visible light communications (VLC) both in free space and in polymer optical fiber [8]. VLC using LEDs offers the possibility of employing general illumination devices for data transmission, and many other advantages including license-free operation, high spatial diversity and innate security [9]. In our recent work, we demonstrated that single GaN-based μLED elements have typical electrical-to-optical (E-O) modulation bandwidths in the range of 100 to 400 MHz [7], and in some cases up to 800 MHz [10]. Error-free data transmission up to 1.7 Gbps [10] and 7.9 Gbps [11] has been achieved using on-off keying (OOK) and orthogonal frequency division multiplexing (OFDM), respectively, applied to such single μLED elements. By operating a μLED array in a ganged (parallel-addressed) fashion, it is possible to obtain a higher signal-to-noise ratio, and thus longer data-transmission distance, while retaining a fast data rate [12].

In recent years, with the maturation of fabrication techniques, different addressing schemes for μLED arrays have been demonstrated [13]–[15]. An active driving scheme can be accomplished by integrating μLED arrays with complementary metal-oxide-semiconductor (CMOS) active matrix drivers, using flip-chip bonding [3], [7], [15]. Compared with the alternative matrix addressing scheme, the flexible control of individual elements is of great benefit for μ display and VLC applications. However, in the conventional embodiment, there are also some drawbacks. In a conventional μLED array, elements share a common n-electrode (cathode) with individually addressable p-electrodes (anodes). This configuration is shown in Fig. 1(a), and it is generally used because standard GaN LED epitaxial structures invariably have the p-side of the junction on top, which is necessitated by the relatively low conductivity of p-doped GaN [16], in addition to several growth issues.

In the configuration shown in Fig. 1(a), the n-type GaN layer functions as a shared conductive path for all μLED elements in the array. Therefore, different distances between the common n-electrode and the respective μLED elements lead to different series-resistance contributions from the n-type GaN. These differing series resistances result in non-uniform operating currents at the same applied voltage for each μLED element and, thus, poor optical element-to-element uniformity [14] and high crosstalk [17], which are undesirable in practical applications. Concerning the driver choice, this configuration also restricts the CMOS circuitry to designs based on p-type MOS (PMOS) transistors. It is well known that the mobility of majority carriers (holes) in PMOS transistors ($\approx$450 cm^2/(V·s) in Si doped at 10^{15} cm^{-3}) is significantly lower than that of majority carriers (electrons) in NMOS transistors ($\approx$1500 cm^2/(V· s) in Si doped at 10^{15} cm^{-3}) [16]. Thus, the operating speed of PMOS transistors is slower than comparable NMOS transistors. Additionally, in order to achieve the same impedance, a larger size is required for PMOS transistors. This, in turn, leads to a larger area requirement on the chip and also a larger capacitance, thus further reducing the operating speed of PMOS transistors [18]. These factors are highly disadvantageous for μLED array applications, since the achievable density of driver cells on a chip, and the modulation speed supplied from the CMOS, are both limited. Following these considerations, it is advantageous if the series resistance difference between μLED elements can be minimized and, simultaneously, NMOS drivers used.

In this work, we demonstrate an innovative GaN-based μLED array configuration combining a common p-electrode with individually addressable n-electrodes. Compared with a conventional μLED array, this design employs a reversed common and individual electrode structure, which minimises the series-resistance differences from conductive paths and provides compatibility with NMOS transistor-based CMOS drivers. We have furthermore developed the fabrication process and describe how the various challenges in the fabrication of GaN-based LED arrays with individual
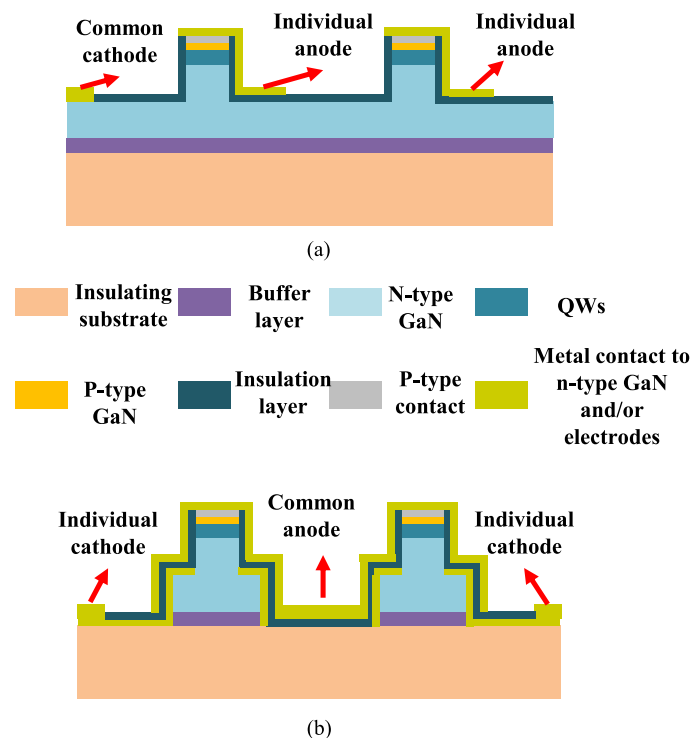
Fig. 1. Simplified cross-sectional schematic configurations of a conventional μLED array (a) and the innovative variant developed in this work (b). Dimensions are not to scale.

n-electrodes can be addressed. We have improved the performance, the proportion of working μLED elements per array (referred to as μLED element yield from here on) and the uniformity of electrical/optical characteristics in comparison with our earlier work [7], [15]. Example arrays fabricated from a commercial blue LED wafer on sapphire show performance characteristics confirming the potential of the approach. At 450 nm, over 2.0 mW optical power and 440 MHz E-O modulation bandwidth are achieved for a single μLED element of 24 μm diameter at 17.7 kA/cm^2 operating current density.

We also demonstrate the integration of this array with a custom CMOS driver based on NMOS transistors. This driver is capable of operating the LEDs with various modulation schemes. While many current VLC demonstrations rely on the usage of arbitrary waveform generators, the integrated system here is a stepping stone towards more practical implementations. To demonstrate its basic functionality, the responses from single- and/or multiple-μLED elements under an on-off-keying (OOK) data transmission scheme are presented. Open eye-diagrams are recorded at several hundred Mbps. Transmission of stepped sawtooth waveforms is also studied to illustrate the capability of this integrated system to transmit optical signals with discretely varying intensity.

2. Experimental Details

The μLED arrays were fabricated from blue III-nitride LED wafers grown on c-plane (0001) sapphire with periodically patterned surfaces. Light was extracted through the sapphire, the backside of which was polished before device fabrication. The LED epitaxial structure consists of a 3.4 μm-thick undoped GaN buffer layer, a 2.6 μm-thick n-type GaN layer, eleven periods of InGaN (2.8 nm)/GaN (13.5 nm) quantum wells (QWs) emitting at 450 nm, a 30 nm-thick p-type AlGaN electron blocking layer and a 160 nm-thick p-type GaN topmost layer. The μLED arrays discussed in detail here contain a 6 $\times$ 6 layout of μLED elements, each with a diameter of 24 μm (452.2 μm^2 emitting area),

on a 300 μm center-to-center pitch. Variants on this design were also fabricated, and are discussed further in connection with optimization of processing in Section 3-B.

As mentioned above, each μLED element in the array developed in this work is individually addressed by its own n-electrode with a shared p-electrode. Fig. 1 illustrates the simplified schematic configurations of the conventional μLED array, (a), and the one developed in this work, (b). The μLED elements in the conventional array are defined by element etching finished at the n-type GaN layer. By this means, all the μLED elements in the array are connected via n-type GaN and, thus, share a common n-electrode, while having individually addressable p-electrodes. In order to realize a μLED array with individually addressed n-electrodes, each μLED element must be fully isolated from both p- and n-type GaN layers as shown Fig. 1(b). To achieve this configuration, two steps of Cl_2-based plasma etching of GaN are involved. Fig. 2 shows the main steps. Firstly, a 6 $\times$ 6 array of GaN mesas, in a square shape with sides of 130 μm, is etched down to the sapphire substrate by inductively coupled plasma (ICP) etching [see Fig. 2(a)]. Then, a disk-shaped μLED element with 24 μm diameter is created at the centre of each mesa through a second ICP etch which stops at the n-type GaN layer [see Fig. 2(b)]. This two-step etching not only enables the isolation of μLED elements from both p- and n-type GaN layers, but also guarantees the same contact area of metal contacts to n-type GaN for each μLED element. Although the square mesas have a separation of 170 μm in the design discussed in detail, these principles have also been applied to arrays in which the mesas are separated by a gap of only 6 μm.

After the etching steps described, a 100 nm Pd metal layer is evaporated on the p-type GaN surface and thermally annealed in a N_2 ambient at 300 °C to form a quasi-ohmic contact to p-type GaN. The metallization on the isolated n-type GaN mesa is realized by sputtering a Ti/Au (50/200 nm) metal bilayer and a lift-off process. This bilayer is also patterned to make metal tracks from the n-type GaN mesas to individually address every μLED element [see Fig. 2(c)]. Specific lift-off resists used include Dow Megaposit SPR220 4.5 (positive-working) and Micro Resist Technology ma-N 1420 (negative-working). Solvent-based treatments used to remove photoresist residues in non-optimised processes involved 1-methyl-2-pyrrolidone, with heating up to 120 °C or ultrasonication, in addition to methanol and acetone. Then, in our optimised process, the array is cleaned by an O_2-based plasma at 200 °C in a plasma asher (Matrix 105 system). We have found plasma ashing is an especially critical step to optimise the μLED element yield and uniformity of electrical/optical characteristics. These improvements will be discussed in more detail in Section 3-B.

Following the plasma clean, a 300 nm-thick SiO_2 layer is deposited by plasma enhanced chemical vapor deposition. After selectively removing SiO_2 on top of each μLED element, another Ti/Au metal bilayer is deposited to interconnect μLED elements forming a shared p-electrode, as illustrated by the shaded overlays (with dashed red outlines) in Fig. 2(d). Fig. 2(e) shows a schematic layout of the whole array to emphasise the electrode configuration. Although different distances between electrodes and target μLED elements still exist, it is important to note that the conductive paths are formed by Ti/Au metal bilayers, rather than the n-type GaN as in the conventional configuration. Thus, the resulting series-resistance differences are minimised, owing to the significantly lower sheet resistivity of the metal layer.

The custom CMOS driver used in this work is based on NMOS transistors, and contains four independent current-steering digital-to-analog converter (DAC) driver channels with 8-bit resolution. Each driver channel is designed to sink a full-scale current up to 255 mA, and operates at an electrical-to-electrical modulation bandwidth of 250 MHz. More detailed information can be found in [19]. In order to integrate the μLED array with the CMOS driver, the μLED array is firstly wire-bonded to a commercial ceramic package, which is soldered to a daughter card. The daughter card and motherboard are connected through four high-speed connectors. The motherboard has 40 SubMiniature Version A (SMA) connectors around the edge. Four of these SMA connectors are used for supplying power, and the other connectors are used for connecting the μLED elements to the CMOS driver. A photograph of the assembled system is shown in Fig. 3.

Before integrating the μLED array with the CMOS driver, its electrical, optical and modulation performance characteristics were measured. The quoted yields of working μLED elements are based on measurements of several tens of individual arrays. By placing a Si photodetector in close
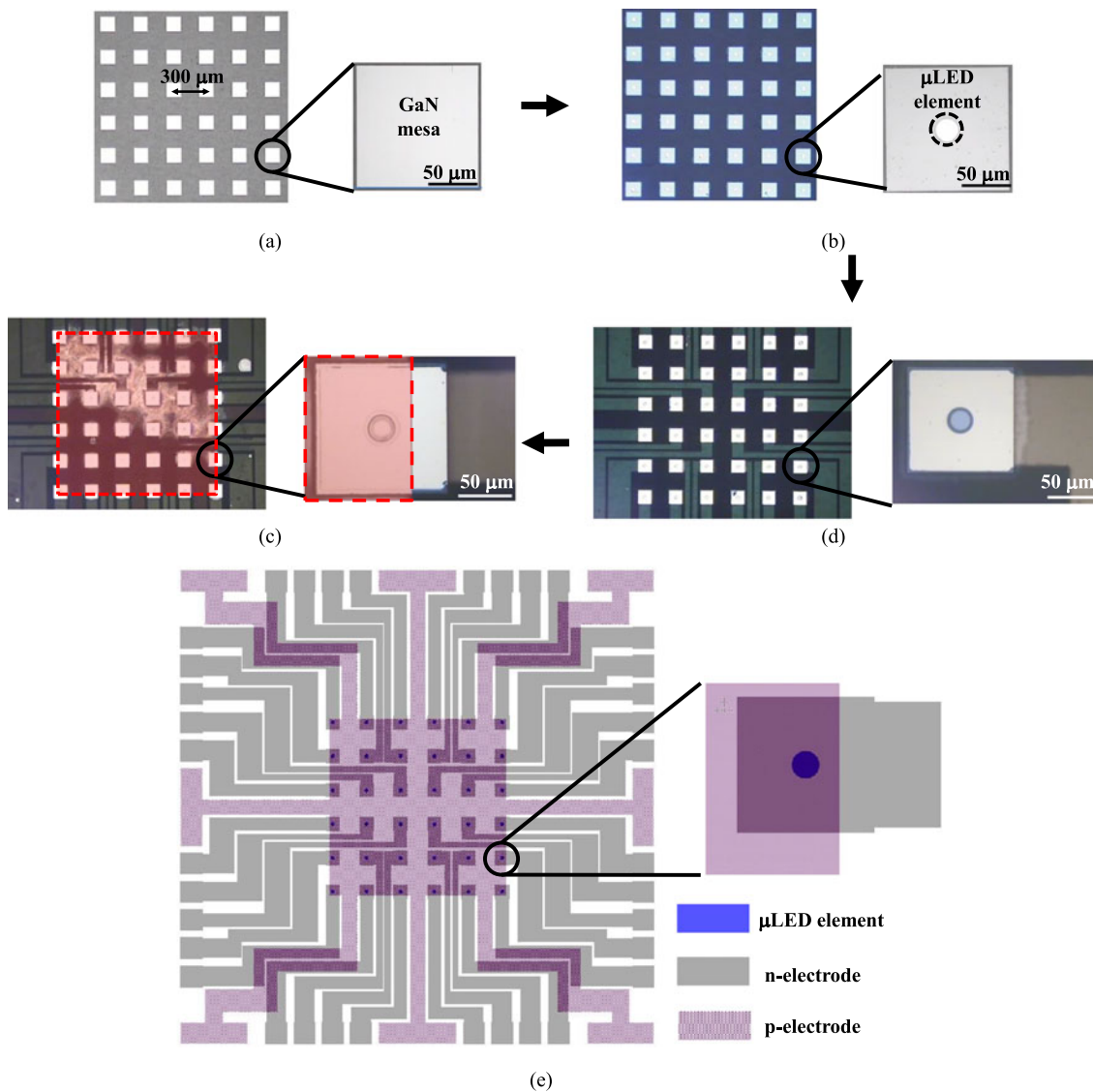
Fig. 2. Plan view optical images of the main steps in the fabrication process of μLED array with individually addressable n-electrodes: (a) GaN mesa etching down to the sapphire substrate; (b) μLED element etching finished at the n-type GaN layer; (c) metal deposition for individually addressable n-electrodes; (d) metal deposition for a shared p-electrode. High-magnification images for a typical μLED element are also shown. Part (e) shows a schematic layout of the whole μLED array.

proximity to the polished sapphire substrate of the μLED array, the current versus voltage (I-V) and optical power versus current (L-I) characteristics were measured at the same time, through scanning each data point under direct-current (DC) conditions. The E-O modulation bandwidth of μLED elements was measured following the same method described in [7] and [15]. A small-signal modulation, of fixed amplitude, from an HP8753ES network analyser was combined with a DC bias using a bias-tee, and applied to a representative μLED element using a high-speed probe. The modulated light output from the μLED element was collected by a 1.4 GHz bandwidth photoreceiver, and a network analyzer used to measure the frequency response.

After the initial characterization outlined, the μLED array was integrated with the CMOS driver to demonstrate its compatibility and application in VLC with integrated control. Arbitrary waveforms were sent to the μLED elements through the CMOS drivers. These waveforms were generated
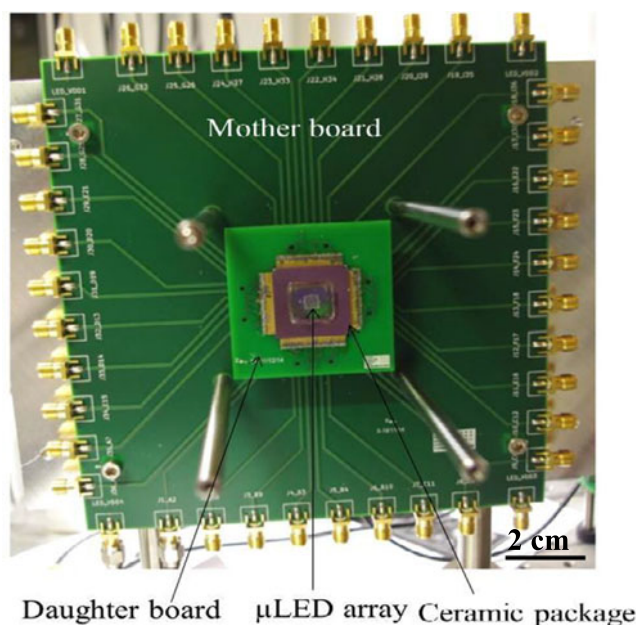
Fig. 3. Photograph of the system integrating the individual-n-addressable μLED array with the NMOS-based CMOS driver.

through a MatlabTM interface, and downloaded onto the field-programmable gate array. The signal levels correspond to integers ranging from 0–255 on an 8-bit DAC, and waveforms were created as a 1 $\times$ X array. The corresponding output current of the CMOS drivers was proportional to the received integer value for each sample period. The symbol-rate was determined by modifying the clock speed of the CMOS driver, which was also controllable through the Matlab interface. The LED power supply was set to 9 V and limited to 70 mA per active μLED element. The output responses were collected by a Hamamatsu C5658 avalanche photodiode (APD) with 1 GHz bandwidth. The distance between the μLED array and APD was around 50 cm. All measurements were performed at room temperature.

3. Results and Discussion

3.1 Performance of a Single μLED Element

Fig. 4(a) illustrates the typical I-V and L-I characteristics of a single μLED element in an array. This μLED element can be operated at a current up to 80 mA, and is able to produce an optical power over 2 mW before thermal rollover, which corresponds to current and optical power densities of 17.7 kA/cm^2 and 442.3 W/cm^2, respectively This high operating current density leads to a shorter differential carrier lifetime and, thus, increases the modulation bandwidth of the μLED element [7]. As shown in Fig. 4(b), this μLED element has an E-O modulation bandwidth in excess of 440 MHz, which is over 12 times higher than the corresponding value for typical commercial LEDs [20]. Compared with an individual μLED element from the conventional individually p-addressable array reported in our early work [7], [15], all the performance characteristics show a significant improvement, which is in part attributed to the Pd metal contact to p-type GaN employed here. We have found that Pd metal contacts to p-type GaN have lower specific contact resistivity and higher reflectivity than the metal contact scheme used in our previous work: annealed Ni/Au, capped with Ti/Au as a reflector. These properties reduce the series resistance of a μLED element, and enhance the light extraction efficiency (LEE) resulting in better electrical, optical and modulation performance. Another significant point of comparison with a μLED element in a conventional array
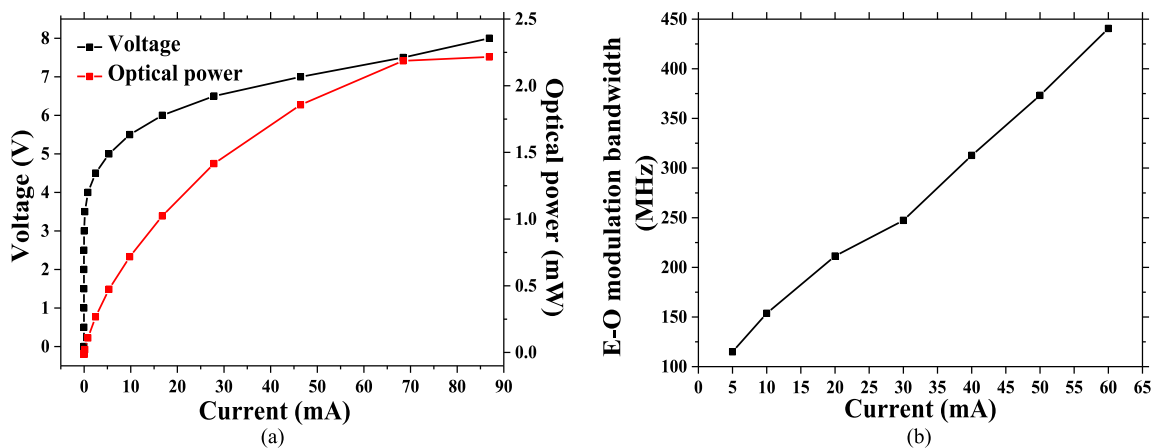
Fig. 4. (a) I-V and L-I characteristics of a single μLED element in the array; (b) E-O modulation bandwidth characteristic of the same μLED element. Lines connecting data points are to guide the eye only.

is that the area of metal contact to n-type GaN for each μLED element is limited by the size of the GaN mesa etched down to the sapphire substrate, as discussed in Section 2. This limited contact area (less than 1.7×10^{-4} cm^2 per element) leads to the higher series-resistance contributed from the metal contact to n-type GaN, which should degrade the I-V characteristic for the μLED element in this innovative array such as higher turn-on voltage. Nevertheless, we do not observe the remarkable degradation on the I-V characteristic and the low contact resistivity of the Ti/Au metal contact to n-type GaN ($\sim 3.7 \times 10^{-5}$ cm^2) [21] rationalizes this observation. This observation further indicates that the electrical performance of a GaN-based μLED element is dominated by the series-resistance from the metal-contact to p-type GaN which also motivates our work on Pd metal contact to p-type GaN as discussed in early part.

3.2 μLED Element Yield and Uniformity of Electrical/Optical Characteristics

In addition to the performance characteristics of single μLED elements, the μLED element yield and the uniformity of electrical/optical characteristics across a full array are important factors for applications. As explained above, a deep etch down to the sapphire substrate is necessary to define separate GaN mesas within which each μLED element is fabricated. This step leads to a relatively deep gap, or trench, between adjacent GaN mesas (around 6 μm in depth for the epitaxial structure employed), which has no counterpart in conventional μLED array process flows. We have found this deep gap has a great influence on the μLED element yield, and reference to Fig. 1(b) will show how dielectric and metal layers must be deposited over the exposed substrate in this region. Initial versionsof the 6×6 μLED arrays were fabricated using conventional stripping solvents to remove lift-off resists, and the specific materials tried were detailed in Section 2. With 170 μm gaps between mesas, the μLED element yield in the array was around 90%. However, when the gap width decreased to 6 μm in a similar array design, the μLED element yield dropped to around 67%. The cause of low yields was the incomplete removal of photoresist residues, as illustrated by a typical scanning electron microscope (SEM) image shown in Fig. 5. These photoresist residues lead to degradation of the SiO$_2$ layer deposited in the following step and, consequently, short-circuiting of μLED elements and low element yield. The extent of contamination was also consistently greater in the small-gap case. Although our survey of different types of lift-off resist and cleaning solvents could not be exhaustive, we consider this issue and the solution now discussed to be of general applicability. The optimized process introduced an O$_2$-based plasma ashing step to replace the solvent-based step for photoresist stripping before the SiO$_2$ deposition. Such low-damage oxidizing plasma processing is known to be effective for full removal
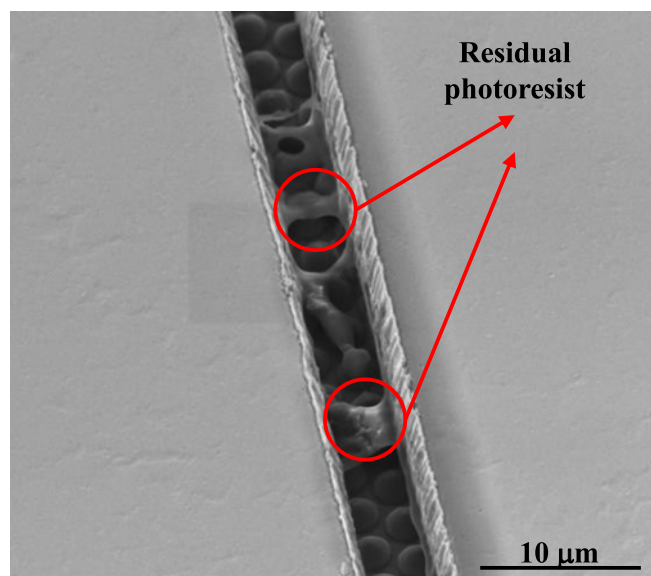
Fig. 5. Oblique-view SEM image of photoresist residues in a deep narrow gap (6 μm in both width and depth) between two adjacent GaN mesas. Examples of photoresist residues are highlighted by red circles. The lenticular features visible in the gap are from the periodic surface texturing (patterned sapphire substrate, PSS) applied to the sapphire before the growth of the LED structure. Note also that the GaN etch steps leave near-vertical sidewalls.

of photoresist residues in many other types of semiconductor device processing. We are not aware of a previous application to analogous GaN device process flows, but the chemical stability of GaN and its relative resistance to oxidation [22] are possibly significant for the viability of our optimised process flow [23], [24]. With the introduction of this ashing step, the μLED element yield in the μLED array with 170-μ m mesa separation increased to 100% of arrays tested Furthermore, the yield improvement is more significant for μLED arrays with a narrower gap between mesas. For example, the μLED element yield in arrays with a gap width of 6 μm increased from 67% to over 95%.

As a separate issue to the improvement in μLED element yield, we find the ashing step can also improve the uniformity of electrical and optical characteristics. Because the custom CMOS drivers are designed for operation with current setpoints, we compared the applied voltage and optical output power of selected μLED elements when driven at the same operating current within the same array. Fig. 6(a) illustrates the applied voltage and optical power at a fixed current of 60 mA (corresponding to a current density of 13.3 kA/cm^2) measured for 5 randomly selected μLED elements in an array fabricated without O$_2$ plasma ashing. The applied voltage and output power variations are within 18.1% and 6.4%, respectively [Variation is defined as (V$_{max}$ V$_{min}$)/V$_{min}$ $\times$ 100% for voltage and equivalently for power]. Since the optical power of a μLED element at a fixed current is proportionate to LEE, which is strongly influenced by the reflectivity of the Pd-based metal contact to p-type GaN, the degree of uniformity confirms consistency in the optical properties of these contacts. The larger variations in applied voltage correlate with the different lengths of Ti/Au interconnection track to different elements. Fig. 6(b) shows comparable results for elements in an array processed with the plasma ashing step. The applied voltage and optical power variations at 60 mA are reduced to 6.8% and 3.5% respectively. To ensure a fair comparison, the positions of the five elements measured for this figure are exactly same as those measured for Fig. 6(a). The same pattern of variation in applied voltage, correlating with the length of interconnect track, can thus be seen. The applied voltage variation could also be further reduced by increasing the thickness of Ti/Au metal bilayer.
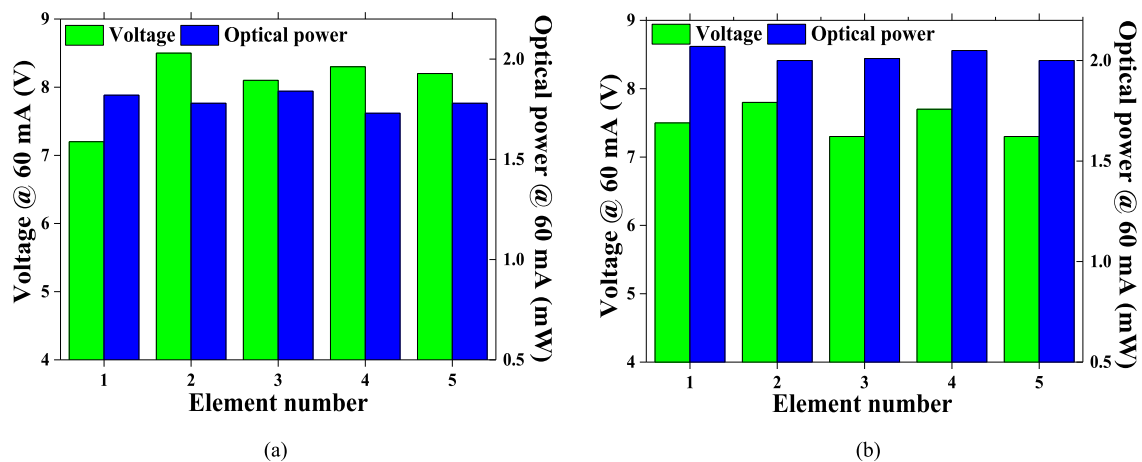
(a)   (b)

Fig. 6. Electrical and optical uniformities of 5 selected μLED elements of μLED arrays (a) without the ashing step or (b) with the ashing step. The positions of selected elements are exactly the same in both arrays.
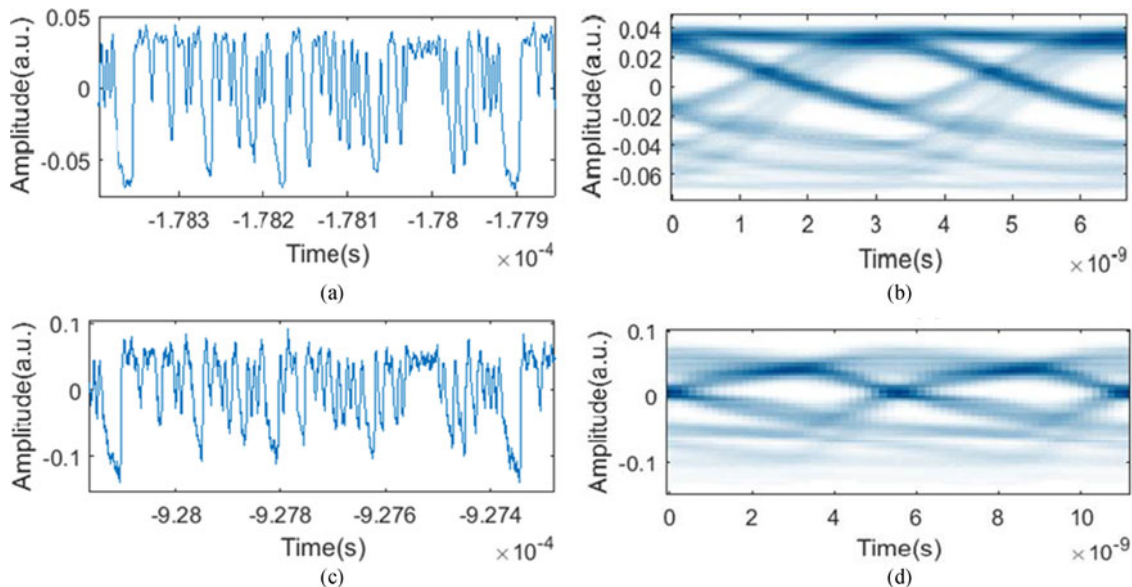

Fig. 7. Received waveforms and resultant eye-diagram for a single μLED element operated at 300 MHz [(a) and (b)] and four μLED elements operated at 180 MHz [(c) and (d)].

3.3 VLC Application of the μLED Array Integrated With NMOS Transistor-Based CMOS Driver

The μLED array was integrated with the custom NMOS transistor-based CMOS driver following the scheme described in Section 2. For the purpose of illustrating the VLC application, a pseudo-random OOK data stream was generated and sent to the μLED elements through the CMOS driver. This was done for 1 and 4 μLED elements each operating synchronously with the same waveform but driven by independent DACs. Pseudo random data sequences were generated and at transmitted between 10 and 475 Mbps. The received waveforms and resultant eye-diagrams are shown in Fig. 7. As shown in Fig. 7(a) and (b), a single-μLED-element could be operated at 300 Mbps without observable bit error. When four μLED elements were operated together, a similar eye diagram was observed at a lower bitrate of 180 Mbps, as shown in Fig. 7(c) and (d). This drop is
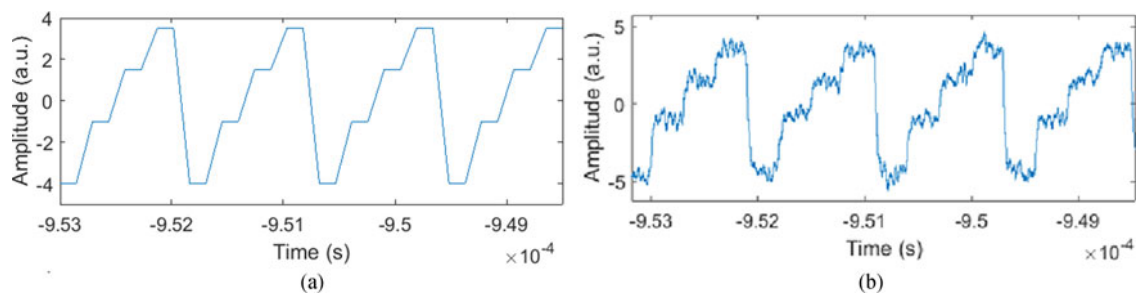
Fig. 8. Progammed stepped sawtooth input waveform with four distinct steps (a) and corresponded optical output waveform from a single μLED element (b). The μLED element was operated at 10 MHz.

likely due to heating effects as the four elements operated in close proximity to each other. It should be noted that the present array has no heat sink, so this effect has the potential to be alleviated. These results demonstrate single- and multi-element operation of the array at high bitrates. The apparent time jitter within the eye-diagram is partially due to the reset time of the DACs after each repetition of the OOK waveform.

As an alternative to simple OOK modulation, the custom CMOS driver is also capable of altering the modulation depth and DC offsets of the generated waveform, allowing greater control over the data encoding. This flexibility in operation allows the CMOS driver to directly modulate each μLED independently with different encoding schemes. The concept was tested with stepped sawtooth, or staircase-like, waveforms, representative of pulse amplitude modulation scheme. The optical output waveforms from a single μLED element in response to such input signal are shown in Fig. 8. The μLED element was operated at 10 MHz at an offset of 240 mA with a modulation depth of 16 mA. Using an input with 4-level input waveform as shown in Fig. 8(a), the corresponding μLED output also showed four distinct intensity levels clearly [see Fig. 8(b)]. The data rates presented here are lower than in our other work, which used multiple parallel channels to increase the aggregate data rate [19]. However, we wish to highlight that, since the modulation bandwidth of μLED elements was shown to be greater than 400 MHz, it does not limit the data rates achievable using this CMOS-driven system. Further optimization work is ongoing on both driver and μLED parts to improve the VLC performance of this integrated system.

4. Conclusion

In summary, we present the design, process flow development, performance characterization and application of an innovative GaN-based μLED array . In this design, μLED elements share a common p-electrode with individually addressable n-electrodes. This is a reversed structure compared with the conventional GaN-based arrays, which makes the array compatible with an NMOS transistor-based CMOS driver for faster modulation. We have optimized the fabrication process to improve the yield and uniformity of individual μLED elements. By integrating an array emitting at 450 nm with a custom NMOS transistor-based CMOS driver, application to VLC, and in particular to multi-level data encoding schemes, is also demonstrated.

Acknowledgment

References

[1] S. Jin, J. Li, J. Li, J. Lin, and H. Jiang, "GaN microdisk light emitting diodes," *Appl. Phys. Lett.*, vol. 76, no. 5, pp. 631–633, 2000.

[2] Z. Gong *et al.*, "Size-dependent light output, spectral shift, and self-heating of 400 nm InGaN light-emitting diodes," *J. Appl. Phys.*, vol. 107, no. 1, 2010, Art. no. 013103.

[3] J. Day, J. Li, D. Lie, C. Bradford, J. Lin, and H. Jiang, "III-nitride full-scale high-resolution microdisplays," *Appl. Phys. Lett.*, vol. 99, no. 3, 2011, Art. no. 031116.

[4] Z. J. Liu, W. C. Chong, K. M. Wong, K. H. Tam, and K. M. Lau, "A novel BLU-free full-color LED projector using LED on silicon micro-displays," *IEEE Photon. Technol. Lett.*, vol. 25, no. 23, pp. 2267–2270, Dec. 2013.

[5] A. H. Jeorrett *et al.*, "Optoelectronic tweezers system for single cell manipulation and fluorescence imaging of live immune cells," *Opt. Exp.*, vol. 22, no. 2, pp. 1372–1380, 2014.

[6] B. Guilhabert *et al.*, "Sub-micron lithography using InGaN micro-LEDs: Mask-free fabrication of LED arrays," *IEEE Photon. Technol. Lett.*, vol. 24, no. 24, pp. 2221–2224, Dec. 2012.

[7] J. J. McKendry *et al.*, "Visible-light communications using a CMOS-controlled micro-light-emitting-diode array," *J. Lightw. Technol.*, vol. 30, no. 1, pp. 61–67, Jan. 2012.

[8] D. Tsonev *et al.*, "A 3-Gb/s single-LED OFDM-based wireless VLC link using a gallium nitride μLED," *IEEE Photon. Technol. Lett.*, vol. 26, no. 7, pp. 637–640, Apr. 2014.

[9] H. Burchardt, N. Serafimovski, D. Tsonev, S. Videv, and H. Haas, "VLC: Beyond point-to-point communication," *IEEE Commun. Mag.*, vol. 52, no. 7, pp. 98–105, Jul. 2014.

[10] R. X. Ferreira *et al.*, "High bandwidth GaN-based micro-LEDs for multi-Gb/s visible light communications," *IEEE Photon. Technol. Lett.*, vol. 28, no. 19, pp. 2023–2026, Oct. 2016.

[11] M. S. Islim *et al.*, "Towards 10 Gb/s orthogonal frequency division multiplexing-based visible light communication using a GaN violet micro-LED," *Photon. Res.*, vol. 5, no. 2, pp. A35–A43, 2017.

[12] A. Jovicic, J. Li, and T. Richardson, "Visible light communication: Opportunities, challenges and the path to market," *IEEE Commun. Mag.*, vol. 51, no. 12, pp. 26–32, Dec. 2013.

[13] H. Jiang, S. Jin, J. Li, J. Shakya, and J. Lin, "III-nitride blue microdisplays," *Appl. Phys. Lett.*, vol. 78, no. 9, pp. 1303–1305, 2001.

[14] Z. Gong *et al.*, "Matrix-addressable micropixellated InGaN light-emitting diodes with uniform emission and increased light output," *IEEE Trans. Electron. Devices*, vol. 54, no. 10, pp. 2650–2658, Oct. 2007.

[15] J. J. McKendry *et al.*, "Individually addressable AlInGaN micro-LED arrays with CMOS control and subnanosecond output pulses," *IEEE Photon. Technol. Lett.*, vol. 21, no. 12, pp. 811–813, Jun. 2009.

[16] E. F. Schubert, T. Gessmann, and J. K. Kim, *Light Emitting Diodes*. Hoboken, NJ, USA: Wiley, 2005.

[17] J. Herrnsdorf *et al.*, "Active-matrix GaN micro light-emitting diode display with unprecedented brightness," *IEEE Trans. Electron. Devices*, vol. 62, no. 6, pp. 1918–1925, Jun. 2015.

[18] S. M. Sze and K. K. Ng, *Physics of Semiconductor Devices*. Hoboken, NJ, USA: Wiley, 2006.

[19] S. Rajbhandari *et al.*, "High-speed integrated visible light communication system: Device constraints and design considerations," *IEEE J. Sel. Areas Commun.*, vol. 33, no. 9, pp. 1750–1757, Sep. 2015.

[20] J. Vucic, C. Kottke, S. Nerreter, K.-D. Langer, and J. W. Walewski, "513 mbit/s visible light communications link based on DMT-modulation of a white LED," *J. Lightw. Technol.*, vol. 28, no. 24, pp. 3512–3518, Dec. 2010.

[21] Y.-I. Nam and B.-T. Lee, "Investigation of Ti/Au and Ti_2 N/Ti/Au ohmic contacts to n-GaN films," *Semicond. Sci. Technol.*, vol. 26, no. 8, 2011, Art. no. 085014.

[22] S. King *et al.*, "Cleaning of AlN and GaN surfaces," *J. Appl. Phys.*, vol. 84, no. 9, pp. 5248–5260, 1998.

[23] S. Fujimura, K. Shinagawa, M. Nakamura, and H. Yano, "Additive nitrogen effects on oxygen plasma downstream ashing," *Jpn. J. Appl. Phys.*, vol. 29, no. 10R, 1990, Art. no. 2165.

[24] A. Belkind and S. Gershman, "Plasma cleaning of surfaces," *Vacuum Coating Technol.*, pp. 46–57, Nov. 2008.